



**Annual Activity Report**  
**on**  
**Japan-ASEAN Science, Technology and**  
**Innovation Platform (JASTIP),**  
**Work Package 2 (WP2) –**  
**Energy and Environment**

2019 Progress

# TABLE OF CONTENTS

|  |           |
|--|-----------|
| <b><u>1. Innovations for Conversion of Biomass to High Value Chemicals by Photocatalytic Process</u></b> ..... | <b>3</b>  |
| <u>1.1 Introduction and Rational</u> .....   | 4         |
| <u>1.2 Project Scopes</u> .....  | 6         |
| <u>1.3 Project Progress</u> .....  | 7         |
| <u>1.4 Conclusions</u> .....   | 36        |
| <u>1.5 Project Outputs</u> .....   | 36        |
| <u>1.6 References</u> .....  | 40        |
| <b><u>2. Development of Carbons from Biomass for Energy Storage Applications</u></b> .....                     | <b>44</b> |
| <u>2.1 Introduction</u> .....  | 45        |
| <u>2.2 Research Progress</u> .....   | 46        |
| <u>2.3 Project Outputs</u> .....   | 61        |
| <b><u>3. Innovations in Biomass Application for Catalytic Material Synthesis and Energy Devices</u></b> .....  | <b>62</b> |
| <u>3.1 Purpose of Collaborative Research</u> .....   | 63        |
| <u>3.2 Research Progress</u> .....   | 664       |
| <u>3.3 Project Outputs</u> .....   | 87        |

**Innovations for Conversion of Biomass  
to High Value Chemicals by  
Photocatalytic Process**

# 1. Innovations for Conversion of Biomass to High Value Chemicals by Photocatalytic Process

Surawut Chuangchote<sup>1</sup>, Navadol Laosiripojana<sup>2</sup>, Verawat Champreda<sup>3</sup>, Takashi Sagawa<sup>4</sup>

<sup>1</sup> Department of Tool and Materials Engineering, Faculty of Engineering, King Mongkut's University of Technology Thonburi (KMUTT), 126 Prachauthit Rd., Bangmod, Thungkru, Bangkok 10140, Thailand.

<sup>2</sup> The Joint Graduate School of Energy and Environment, Centre of Excellence on Energy Technology and Environment, King Mongkut's University of Technology Thonburi (KMUTT), 126 Prachauthit Rd., Bangmod, Thungkru, Bangkok 10140, Thailand.

<sup>3</sup> National Center for Genetic Engineering and Biotechnology, 113 Phahonyothin Rd., Klong Luang, Pathumthani 12120, Thailand.

<sup>4</sup> Graduate School of Energy Science, Kyoto University, Kyoto 606-8501, Japan.

## Abstract

Application of photocatalytic processes for conversion of sugars which can be derived from lignocelluloses to energy and chemicals is considered a new promising environmentally friendly alternative which will play an important role in biorefinery and bioindustry related to valorization of sugars and agricultural wastes. This project aims to advance our technology on photocatalyst design under the JASTIP Renewable Energy program between NSTDA and Kyoto University (2015-2019). The project themes will cover (1) continual research on fabrication and modification of photocatalysts for conversion of sugars to high-value chemicals (*e.g.* functional sugar derivatives) by improving the catalyst's specificity by fabrication techniques or surface modification and (2) design and assembly of a prototype photocatalytic reactor. This concept on "photo-conversion on renewable biomaterials" will lead to the development of "photo-bio flow reactor" and will provide strong platform for conversion of sugars to value-added chemicals in integrative biorefinery.

**Keyword** Biomass, Photocatalysis, Sugar conversion, Lignin utilization, High-value chemicals, Sugar derivatives

## 1.1 Introduction and Rationale

Thailand is an agricultural-based country where lignocellulosic biomass can be considered as an important renewable energy resource for production of electricity, heat, liquid fuel, and commodity chemicals. This "biorefinery" concept can alleviate global warming due to the carbon neutral nature of the biomass and decrease the country's dependence of the depleting fossil resource. Biomass is the renewable resources (sustainable), which has its compositions similar to fossil fuel (contains C and H), and the products obtained from biomass are similar to those of petroleum. In details, lignocellulosic biomass is a multi-structure material. It consists mainly of three polymers *i.e.* cellulose, hemicelluloses, and lignin, which are associated with each other in addition to small amounts of acids, salts, and minerals. Currently several technologies, including catalytic, thermochemical, and biotechnological routes have been investigated for conversion of biopolymers-derived intermediates from

various agricultural wastes to a spectrum of value-added products. However, these technologies are thermochemically and/or biochemically conversion processes which are limited by some restrictions in practice, such as high cost of reagents and equipment, high energy consumption, and harsh reaction conditions. Some processes have to use high chemical contents and more production steps for efficient biomass conversion into fuels and chemicals. These cause high capital investment in term of energy input and chemical usage. The exploration of new routes for the production of platform chemicals or fuels from biomass thus becomes increasingly important.

Photocatalysis is one of promising processes for energy and chemical productions, because it can be performed under solar irradiation at room temperature and mild condition. It offers the possibility of extending the spectrum of applications to a variety of processes, including oxidations and oxidative cleavages, reductions, isomerizations, substitutions, condensations, and polymerizations. In addition, it is considered as clean, effective, energy-saving, technology simple, ecologically benign, and low cost strategy. Photocatalysis is a well-established technique for many applications, e.g. wastewater or air treatment, pollutant degradation, and hydrogen (clean fuel) production by water splitting. Titanium dioxide ( $\text{TiO}_2$ ) is the most important photocatalyst for many applications, such as degradation of organic pollutants (Hwang *et al.*, 2012), production of hydrogen (Gomathisankar *et al.*, 2013), self-cleaning surfaces (Murugan *et al.*, 2013), and dye sensitized solar cells (Cheng *et al.*, 2013).  $\text{TiO}_2$  is a white solid inorganic substance that occurs naturally in several kinds of rock and mineral sands. It is a semiconducting material, which can be chemically activated by light with band-gap energy ( $E_g$ ) of 3.2 eV.  $\text{TiO}_2$  exists in 3 different crystalline modifications, i.e. anatase, brookite, and rutile, where anatase exhibits the highest overall photocatalytic activity (Park *et al.*, 2013). It is a popular catalyst to use in photocatalytic reactions, because  $\text{TiO}_2$  has a highly oxidative, chemically stable, inexpensive, and nontoxic nature.  $\text{TiO}_2$  nanoparticles have been prepared by different methods such as, chemical precipitation (Mashid *et al.*, 2006), chemical vapor deposition (CVD) (Shi, J., & Wang, X., 2011), sputtering (Song *et al.*, 2009), sol-gel technique (Bahadur *et al.*, 2011), hydrolysis, micro-emulsion method (Shen *et al.*, 2011), aerosol-assisted chemical vapor deposition (Tahir *et al.*, 2012), spray deposition (Bujnova *et al.*, 2010), thermal plasma (Tanaka *et al.*, 2011), hydrothermal method (Oh *et al.*, 2009), microwave-assisted hydrothermal synthesis (Melis *et al.*, 2012), solvothermal method (Zhang *et al.*, 2009), and the flame combustion method (Zhao *et al.*, 2007). Among these methods, sol-gel method is one of the most popular techniques for preparation of nanosized metal oxide materials with high photocatalytic activities (Su *et al.*, 2004; Tseng *et al.*, 2010).

In this proposed project, the application of photocatalytic approach for chemical production will be investigated based on the close collaboration between JGSEE, BIOTEC, and The University of Kyoto under the JASTIP Renewable Energy collaboration. The work will include the development of novel photocatalysts for highly efficient conversion of sugars and lignin to value-added chemicals. Together with the design and assembly of photocatalytic reactor with the concept on development of bio-energy devices in combination with efficient utilization of solar energy by Kyoto U., this collaboration will provide strong platform alternative technology for utilization of biomass in bio-industry which will contribute to the government's strategy on new S-curve industry.

## 1.2 Project Scopes

This project aims to develop high performance photocatalysts and photocatalytic reactor for production of target chemicals from glucose which can be obtained from 1st generation or 2nd generation raw materials in biorefinery. The project will focus on synthesis and fabrication of nano-scaled photocatalysts with improved performance and characterization of physicochemical properties of self-synthesized photocatalysts compared to commercial catalysts. The work will include the study of photocatalytic reactions on synthesis of high-value products (functional sugar derivatives) from glucose and application of the developed photocatalysts for production of target chemicals in photocatalytic reactor. The specific technical objectives are as follows:

- (a) To study the effects of fabrication conditions, doping and surface modification on morphological appearances, physico-chemical properties, photocatalytic activity and selectivity of the photocatalysts
- (b) To study the effects of chemical structures of sugars on mechanisms of photocatalytic reactions
- (c) To study the reaction pathways for photocatalytic conversion of sugars (e.g. glucose) to its derivatives or unconventional sugars
- (d) To design and assemble a prototype laboratory-scale photocatalytic reactor (photo bio-flow reactor)
- (f) To study the reaction kinetics on sugar conversion to target chemicals in photo-bio flow reactor

### 1.3 Project Progress

As a major imported of solar source, photocatalysis process is one of the promising technologies which can be applied under solar irradiation at room temperature and mild condition. Heterogeneous photocatalysis employs as an alternative semiconductor material. Among them titanium dioxide ( $\text{TiO}_2$ ) has been widely used to be the most attractive photocatalyst in term of chemical stability, non-toxicity, and expressed high photocatalytic activity [Pelaez, et al., 2012]. However, its main drawback is performed under UV light irradiation ( $\lambda < 380$  nm) corresponding to its large band gap energy. Therefore, modification of  $\text{TiO}_2$  with additional of dopant is an aiming for the absorption of photocatalyst shift to visible light [Liu, et al., 2011; Gong, et al., 2015]. Moreover, modified new material is a point of view to improve yield and selectivity of valuable products [Ong, et al., 2016; Xu, et al., 2016, Kameyama, et al., 2015].

#### 1.3.1 Materials and method

##### 1.3.1.1 Materials

Titanium(IV) butoxide ( $\text{Ti}(\text{OC}_2\text{H}_9)_4$ ; Sigma-Aldrich, USA), acetylacetone (ACA; Sigma-Aldrich, USA), and isopropyl alcohol (Sigma-Aldrich, USA) were used to prepare titanium dioxide ( $\text{TiO}_2$ ) sol. All chemical for non-metal source include glucose ( $\text{C}_6\text{H}_{12}\text{O}_6$ ); boric acid ( $\text{H}_3\text{BO}_3$ ); ammonia ( $\text{NH}_3$ ), and metals source: copper nitrate trihydrate ( $\text{Cu}(\text{NO}_3)_2$ ); silver nitrate ( $\text{AgNO}_3$ ); chromium(II) acetate ( $\text{Cr}_2(\text{CH}_3\text{CO}_2)_4(\text{H}_2\text{O})_2$ ); indium(III) nitrate hydrate ( $\text{In}(\text{NO}_3)_3 \cdot 3\text{H}_2\text{O}$ ); nickel(II) nitrate hexahydrate ( $\text{Ni}(\text{NO}_3)_2 \cdot 6\text{H}_2\text{O}$ ); Strontium nitrate ( $\text{Sr}(\text{NO}_3)_2$ ) were manufactured from (Wako, Japan) for modification of  $\text{TiO}_2$ . Acetonitrile (ACN; RCI Labscan Co., Ltd., Thailand). Glucose monohydrate was obtained from Carlo Erba Reagents Co. (France) for photocatalytic reaction.

##### 1.3.1.2 Synthesis of $\text{TiO}_2$ photocatalyst nanoparticle

A series of pure, non-metal and metal doped on  $\text{TiO}_2$  were prepared using a sol-gel method. In details, a titanium precursor solution was prepared by mixing 4.36 ml of titanium butoxide with 1.26 ml of acetyl acetone under continuous stirring at room temperature which referred as solution A. Then, solution B was prepared by mixing 20 ml of 2-propanol, 15 ml of DI water and appropriate amount of non-metal and metal dopant. After that, solution B was added dropwise to solution A under continuous stirring. The resultant mixture was stirred for 3 hours at room temperature, followed by aging in oil bath at  $80^\circ\text{C}$  for 12 h. The obtained gel was dried by hot-pate at  $100^\circ\text{C}$  for 8 h. Finally, dry particles were grounded and calcined in a muffle furnace at  $400^\circ\text{C}$  for 3 h to obtain  $\text{TiO}_2$  powders.

##### 1.3.1.3 Synthesis of $\text{TiO}_2$ photocatalyst nanofiber

$\text{TiO}_2$  nanofibers were synthesized based on the electrospinning method in an in-house design. The solution was performed in methanol (10 mL) with 0.8 g of poly(vinylpyrrolidone) (PVP; Mw) 1 300 000, Aldrich), 4 g of titanium(IV) butoxide (TiBu; Aldrich), and 1.175 g of acetylacetone (ACA; Aldrich). The obtained solution was stirred overnight (12 h) to obtain a homogenous solution. Then, the appropriate amount dopant was added into the solution and stirred overnight. The obtained spinning solution was loaded into a plastic syringe with the nozzle-end which adjustable of 22-gauge stainless steel needle. The emitting electrode of

positive polarity from a Gamma High Voltage Research power supply was connected to the nozzle, while the grounding electrode was attached to a sheet of aluminum, used as the stationary collector plate. The distance between nozzle-end and collector was applied of 15 cm. with an electrical potential of 15 kV. The flow rate of syringe pump was 1.0 ml h<sup>-1</sup>. The obtained fibers were collected approximately 5 hours under atmospheric condition to allow the complete hydrolysis. The electrospun fibers was then calcinated at 500°C for 2 hours.

In order to synthesized TiO<sub>2</sub> hollow nanofibers the in-house designed coaxial nozzle electrospinning was performed. The solution was prepared according to the previous procedure. Then, the solution was added two through syringe pumps. The flow rate of inner and outer were controlled at 1.0 ml h<sup>-1</sup> and 2.0 ml h<sup>-1</sup>, respectively. Further processes were conducted based on the previous procedure.

#### 1.3.1.4 Synthesis of graphitic carbon nitride (g-C<sub>3</sub>N<sub>4</sub>)

The g-C<sub>3</sub>N<sub>4</sub> (**Fig. 1**) was synthesized by thermal polymerization, 3 g of urea was put into a crucible which was then heated in a furnace at a rate of 4°C min<sup>-1</sup> and kept for 2 h at 500°C. After cooled down to room temperature, it was ground to powder for further experiment.

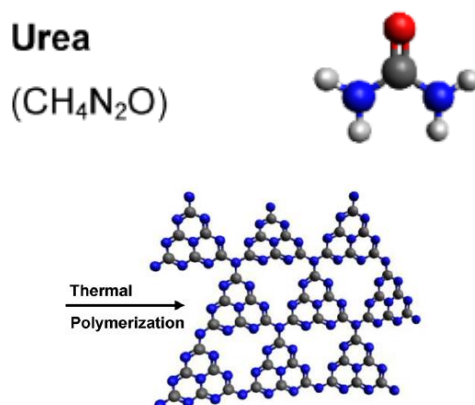


**Fig. 1.** Schematic structure of graphitic carbon nitride (g-C<sub>3</sub>N<sub>4</sub>) [Ong, W.J., et al., 2016]

#### 1.3.1.5 Synthesis of nanoparticles ZnS<sub>2(1-x)}</sub>-AgInS<sub>x</sub> (ZAIS(x))

The synthesis of quantum composite was studied according to previous method [Torimoto, et al., 2007]. Briefly, solid solution nanoparticles of ZnS-AgInS<sub>2</sub> were prepared by thermal decomposition of a metal ion-diethyldithiocarbamate complex of (AgIn)<sub>x</sub>Zn<sub>2(1-x)</sub>(S<sub>2</sub>CN(C<sub>2</sub>H<sub>5</sub>)<sub>2</sub>)<sub>4</sub>. The precursor powder was prepared by mixing 50 cm<sup>3</sup> of a sodium diethyldithiocarbamate aqueous solution (0.050 mol dm<sup>-3</sup>) with 50 cm<sup>3</sup> of an aqueous solution containing AgNO<sub>3</sub>, In(NO<sub>3</sub>)<sub>3</sub> and Zn(NO<sub>3</sub>)<sub>2</sub> with a mole ratio of x:x:2(1 - x) (total concentration of metal ions: 0.025 mol dm<sup>-3</sup>) followed by washing with water and methanol several times and drying. A 100 mg of precursor powder was put into a test tube and heat-treated at 180 °C for 3 min in an N<sub>2</sub> atmosphere. Then oleylamine (6.0 cm<sup>3</sup>) was added the thus-obtained brown powder, followed by further heat treatment at 180°C for 3 min in an N<sub>2</sub> atmosphere. The obtained mixture was centrifuged at 3,000 rpm for 5 min and the supernatant was collected by removing the larger particle. Suitable amount of methanol was added to the supernatant containing nanoparticles of ZAIS followed by centrifugation at 5,000 rpm for 5 min. The obtained ZAIS precipitate was dispersed in toluene for further study.

### 1.3.1.6 Characterization of photocatalysts

The synthesized photocatalytic samples were characterized according to the following techniques: The morphologies appearances of photocatalyst was conducted by an emission scanning electron microscope (FESEM; HITACHI SU-6600) with the use of energy-dispersive X-ray (EDX). The specific surface area, pore size and pore volume of the samples were carried out according to Brunauer-Emmett-Teller (BET) method (BEL Japan, BELSORP 18) by N<sub>2</sub> desorption at 77 K. The optical properties were analyzed using diffuse reflectance UV-vis absorption spectrophotometry (JASCO V-550). The UV-visible absorption spectra were acquired as the dry-pressed vessel of the samples with applying BaSO<sub>4</sub> as the reference sample (UV-vis DRS; Jasco V-550). The absorption spectra were recorded in air at room temperature with an integrating sphere in the range of 200-800 nm. The band gap values were calculated based on Tauc plot equation.

$$\alpha hv = A(hv - E_g)^n$$

where A is a constant,  $\alpha$  is photo absorption coefficient,  $h\nu$  is photon energy,  $E_g$  is average energy gap, and  $n$  is 2 for allowed indirect transition. The photoluminescence spectra (PL) were measured at room temperature using a Spectro-fluorophotometer (PL; JASCO FP-8600) with excitation wavelength of 270 nm with the scanning range of 300-900 nm. The crystalline and phase analysis were determined by X-ray diffraction (XRD; Rigaku, Smartlab) using Cu-K $\alpha$  radiation with the angles scanning of 20-80° ( $2\theta$ ) at 40 kV and 30mA. The approximate crystalline size of sample was calculated using the Scherrer equation:

$$D = \frac{K\lambda}{\beta \cos \theta}$$

Where D is the crystalline size, the coefficient ( $K=0.94$ ),  $\beta$  is the full-width at half-maximum (FWHM) of the diffraction peak of anatase phase [101],  $\theta$  is diffraction angle, and  $\lambda$  is the wavelength of X-ray corresponding to the Cu K $\alpha$  irradiation ( $\lambda = 1.5406 \text{ \AA}$ )

### 1.3.1.7 Photocatalytic reaction of glucose under UV-light

The reaction was prepared in a mixture of distilled water and acetonitrile (10:90 v/v) (Colmenares et al., 2011). The prepared solution (400 ml) was transferred into a Pyrex cylindrical double-walled reactor. The concentration of glucose solution (1 g/l) and photocatalyst loading (1 g/l) were mixed together under dark condition and continuous stirring for 30 min to reach an absorption-desorption equilibrium. A mercury lamp 450 W (250-365 nm, UM-452, USHIO, Japan) located inside the reactor as a light source to irradiate the samples. The reaction temperature was maintained by a cooling water system at 25°C. The samples were taken from the photoreactor at specified times for analysis.

### 1.3.1.8 Photocatalytic reaction of glucose under visible-light

The glucose solution was prepared in a mixture of distilled water and acetonitrile (10:90 v/v) (Colmenares et al., 2011). The prepared solution was performed in quartz vessel with working volume of 3 ml. The various types of photocatalyst were presented in the photocatalytic reaction. The concentration of glucose solution (1 g/l) and photocatalyst loading (1 g/l) were mixed together under dark condition and continuous stirring for 30 min to reach an absorption-desorption equilibrium. The samples were irradiated under 450 W Xenon lamp equipped with controller (Wacom, Japan) and sharp cut-off filter (code number L38  $\lambda > 380$  nm and L42  $\lambda > 420$  nm; Hoya, Japan). The position between light source and reactor was fixed with 10 cm. The reaction temperature was maintained at room temperature ( $\sim 25^\circ\text{C}$ ). The samples were taken from the photoreactor at specified times for analysis by HPLC.

### 1.3.1.9 Products analysis

The samples were taken from the photoreactor at specified times. The liquid product was filtered by a 0.22- $\mu\text{m}$  nylon filter before analysis. The chemical products were monitored by a high performance liquid chromatography (HPLC, Shimadzu, LC-10AD pump, Japan) equipped with a refractive index detector (Shimadzu RID-10A, Japan). Separation was performed on an Aminex HPX-87H column (300 x 7.8 mm) (Bio-Rad, USA). The mobile phase was 5 mM sulfuric acid at a flow rate of 0.5 mL/min and injection volume was 20  $\mu\text{L}$ . HPLC was used for analysis of the content of organic products and glucose conversion.

### 1.3.2 Photocatalytic conversion of glucose to high value fuels and chemicals

$\text{TiO}_2$  photocatalyst was synthesized by combination of sol gel and microwave with different concentrations of a surfactant, called CTAB. The surface morphology of the photocatalyst was observed using a scanning electron microscope. It was found that the agglomeration of  $\text{TiO}_2$  photocatalyst decreased with increasing concentration of CTAB (**Fig. 2**). Therefore, the particle size of  $\text{TiO}_2$  decreased with increasing concentration of CTAB. This is due to CTAB could reduce the surface tension and made high dispersion of  $\text{TiO}_2$  precursor in the solution during the preparation process. In addition, CTAB could increase surface area of obtained catalysts, leading to high photocatalytic activity.

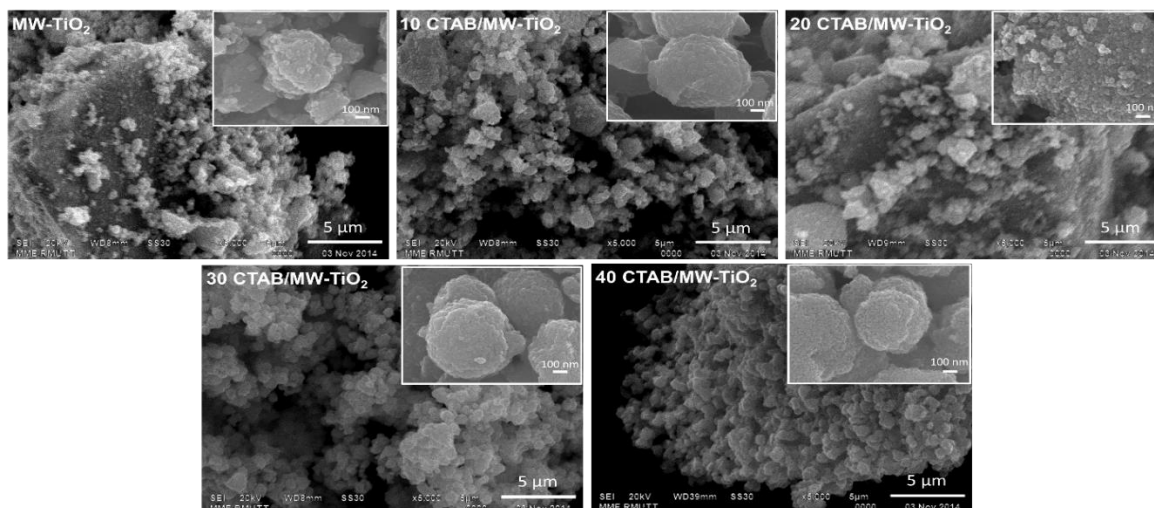


**Fig. 2.** SEM images of  $\text{TiO}_2$  photocatalysts synthesized with different concentrations of CTAB.

The glucose conversions of various catalysts were carried out for 120 min under UV irradiation (wavelength = 365 nm). The results showed that high concentration of CTAB resulted in high glucose conversion. The highest glucose conversion of 60% represented in 40 CTAB/MW- $\text{TiO}_2$ . It can conclude that high concentration of CTAB toward high surface area and low agglomeration of  $\text{TiO}_2$ , resulting in the highest glucose conversion (**Fig. 3**). The product yields of glucose conversion are shown in **Fig. 4**. There are 4 products of glucose conversion; gluconic acid, arabinose, xylitol, and formic acid. It was observed that the yields of all products tended to increase with increasing irradiation time. The highest conversion of 60% after 120 min showed the yield of gluconic acid, arabinose, xylitol, and formic acid of 5%, 26%, 3% and 25%, respectively. From the yields of products, it indicated that use of CTAB tended to give high yields of arabinose (**Fig. 3**).

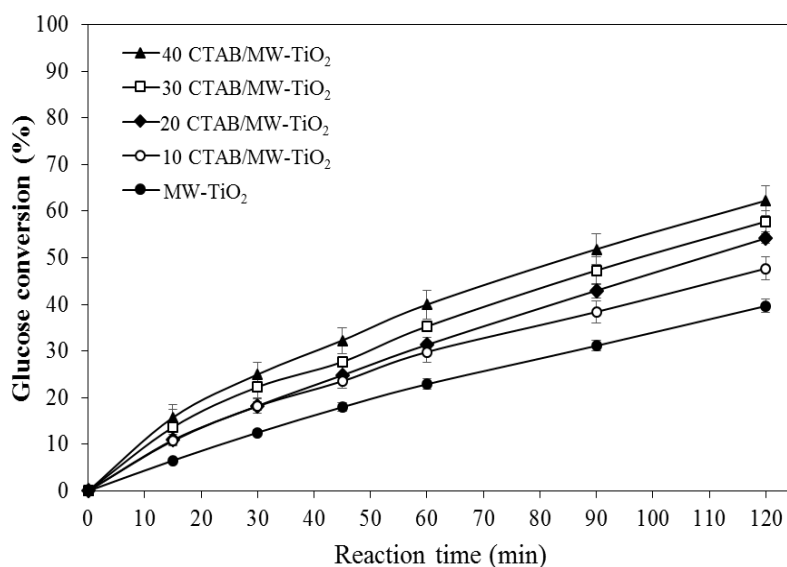


**Fig. 3.** Photocatalytic conversion of glucose with TiO<sub>2</sub> synthesized with different concentrations of CTAB in MW.

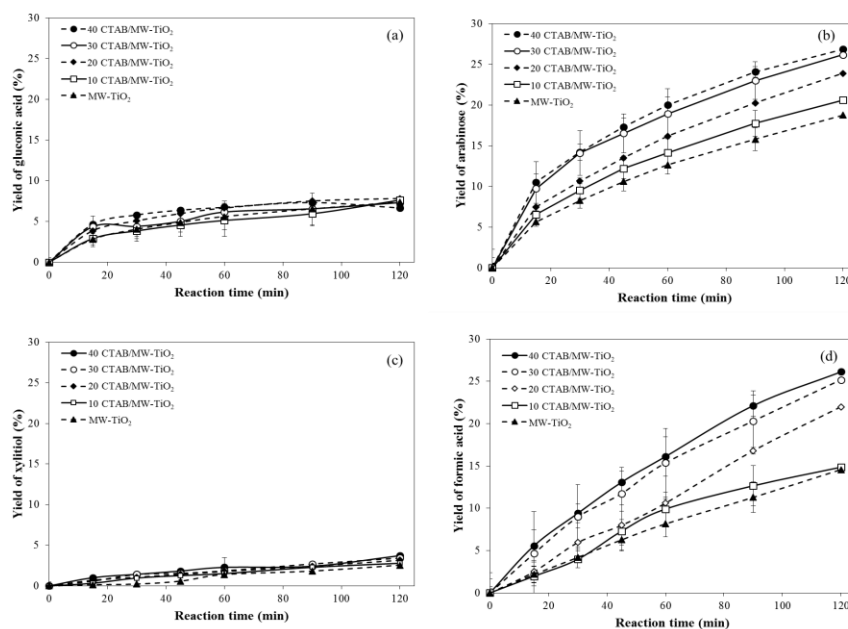


**Fig. 4.** Product yields of photocatalytic conversion of glucose with TiO<sub>2</sub> photocatalysts synthesized by different concentrations of CTAB.

As mentioned above, high surface area can enhance photocatalytic activity. So, the use of support materials is of interest for modification of TiO<sub>2</sub>. The supports are expected to decrease agglomeration of TiO<sub>2</sub> and increase selectivity of photocatalytic reactions. From the group of supports, zeolites have been reported to delocalize band gap excited electrons of TiO<sub>2</sub> and thereby minimize electron-hole recombination to favor photoinduced electron-transfer reactions. SEM images show that surface morphology of zeolite changed after TiO<sub>2</sub> loading. It was found that the TiO<sub>2</sub> particles were coated on the surface (see **Fig. 5**) compared with pristine zeolite. The TiO<sub>2</sub> coated on surface of zeolite showed well distribution. This

caused the reduction of the agglomeration of  $\text{TiO}_2$  nanoparticles synthesized with conventional process without zeolite. The catalyst size was increase when the amount of  $\text{TiO}_2$  increased. Therefore, it was found that the specific surface area of  $\text{TiO}_2/\text{ZeY}$  increase compared with pure  $\text{TiO}_2$ .

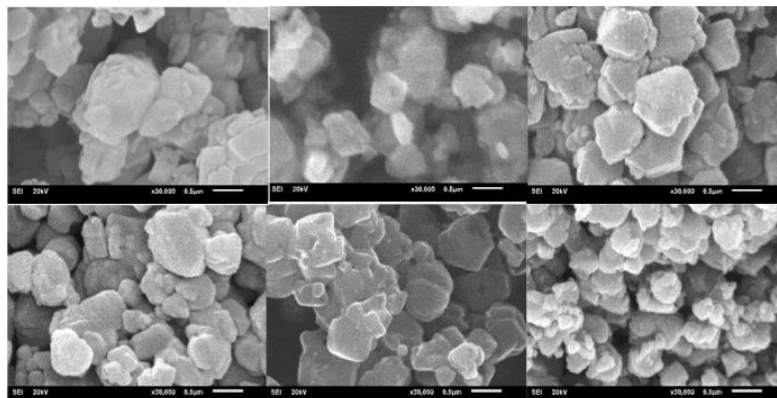


**Fig. 5.** SEM images (30000x) of ZeY,  $\text{TiO}_2(5\%)/\text{ZeY}(95\%)$ ,  $\text{TiO}_2(15\%)/\text{ZeY}(85\%)$ ,  $\text{TiO}_2(30\%)/\text{ZeY}(70\%)$ ,  $\text{TiO}_2(45\%)/\text{ZeY}(55\%)$ , and  $\text{TiO}_2$ .

The glucose conversion and organic compound yields increased with long irradiation time and reached a maximum value at 120 min. The results showed that zeolite supported  $\text{TiO}_2$  ( $\text{TiO}_2/\text{ZeY}$ ) represented higher photocatalytic conversion of glucose than pristine  $\text{TiO}_2$  (**Fig. 6**). However, it is distinct that the conversion rates did not increase linearly with increasing  $\text{TiO}_2$  content. Certainly, the highest glucose conversion was achieved at a medium loading of 15%  $\text{TiO}_2$  (75%) (Wang, C.C. *et al.* 2008). The yields of gluconic acid, arabinose, xylitol, and formic acid were 8.0, 29, 3, and 37%, respectively.

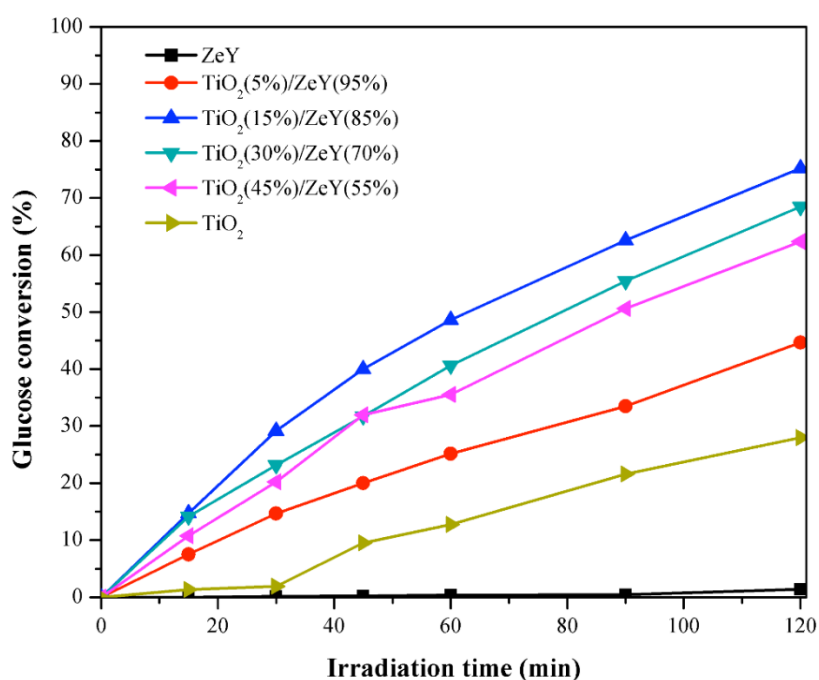


**Fig. 6.** Photocatalytic conversions of glucose under UV irradiation for 120 min with ZeY,

TiO<sub>2</sub>/ZeY (5, 15, 30, and 45 %wt), and TiO<sub>2</sub>.

### 1.3.3 Modification of photocatalyst by non-metal doping

The doping TiO<sub>2</sub> photocatalysts was synthesized by sol gel method. The precursors as boric acid, glucose, and ammonia were performed in order to presence the dopant of boron (B), carbon (C), and nitrogen (N), respectively. In this study, the amount of dopants are based on mole ratio of titanium, which varying ratio of dopant:Ti is 0.02:1 mole.

#### 1.3.3.1 Characterization of bare-TiO<sub>2</sub> and non-metal doped TiO<sub>2</sub>

SEM image of obtained photocatalyst sample are illustrated in **Fig. 7**. In this part, the morphology appearance of bare-TiO<sub>2</sub> and B,N-TiO<sub>2</sub> particles were compared. It could be observed that both samples have a large distribution of particle sizes. This could be described that the agglomeration from the synthesis in form of nanoparticles. Although, this phenomenon indicated that the non-spherical shape of photocatalyst. The dopant was no substantial alteration on the morphology appearance of photocatalyst.

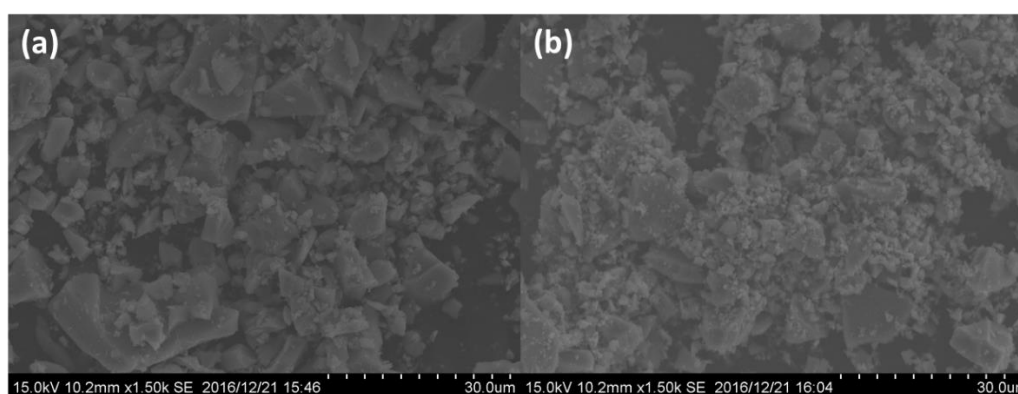


**Fig. 7.** SEM image of photocatalyst: (a) Bare-TiO<sub>2</sub>, and (b) B,N-TiO<sub>2</sub>

The surface area of modified TiO<sub>2</sub> with non-metal are shown in **Table 1**. The surface area remarkably increases with the presence of C, B, N, and BN, respectively. These results were corresponded with the performance on glucose conversion. The pore volume was also slightly increasing with the presence of dopant. Particularly, the presence of co-doping (B,N) gave the highest surface area with 227.69 m<sup>2</sup>/g. Thus, high surface area indicating to improve the active site on photocatalyst resulted in enhance of photocatalytic activity as the results in glucose conversion.

**Table 1.** The specific surface area of non-metal doped on TiO<sub>2</sub>

| Samples                   | Pore size (nm) | Pore volume (cm <sup>3</sup> /g) | Surface area (m <sup>2</sup> /g) |
|---------------------------|----------------|----------------------------------|----------------------------------|
| Bare TiO <sub>2</sub>     | 5.55           | 0.11                             | 77.92                            |
| B-doped TiO <sub>2</sub>  | 3.99           | 0.15                             | 147.37                           |
| C-doped TiO <sub>2</sub>  | 4.37           | 0.12                             | 109.20                           |
| N-doped TiO <sub>2</sub>  | 5.47           | 0.21                             | 153.04                           |
| B,N-dopedTiO <sub>2</sub> | 5.56           | 0.32                             | 227.69                           |

In addition, the increasing of conversion and productivity was also corresponded with the results of PL measurement as shown in **Fig. 8**. Typically, the photoluminescence spectra have been widely studied to investigate the change in the surface state and the efficient of charge trapping, immigration and transferring in semiconductor nanoparticles [Shamaila, et al., 2010]. It was found that doping of non-metal on  $\text{TiO}_2$  resulted in decrease the intensity on PL measurement. This could be described that the effective inhibited the recombination of electron and hole. This lead to increase the possibility of chemical reaction between radical and reactant resulting in achieve the performance on photocatalytic process [Srisasiwimon, et al., 2018].

UV-vis diffuse absorbance was demonstrated the optical properties of obtained photocatalysts (**Fig. 9**). It was found that bare- $\text{TiO}_2$  showed the lowest light absorption in the visible legion (400-700 nm). The presence of dopant on  $\text{TiO}_2$  presented a slightly shift of light absorption. Based on Tauc plots (**Fig. 10**), the band gap energies of bare- $\text{TiO}_2$  was calculated with approximate 3.18 eV which corresponded to the typical band gap of anatase  $\text{TiO}_2$ . Further, the narrow band gap energies of doping C, B, N, and BN on  $\text{TiO}_2$  were observed. A wide absorption region led to increase the excited electron under light irradiation resulted in high performance on glucose conversion [Liu, et al., 2011].

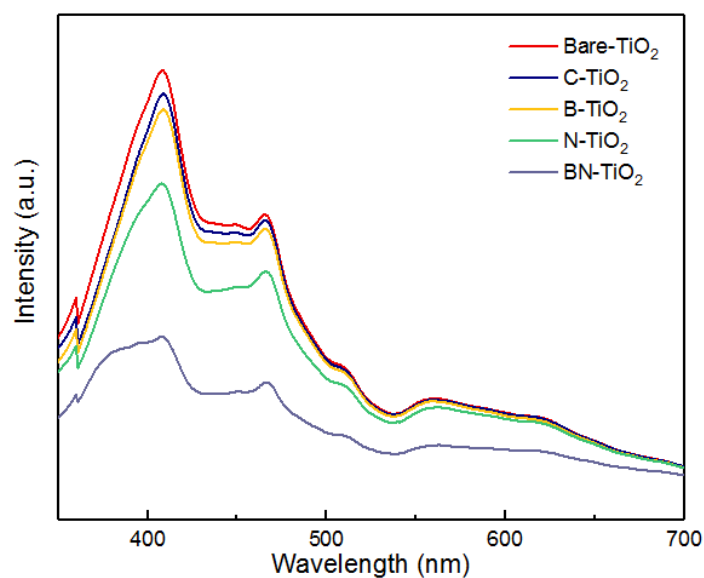


**Fig. 8.** Photoluminescence spectra of non-metals doped  $\text{TiO}_2$

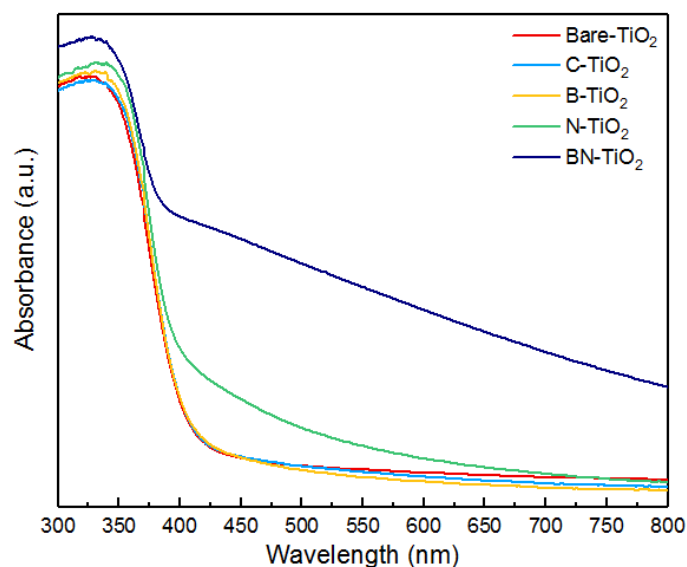


**Fig. 9.** UV-vis diffuse absorbance spectra of non-metal doped TiO<sub>2</sub>

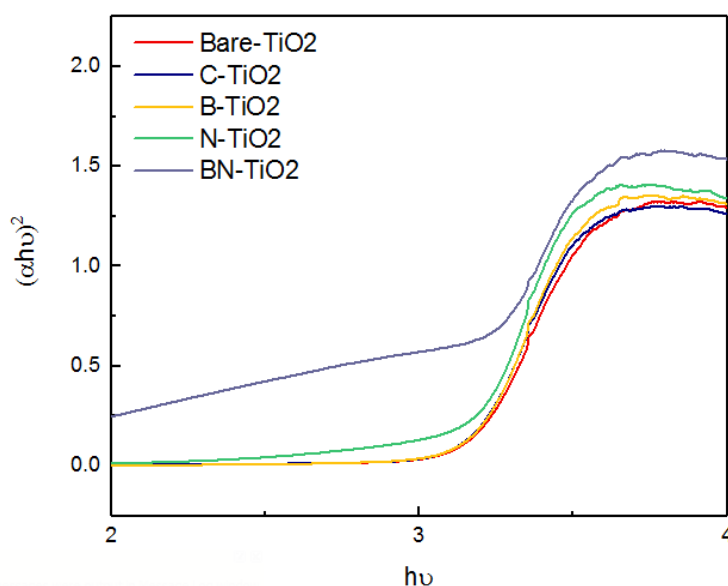


**Fig. 10.** Optical properties of non-metal doped TiO<sub>2</sub> based on Tauc plots equation

Typically, the different crystal phase affects the photocatalytic activity. Among them, anatase phase have been reported with high performance of photocatalyst. In this research, the non-metal doping on TiO<sub>2</sub> nanoparticles was carried out at 400 °C for 2 hours. The phase characterization of photocatalyst was measured by XRD techniques and the patterns are shown in **Fig. 11**. As the results, all of samples consist of anatase form as a unique phase. It was found that the strong peak was observed with (10 1) plane at  $2\theta = 25.4^\circ$  as anatase phase reflection. Therefore, the average crystalline sizes of all samples were calculated by well-known Scherrer formula as shown in **Table 2**. The crystalline size of non-metal doping was smaller compared to bare-TiO<sub>2</sub>. This could be ascribed that introducing of dopant would be affected a little distortion in the crystalline structure [Fu, et al., 2016].

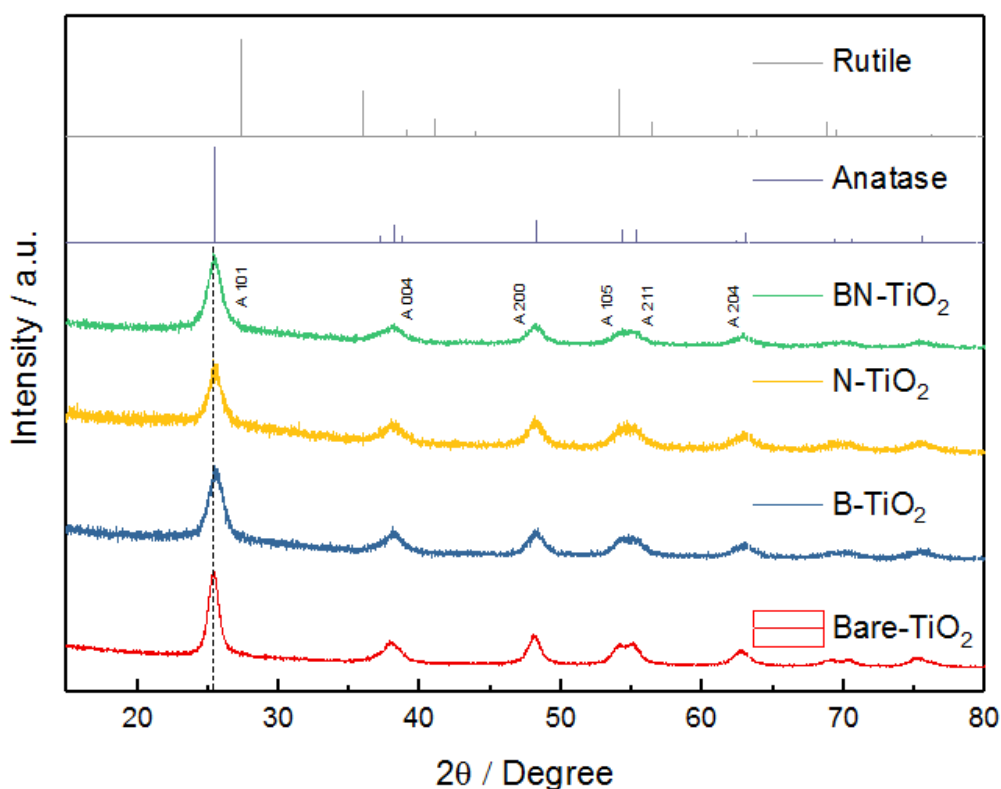


**Fig. 11.** XRD diffraction pattern of bare-TiO<sub>2</sub> and non-metal doped TiO<sub>2</sub>

**Table 2.** The crystalline size of non-metal doped TiO<sub>2</sub>

| Photocatalysts        | Crystal phase (%) |        | Crystallite size (nm) |
|-----------------------|-------------------|--------|-----------------------|
|                       | Anatase           | Rutile |                       |
| Bare-TiO <sub>2</sub> | 100               | -      | 9.59                  |
| B-TiO <sub>2</sub>    | 100               | -      | 7.31                  |
| N-TiO <sub>2</sub>    | 100               | -      | 7.56                  |
| B,N-TiO <sub>2</sub>  | 100               | -      | 7.35                  |

### 1.3.3.2 The performance of non-metal doped TiO<sub>2</sub> on glucose conversion

The glucose conversion of non-metal doped TiO<sub>2</sub> is shown in **Fig. 12**. Bare-TiO<sub>2</sub> showed the conversion with 24.9% under UV-light. According to the results, the presence of non-metal doping (B, C, and N) could be enhance glucose conversion compared with benchmark. The single doping of nitrogen on TiO<sub>2</sub> was improved the glucose conversion with 60.3%. In addition, modified TiO<sub>2</sub> with co-doping of boron and nitrogen showed the highest glucose conversion up to 93.1% for 180 min (**Fig. 13**). The products yield of gluconic acid, arabinose, xylitol, and formic acid were 9.0, 30.5, 8.9 and 47.6%, respectively. However, time course-change of product profile was almost the same for all photocatalyst.

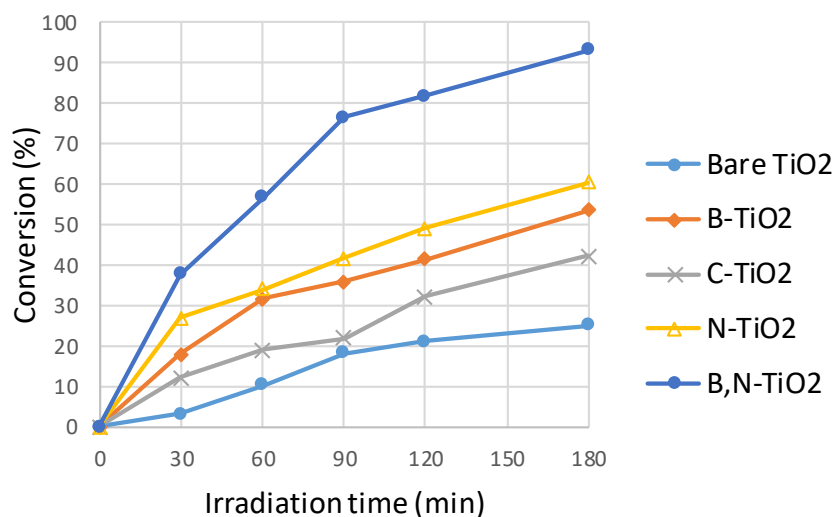


**Fig. 12.** Photocatalytic conversion of glucose under UV irradiation for 180 min in the presence of non-metal doping on TiO<sub>2</sub>

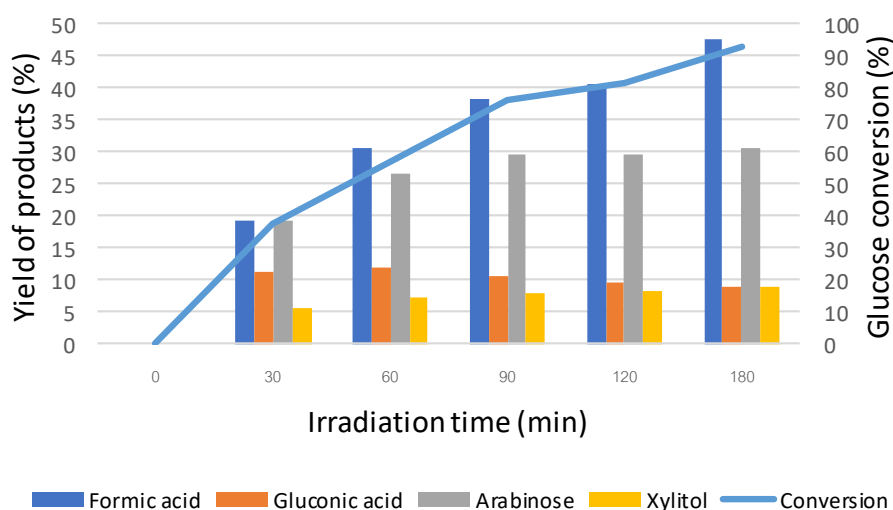


**Fig. 13.** The product profile of glucose conversion under UV irradiation for 180 min B,N doped TiO<sub>2</sub>

### 1.3.3.3 Rate of reaction on photocatalytic glucose conversion

**Table 3.** demonstrate the reaction rate of photocatalytic glucose conversion. It could be seen that the bare-TiO<sub>2</sub> showed a slight increasing of reaction rate, until retention time of 90 min gave the highest rate of 0.9 mmol L<sup>-1</sup> h<sup>-1</sup>. On the other hand, the doping photocatalyst could be enhance the performance on glucose conversion with short reaction time. The rapid reaction was occurred within 90 min and then slightly lower until final reaction time. For example, B,N-TiO<sub>2</sub> showed the highest reaction rate at 30 min with 3.5 mmol L<sup>-1</sup> h<sup>-1</sup>. The derived products of all photocatalysts were presented in different reaction rate. However, performed in batch processing showed the same characteristic of products in term of selectivity for all photocatalysts as previously proposed the reaction pathway of glucose

conversion [Payormhorm, et al., 2017]. Further research, the reaction will be carried out in photocatalytic bio-flow reactor in order to study the kinetic reaction for improving the selectivity and yield of derived products.

**Table 3.** Reaction rate of non-metal doped TiO<sub>2</sub> nanoparticles

| Catalyst              | Time (min) | Reaction rate (mmol L <sup>-1</sup> h <sup>-1</sup> ) | Products rate (mmol L <sup>-1</sup> h <sup>-1</sup> ) |           |         |             |
|-----------------------|------------|---|---|-----------|---------|-------------|
|                       |            |   | Gluconic acid   | Arabinose | Xylitol | Formic acid |
| Bare-TiO <sub>2</sub> | 30         | 0.3   | 0.00  | 0.29      | 0.06    | 1.34        |
|                       | 60         | 0.8   | 0.29  | 0.18      | 0.07    | 0.48        |
|                       | 90         | 0.9   | 0.17  | 0.22      | 0.04    | 0.44        |
|                       | 120        | 0.3   | 0.12  | 0.16      | 0.05    | 0.55        |
|                       | 180        | 0.2   | 0.02  | 0.03      | 0.05    | 0.48        |
| B-TiO <sub>2</sub>    | 30         | 1.9   | 0.35  | 0.86      | 0.15    | 2.38        |
|                       | 60         | 1.5   | 0.07  | 0.45      | 0.21    | 1.28        |
|                       | 90         | 0.4   | 0.08  | 0.58      | 0.14    | 1.40        |
|                       | 120        | 0.6   | 0.06  | 0.43      | 0.12    | 1.36        |
|                       | 180        | 0.7   | -0.04   | 0.21      | 0.05    | 0.95        |
| N-TiO <sub>2</sub>    | 30         | 2.8   | 0.37  | 1.10      | 0.24    | 3.16        |
|                       | 60         | 0.8   | 0.18  | 0.68      | 0.20    | 2.05        |
|                       | 90         | 0.8   | 0.06  | 0.48      | 0.11    | 1.64        |
|                       | 120        | 0.8   | 0.05  | 0.29      | 0.05    | 1.31        |
|                       | 180        | 0.6   | -0.07   | 0.25      | 0.07    | 1.26        |
| B,N-TiO <sub>2</sub>  | 30         | 3.5   | 0.92  | 2.09      | 0.58    | 6.74        |
|                       | 60         | 1.7   | 0.07  | 0.79      | 0.20    | 4.00        |
|                       | 90         | 1.8   | -0.11   | 0.30      | 0.07    | 2.77        |
|                       | 120        | 0.5   | -0.10   | 0.00      | 0.01    | 0.83        |
|                       | 180        | 0.5   | -0.02   | 0.06      | 0.04    | 1.19        |

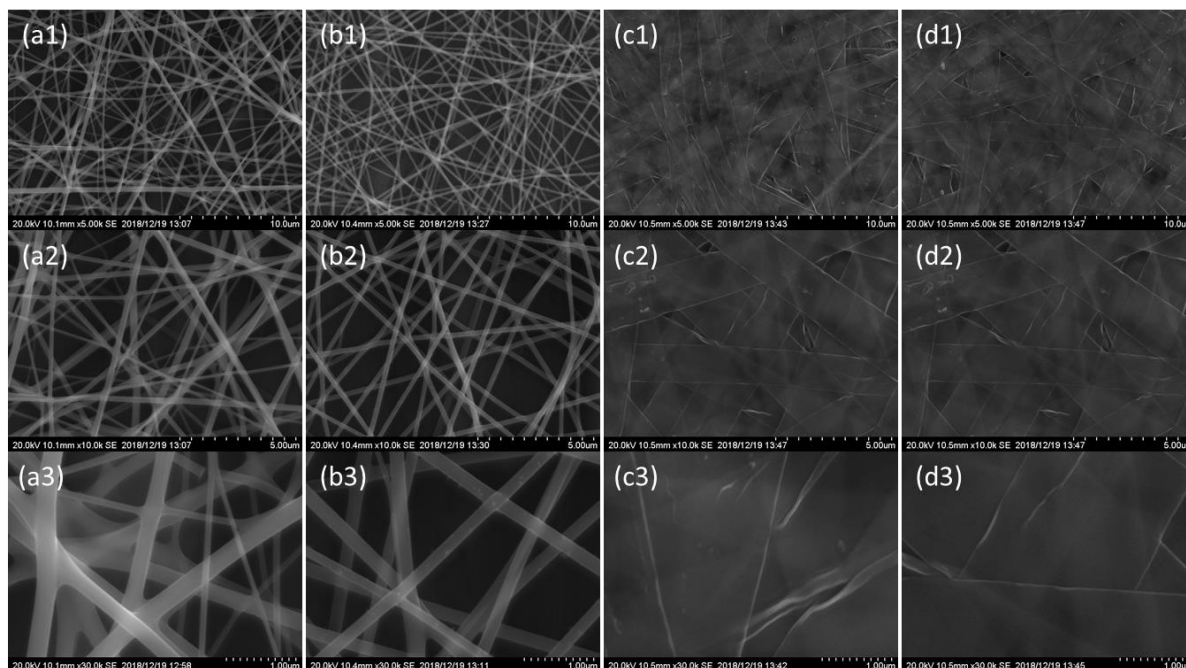
### 1.3.4 Further extension of the catalyst design (1): Preparation of B,N-TiO<sub>2</sub> nanofibers and hollow nanoribbons and Ag-loaded TiO<sub>2</sub> nanofibers

In the above section of 1.3.3, nonmetal B,N-doped TiO<sub>2</sub> resulted in the highest catalytic activity for conversion of glucose (**Fig. 12**). In this context, we newly prepared B,N-doped TiO<sub>2</sub> nanofibers and B,N doped TiO<sub>2</sub> hollow nanoribbons by electrospinning technique in order to improve the catalytic activity through increment of the specific surface area (*viz.* active site) of the catalyst. Further characterization and evaluations of the catalytic activity for conversion of glucose under the illumination of the light are still underway.

#### 1.3.4.1 Characterization of bare-TiO<sub>2</sub> and non-metal doped TiO<sub>2</sub> nanofiber and hollow nanoribbon

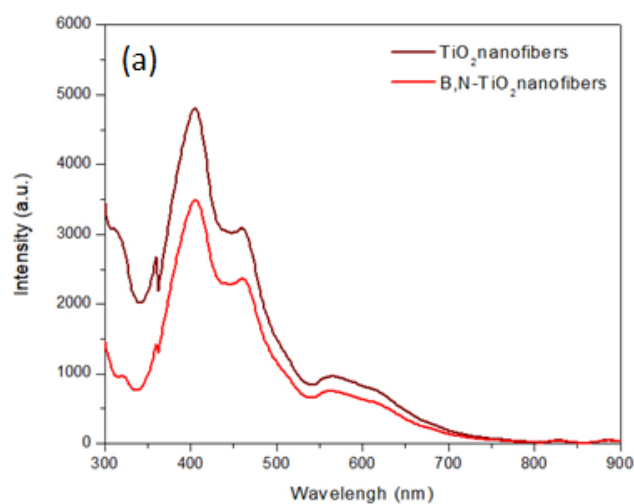
The morphologies appearance of electrospinning technique of TiO<sub>2</sub> nanofibers and hollow-nanofibers by SEM method are illustrated in **Fig. 14**. The first synthesized photocatalyst in form of nanofiber was showed in **Fig. 14 (a and b)**. Although the nanofiber showed a smooth morphology of fiber, however, a slight distribution of sizes in both of pristine and doped TiO<sub>2</sub> were observed. The average diameter of B,N doped TiO<sub>2</sub> was approximately 150 μm. Further, the hollow-nanofiber of TiO<sub>2</sub> and doped TiO<sub>2</sub> was studied by coaxial nozzle electrospinning technique as illustrated in **Fig. 14 (c and d)**. However, the obtained fiber was found in form of hollow-nanoribbon for both samples. Despite, the good

morphologies of hollow-nanoribbons were obtained (smooth and uniform in the distribution of size). This could be further study the suitable condition in term of flow rate to obtain the hollow-nanofibers.



**Fig. 14.** SEM image of (a)  $\text{TiO}_2$  nanofibers, (b) BN doped  $\text{TiO}_2$  nanofiber, (c)  $\text{TiO}_2$  nanoribbon, and (d) BN doped  $\text{TiO}_2$  nanoribbon. The scale bar in figures with suffix “1” is 10  $\mu\text{m}$ , “2” is 5  $\mu\text{m}$ , and “3” is 1  $\mu\text{m}$ .

**Fig. 15** shows the photoluminescence spectra comparison of  $\text{TiO}_2$  and B,N doped  $\text{TiO}_2$  nanofibers. The modified photocatalyst expressed the lower PL intensity resulting in decrease in the recombination of electron and holes (**Fig. 15a**). However, the comparison of PL pattern of hollow nanoribbon was no substantial alteration (**Fig. 15b**).



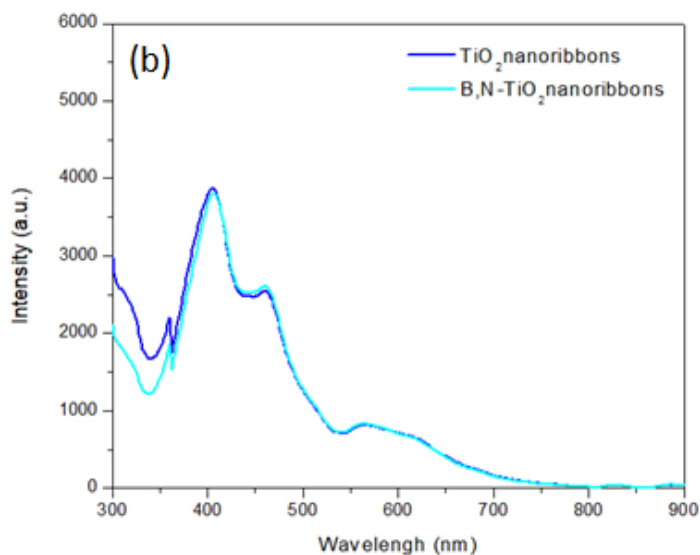


**Fig. 15.** Photoluminescence spectra of bare-TiO<sub>2</sub> and B, N doped TiO<sub>2</sub> (a) nanofiber and (b) hollow-nanoribbon.

**Fig. 16** shows the XRD patterns of the nanofiber and hollow nanoribbon. The structural features obtained from XRD are summarized in **Table 4**. All samples showed very broad peak with (1 0 1) plane at  $2\theta = 25.4^\circ$  indicate anatase phase reflection. As a result, the lower crystalline size of doped TiO<sub>2</sub> both nanofiber and nanoribbon were observed. This could be ascribed that the substitute of B and N in the crystalline of TiO<sub>2</sub> [Fu, et al., 2016].

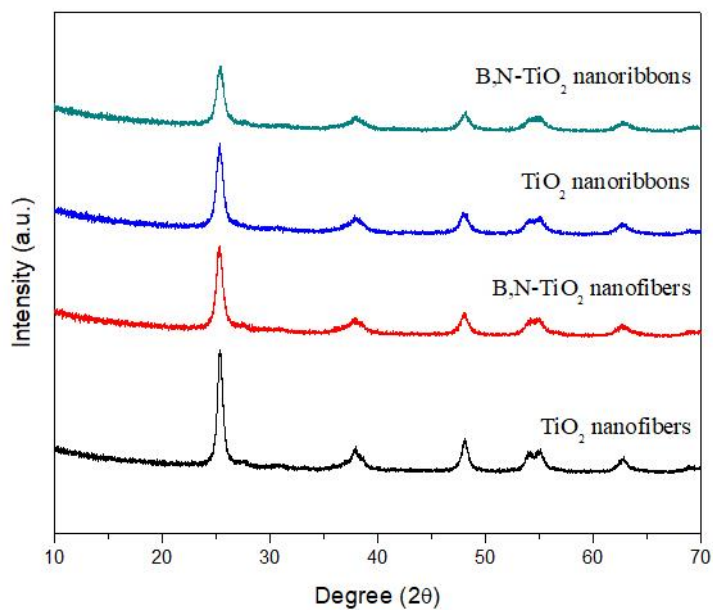


**Fig. 16.** XRD diffraction pattern of nanofibers and nanoribbons

**Table 4.** The crystalline size of nanofibers and nanoribbons

| Photocatalysts                  | Crystal phase (%) |        | Crystallite size (nm) |
|---------------------------------|-------------------|--------|-----------------------|
|                                 | Anatase           | Rutile |                       |
| TiO <sub>2</sub> nanofiber      | 100               | -      | 12.79                 |
| B,N-TiO <sub>2</sub> nanofiber  | 100               | -      | 10.66                 |
| TiO <sub>2</sub> nanoribbon     | 100               | -      | 10.34                 |
| B,N-TiO <sub>2</sub> nanoribbon | 100               | -      | 9.77                  |

#### 1.3.4.2 The performance of fibrous TiO<sub>2</sub> on glucose conversion

Particularly, Ag-loaded TiO<sub>2</sub> nanofibers were also prepared and applied them for photoconversion of glucose. Although it has not yet been optimized the conditions for preparation of the Ag-loaded TiO<sub>2</sub> nanofibers in terms of the photocatalytic activity, in situ preparation in N<sub>2</sub> resulted in the highest activity (**Fig. 17**).

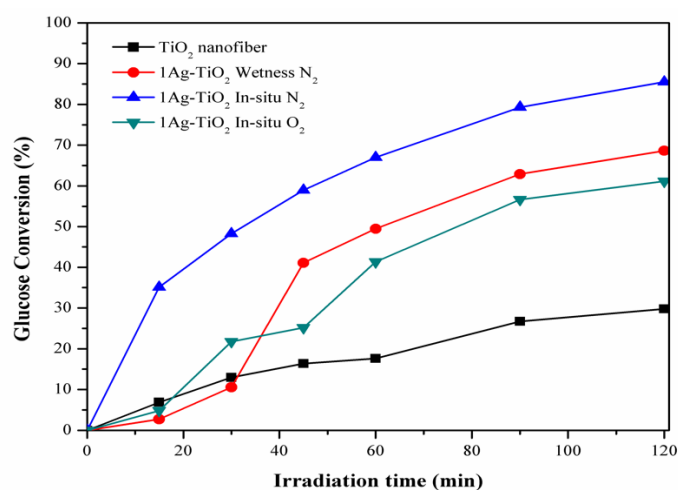


**Fig. 17.** Time-course conversion of glucose under UV irradiation for 2 h with Ag-loaded TiO<sub>2</sub> nanofibers prepared by different techniques.

#### 1.3.5 Modification of photocatalyst by metal doping

The doping TiO<sub>2</sub> photocatalysts was synthesized by sol gel method. The several precursors were performed in order to presence the metal dopant on titanium dioxide. In this study, the amount of dopants are based on mole ratio of titanium, which varying ratio of dopant:Ti is 0.02:1 mole.

##### 1.3.5.1 Characterization of bare-TiO<sub>2</sub> and metal doped TiO<sub>2</sub>

According to the results in **Fig. 18.**, It was found that the photocatalyst in form of nanoparticles showed a large distribution of particles sizes due to the agglomeration of nanoparticles **Fig. 18a**. For example, the agglomeration also found in modified photocatalyst (**Fig. 18b**). However, the dopant was no substantial effect on the morphology appearance.

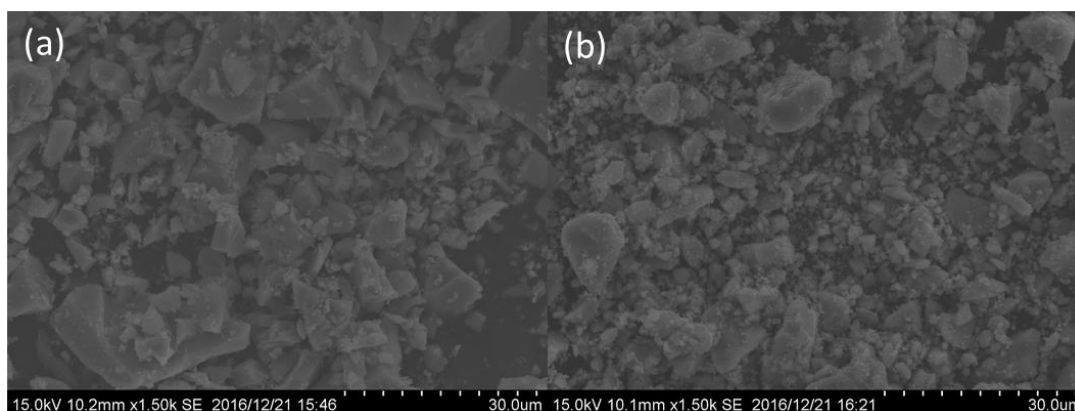


**Fig. 18.** SEM image of photocatalyst: (a) Bare-TiO<sub>2</sub>, and (b) Sr-TiO<sub>2</sub>

The surface area of modified TiO<sub>2</sub> with metal are shown in **Table 5**. All modified photocatalysts with metal dopant led to an increase of specific surface area and pore volume, while a slightly decreasing of pore size was observed. This could be found that the decreasing of crystalline size was corresponding with a smaller crystalline size in XRD method. As the results, the presence of Sr-TiO<sub>2</sub> gave the highest surface area with 210.60 m<sup>2</sup>/g. This indicated the increasing of active site for improving the performance on photocatalytic activity [Payormhorm, et al., 2017].

**Table 5.** The specific surface area of metal doped on TiO<sub>2</sub>

| Samples                   | Pore size (nm) | Pore volume (cm <sup>3</sup> /g) | Surface area (m <sup>2</sup> /g) |
|---------------------------|----------------|----------------------------------|----------------------------------|
| Bare-TiO <sub>2</sub>     | 5.55           | 0.11                             | 77.92                            |
| Sr doped TiO <sub>2</sub> | 4.55           | 0.24                             | 210.60                           |
| In doped TiO <sub>2</sub> | 3.75           | 0.19                             | 202.77                           |
| Ag doped TiO <sub>2</sub> | 3.76           | 0.11                             | 114.95                           |
| Cr doped TiO <sub>2</sub> | 3.78           | 0.12                             | 125.31                           |
| Cu doped TiO <sub>2</sub> | 3.96           | 0.12                             | 124.07                           |
| Ni doped TiO <sub>2</sub> | 4.53           | 0.17                             | 147.75                           |

UV-vis diffuse absorbance was demonstrated the optical properties of obtained photocatalysts (**Fig. 19.**). It could be observed that Sr-TiO<sub>2</sub> and In-TiO<sub>2</sub> showed the lower light absorption in the visible legion (400-700 nm) compared to bare-TiO<sub>2</sub> as benchmark. In contrast, the presence of Ag, Cr, Cu, and Ni on TiO<sub>2</sub> presented a broadly shift of light absorption in visible region. The results demonstrated the potential of photocatalyst for further applied in solar irradiation.

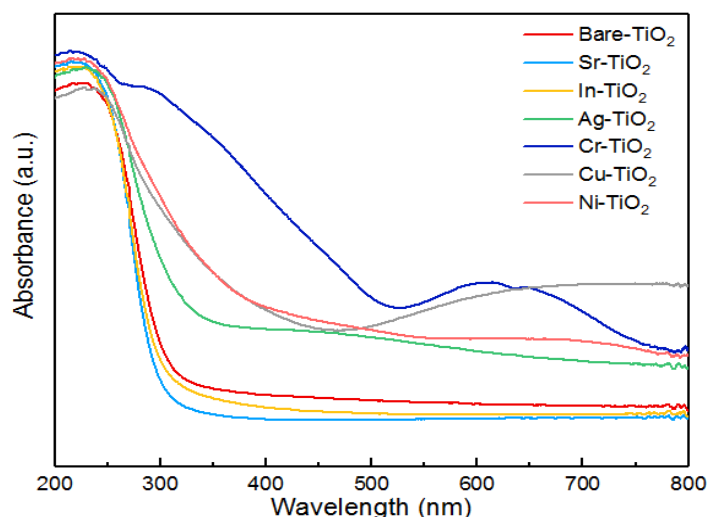


**Fig. 19.** UV-vis diffuse absorbance spectra of metal doped TiO<sub>2</sub>

The photoluminescence spectra of metal doped TiO<sub>2</sub> are demonstrated in **Fig. 20**. The PL measurement was examined to investigate the change in the surface state and the efficient of charge trapping, immigration and transferring in semiconductor nanoparticles [Shamaila, et al., 2010]. It could be observed that the intensity spectra of all samples were corresponded with the results of the ability of light absorption. According to the results, the presence of Ag, Cr, Cu, and Ni on TiO<sub>2</sub> led to decrease the intensity of PL spectra, whereas an increase in PL intensity with Sr and In doped on TiO<sub>2</sub> were observed. Typically, the decreasing an intensity of PL spectra indicated significantly high separation of charge carriers. In this study, the presence of metal on TiO<sub>2</sub> was no substantial correlation with the results on glucose conversion. However, the proper physio-chemical properties of photocatalyst should be determined with the combination of several techniques.

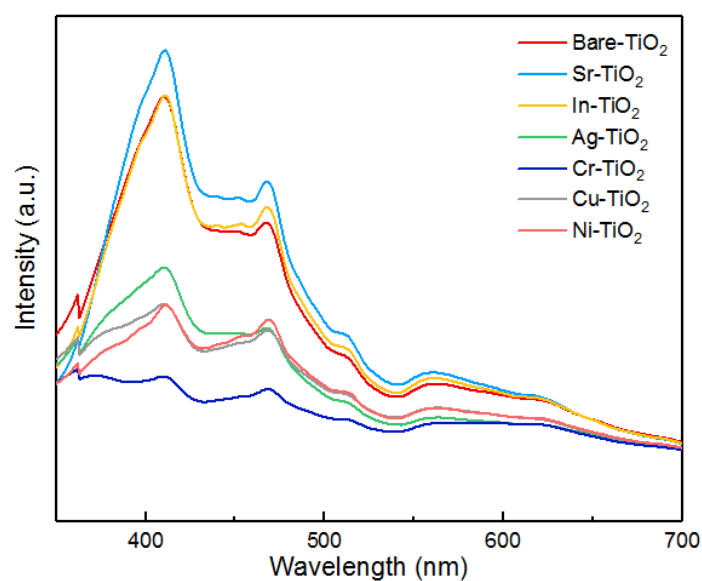


**Fig. 20.** Photoluminescence spectra of metals doped TiO<sub>2</sub>

The phase characterization of photocatalyst was measured by XRD techniques and the patterns are shown in **Fig. 21**. Previous reported have been demonstrated that anatase phase  $\text{TiO}_2$  was a proper form for an efficient in photocatalytic reaction [Kadam, et al., 2017]. In this study, all of samples consist of anatase form as a unique phase. It was found that the strong peak was observed with (1 0 1) plane at  $2\theta = 25.4^\circ$  as anatase phase reflection. Therefore, the average crystalline sizes of all samples were calculated by well-known Scherrer formula as shown in **Table 6**. The providing value of Full-Width-at-Half-Maximum (FWHM) of Ag, In and Sr were 1.4546, 1.4209, and 1.1382, respectively. According to the results, the wider FWHM was corresponded to a decrease of crystalline size. Therefore, the presence of metal dopant showed a smaller crystalline size than those of bare- $\text{TiO}_2$ . This could be ascribed that introducing of dopant would be affected a little distortion in the crystalline structure [Fu, et al., 2016].

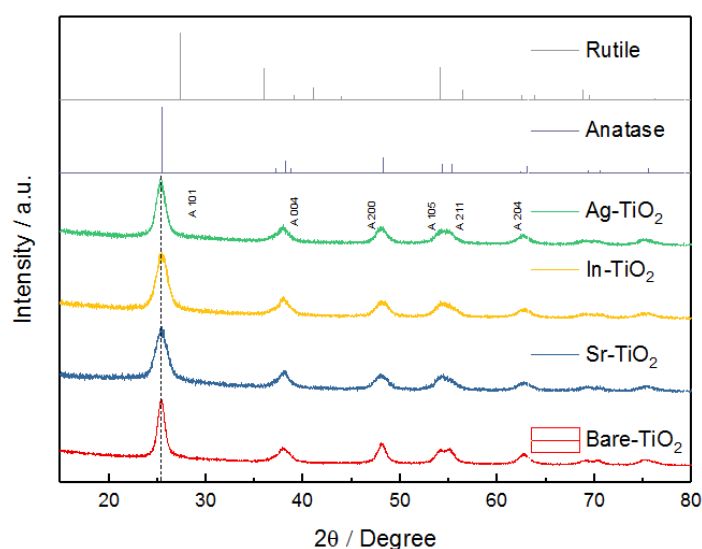


**Fig. 21.** XRD diffraction pattern of bare- $\text{TiO}_2$  and metal doped  $\text{TiO}_2$

**Table 6.** The crystalline size of metal doped  $\text{TiO}_2$

| Photocatalysts       | Crystal phase (%) |        | Crystallite size (nm) |
|----------------------|-------------------|--------|-----------------------|
|                      | Anatase           | Rutile |                       |
| Bare- $\text{TiO}_2$ | 100               | -      | 9.59                  |
| Sr- $\text{TiO}_2$   | 100               | -      | 5.81                  |
| In- $\text{TiO}_2$   | 100               | -      | 6.10                  |
| Ag- $\text{TiO}_2$   | 100               | -      | 7.41                  |

### 1.3.5.2 The performance of metal doped $\text{TiO}_2$ on glucose conversion

The glucose conversion of metal doped  $\text{TiO}_2$  is shown in **Fig. 22**. The Bare- $\text{TiO}_2$  was used as benchmark with glucose conversion of 24.9%. The modified photocatalyst with metal doping led to improve the efficiency except Cr- $\text{TiO}_2$ . The highest glucose conversion was obtained in the presence of Sr- $\text{TiO}_2$  (87.5%). The product profile of Sr- $\text{TiO}_2$  is shown in **Fig. 23**. The products yield of gluconic acid, arabinose, xylitol, and formic acid were 6.7, 33.7, 8.2 and 37.4%, respectively. However, time course-change of product profile was almost the same for all metal doped photocatalyst.

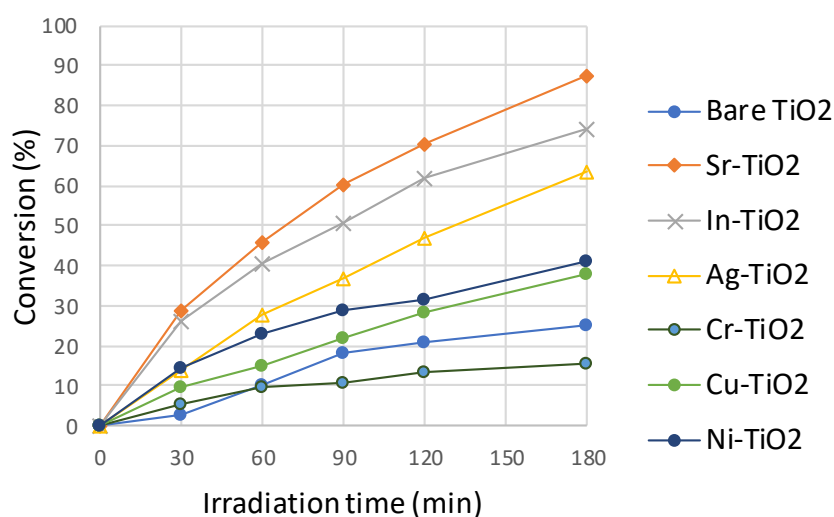


**Fig. 22.** Photocatalytic conversion of glucose under UV irradiation for 180 min in the presence of metal doping on TiO<sub>2</sub>

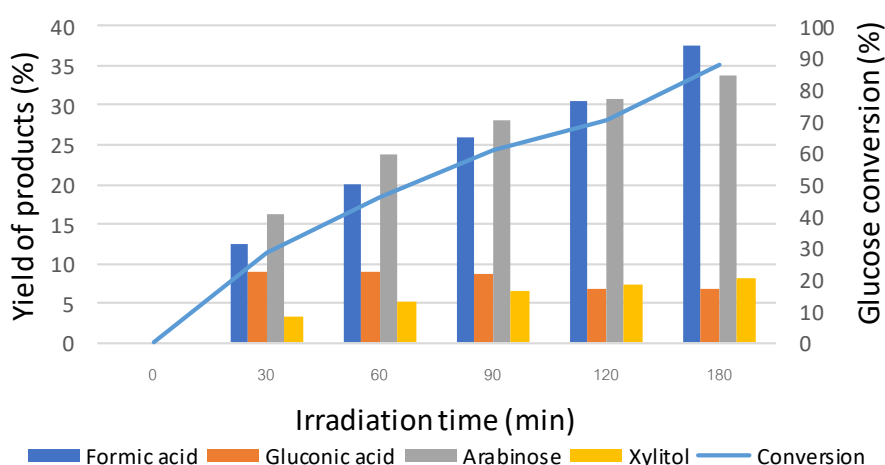


**Fig. 23.** The product profile of glucose conversion under UV irradiation for 180 min Sr doped TiO<sub>2</sub>

### 1.3.6 Modification of photocatalyst by synergistic effects of metal/nonmetal doping

The modification of photocatalyst in the concept of synergistic was investigated to improve the performance of photocatalysts on glucose conversion. According to previous results, a single of nonmetal doping as nitrogen showed the good photocatalyst properties for single nonmetal doping resulted in the highest glucose conversion. Thus, the nitrogen dopant is a representative for efficient nonmetal doping on TiO<sub>2</sub>. In this part, the synergistic effects of various metals/nonmetal (nitrogen) on the physio-chemical properties were studied. The doped TiO<sub>2</sub> photocatalysts were synthesized by sol gel method. Several precursors were studied in order to modify the metal/nonmetal dopant on titanium dioxide.

In this study, the amount of dopants are based on mole ratio of titanium, which varying ratio of dopant:Ti was 0.02:1 mole.

### 1.3.6.1 Characterization of bare-TiO<sub>2</sub> and synergistic metal/nonmetal doped TiO<sub>2</sub>

The synergistic effects of metal/nonmetal doping on physio-chemical properties were studied. SEM image of obtained photocatalyst sample are illustrated in **Fig. 24**. The morphology appearance of metal/nonmetal doped TiO<sub>2</sub> particles (Ag,N-TiO<sub>2</sub>, and Cr,N-TiO<sub>2</sub>) were compared with bare-TiO<sub>2</sub>. It could be observed that all photocatalyst samples showed the same morphology with a random arrangement of particle sizes. According to result, the large distribution in form of nanoparticle enhanced the agglomeration of samples. Although, this phenomenon indicated that the non-spherical shape of photocatalyst. The dopant was shown to have no substantial effect on alteration on the morphology appearance of photocatalyst.

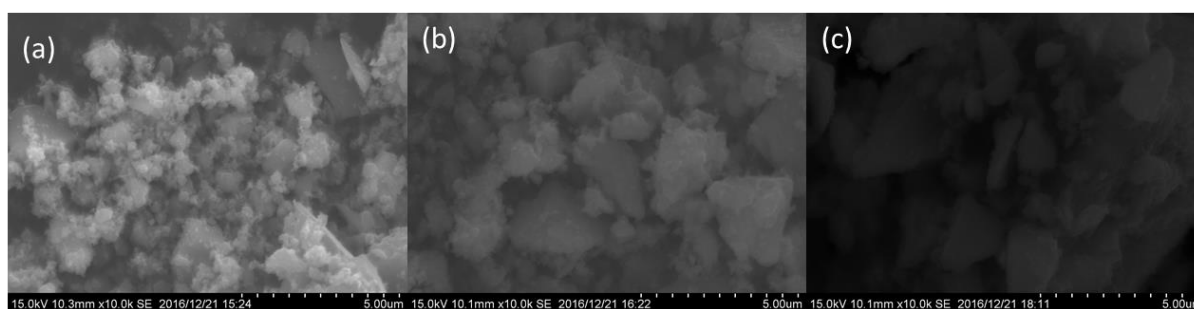


**Fig. 24.** SEM image of photocatalyst: (a) Bare-TiO<sub>2</sub>, (b) Ag,N-TiO<sub>2</sub> and (c) Cr,N-TiO<sub>2</sub>.

Pore size, pore volume, and surface areas of metal/nonmetal doped TiO<sub>2</sub> are shown in **Table 7**. It was observed that the surface area of bare-TiO<sub>2</sub> was 77.92 m<sup>2</sup>/g. The surface area was remarkably increased in the presence of metal/nonmetal dopant. Among the synthesized catalysts, the Sr,N-TiO<sub>2</sub>, In,N-TiO<sub>2</sub>, and B,N-TiO<sub>2</sub> showed the relative high surface area with 251.97, 242.34, and 227.69 m<sup>2</sup>/g, respectively. All modified photocatalyst showed a slightly increasing of pore size and pore volume compared with bare-TiO<sub>2</sub>. However, a similar trend of pore size and pore volume for doping samples were observed. In this study, the high surface area is the main criteria which led to improved activity of the photocatalytic conversion.

**Table 7.** The specific surface area of metal doping on TiO<sub>2</sub>

| Samples                     | Pore size<br>(nm) | Pore volume<br>(cm <sup>3</sup> /g) | Surface area<br>(m <sup>2</sup> /g) |
|-----------------------------|-------------------|-------------------------------------|-------------------------------------|
| Bare-TiO <sub>2</sub>       | 5.55              | 0.11                                | 77.92                               |
| B,N doped TiO <sub>2</sub>  | 5.56              | 0.32                                | 227.69                              |
| Ag,N doped TiO <sub>2</sub> | 6.73              | 0.26                                | 152.42                              |

|                             |      |      |        |
|-----------------------------|------|------|--------|
| In,N doped TiO <sub>2</sub> | 5.74 | 0.35 | 242.34 |
| Sr,N doped TiO <sub>2</sub> | 5.39 | 0.34 | 251.97 |
| Cr,N doped TiO <sub>2</sub> | 5.70 | 0.25 | 174.91 |
| Cu,N doped TiO <sub>2</sub> | 8.79 | 0.24 | 110.19 |
| Ni,N doped TiO <sub>2</sub> | 5.28 | 0.21 | 150.98 |

UV-vis diffuse absorbance was studied to demonstrate the optical properties of the obtained photocatalysts (**Fig. 25**). It was found that the bare-TiO<sub>2</sub> showed no significant absorption in the visible-light region (400-700 nm) due to a large band gap. All metal/nonmetal photocatalyst showed remarkable generate of light absorption in visible region. This notable increase in absorbance reflected the synergism for In,N-TiO<sub>2</sub> and Sr,N-TiO<sub>2</sub> on property of light absorption characteristic of TiO<sub>2</sub>. Further increasing with two region absorption for Cr,N-TiO<sub>2</sub> and Cu,N-TiO<sub>2</sub> were observed. Based on Tauc plots (**Fig. 26**), the band gap energies of bare-TiO<sub>2</sub> was calculated with approximate 3.18 eV which corresponded to the typical band gap of anatase TiO<sub>2</sub>. Narrower band gap energies of metal/nonmetal doped TiO<sub>2</sub> were observed. A narrow band gap led to the increase in the excited electron under light irradiation, resulting in improved performance of photocatalyst (Liu et al., 2011).

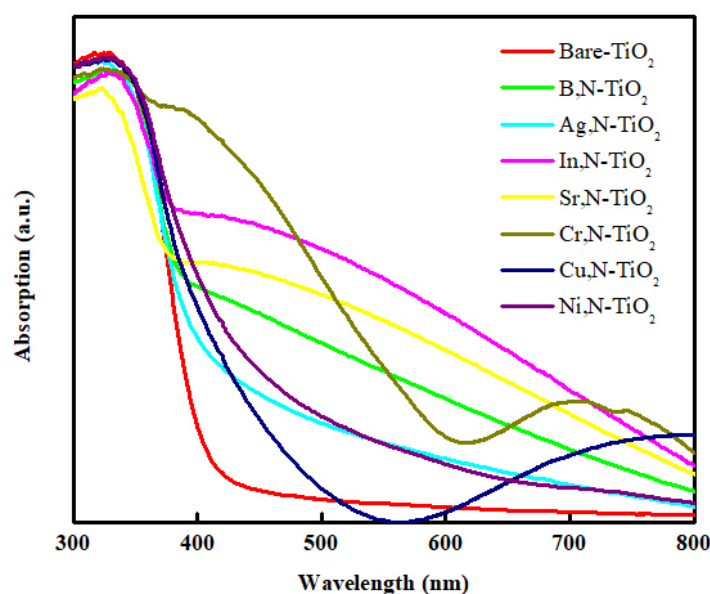


**Fig. 25.** UV-vis diffuse absorbance spectra of metal/nonmetal doped TiO<sub>2</sub>.

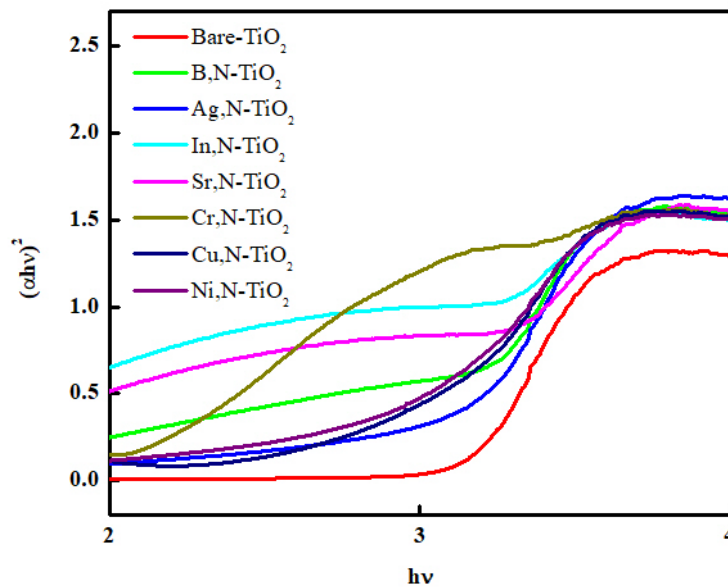


**Fig. 26.** Optical properties of metal/nonmetal doped  $\text{TiO}_2$  based on Tauc plot equation.

The photoluminescence spectra of metal doped  $\text{TiO}_2$  with the excitation wavelength of 270 nm are demonstrated in **Fig. 27**. The PL measurement was examined to investigate the change in the surface state and the efficient of charge trapping, immigration and transferring in semiconductor nanoparticles (Shamaila *et al.*, 2010). As the results, doping of metal/nonmetal on  $\text{TiO}_2$  remarkable decrease on PL intensity in comparison to bare- $\text{TiO}_2$ . This implied that a decrease in the PL intensity could be enhance the effective of charge separation.

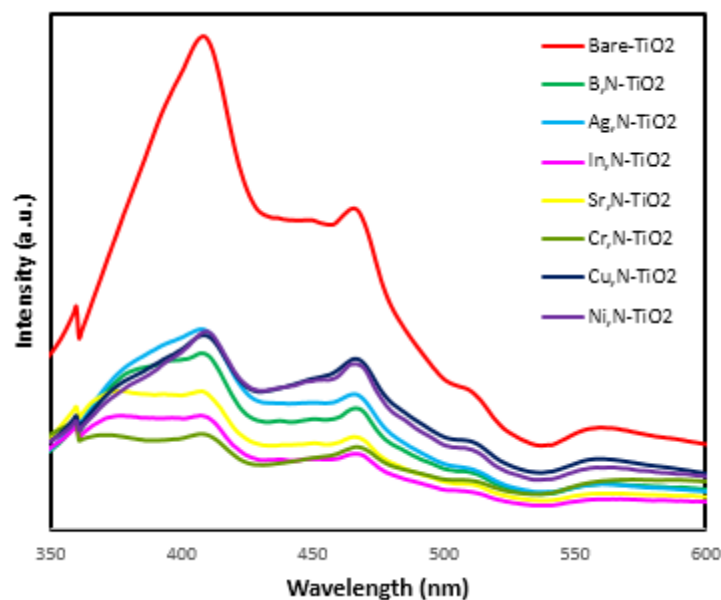


**Fig. 27.** Photoluminescence spectra of metal/nonmetal doped  $\text{TiO}_2$ .

In this part, the synergistic of metal/nonmetal doping on TiO<sub>2</sub> nanoparticles was carried out at 400 °C for 2 h. The phase characteristics of the photocatalysts were studied by XRD and the patterns are shown in **Fig. 28**. It was found that all samples were consisted of anatase form as a unique phase. It was found that the diffraction peak for all photocatalyst samples could be assign to TiO<sub>2</sub> anatase phase. The specific peak of all metal dopant could not be found in the photocatalyst sample. This could be ascribed with well dispersion of dopant on the surface of TiO<sub>2</sub> including small amount of dopant loading (2% mole of Ti) and its small size. The average crystalline sizes of all samples were calculated by well-known Scherrer formula as shown in **Table 8**. The crystalline size of the doped TiO<sub>2</sub> was smaller compared with the bare-TiO<sub>2</sub>. According to the results, the wider FWHM was corresponded to a decrease of crystalline size. This could be due to the slight distortion in the crystalline structure resulted from the dopants (Fu et al., 2016). No change in the 25.4° degrees was observed between the bare and doped TiO<sub>2</sub>.

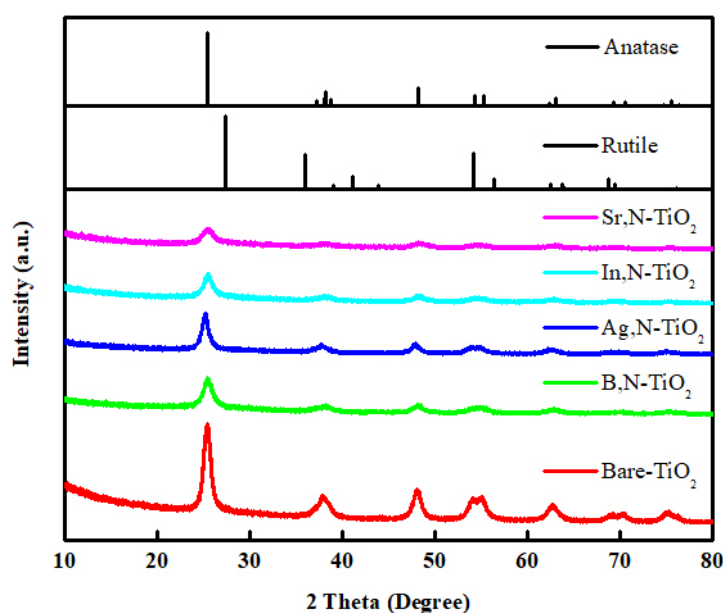


**Fig. 28.** XRD diffraction pattern of bare-TiO<sub>2</sub> and metal doped TiO<sub>2</sub>.

**Table 8.** The crystalline size of metal doped TiO<sub>2</sub>

| Photocatalysts        | Crystal phase (%) |        | Crystallite size (nm) |
|-----------------------|-------------------|--------|-----------------------|
|                       | Anatase           | Rutile |                       |
| Bare-TiO <sub>2</sub> | 100               | -      | 9.59                  |
| B,N-TiO <sub>2</sub>  | 100               | -      | 7.35                  |
| Sr,N-TiO <sub>2</sub> | 100               | -      | 6.03                  |
| In,N-TiO <sub>2</sub> | 100               | -      | 7.45                  |
| Ag,N-TiO <sub>2</sub> | 100               | -      | 7.63                  |

### 1.3.6.2 The performance of synergistic effects metal/nonmetal doped TiO<sub>2</sub> on glucose conversion

The aim of this part is to investigate the synergistic effects of metal/nonmetal doped TiO<sub>2</sub> on the performance of glucose conversion in comparison with the efficiency of single doped TiO<sub>2</sub> (nonmetal or metal) in previous results. The efficiency of single doped TiO<sub>2</sub> on glucose conversion are illustrated in **Fig. 29**. As the results, a nitrogen doped TiO<sub>2</sub> was selected as nonmetal doping with highest performance on glucose conversion (60.3%). Then, various metal (B, Ag, In, Sr, Cr, Cu, Ni) was applied as co-catalyst with nonmetal (nitrogen) to study the synergistic effect on glucose conversion. The performance of synergistic photocatalysts are shown in **Fig. 30**. However, this study showed the conversion results of photocatalyst which gave the performance over 50%. It was found that Sr,N-TiO<sub>2</sub> and In,N-TiO<sub>2</sub> demonstrated a decreasing on glucose conversion compared to its single doping. This indicating no significant effect of synergistic was observed. On the other hand, the presence of B,N-TiO<sub>2</sub> and Ag,N-TiO<sub>2</sub> showed a good synergistic to greatly enhance on glucose conversion which were equivalent to 93.1 and 97.7%, respectively. However, the characteristic of products consists mainly of gluconic acid, arabinose, xylitol, and formic acid for all photocatalysts (**Fig. 31**). Moreover, the time course-change of product profile was almost the same for the reaction using all synergistic photocatalysts.

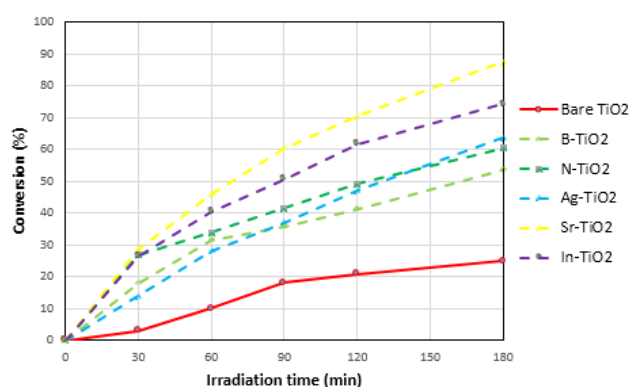


**Fig. 29.** Photocatalytic conversion of glucose under UV irradiation for 180 min in the presence of single doping on TiO<sub>2</sub>.

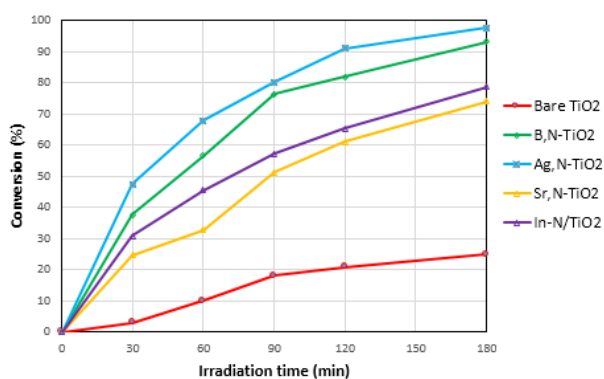


**Fig. 30.** Photocatalytic conversion of glucose under UV irradiation for 180 min in the presence of synergistic metal/nonmetal doping on TiO<sub>2</sub>.

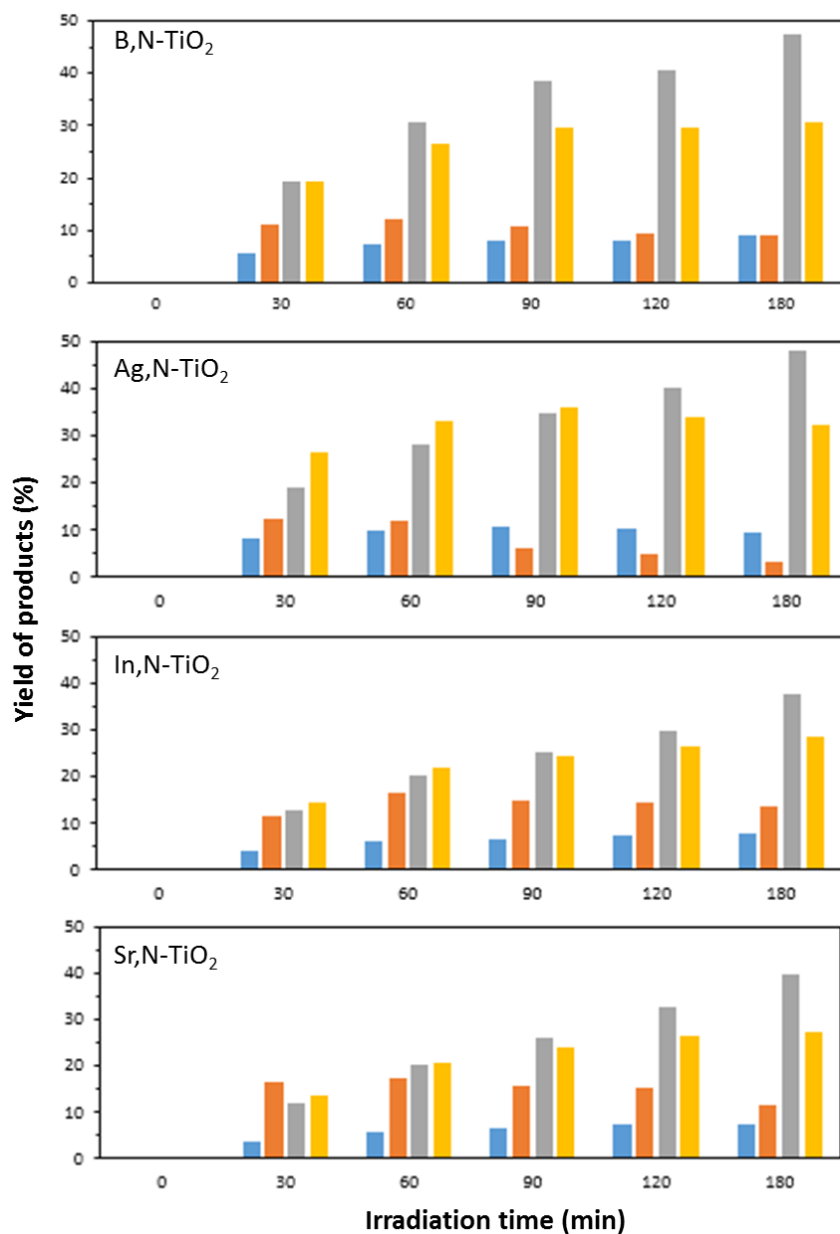


**Fig. 31.** The product profile of glucose conversion under UV irradiation for 180 min in the presence of synergistic metal/nonmetal doping on TiO<sub>2</sub>.

### 1.3.7 Photocatalytic conversion of glucose under visible light

In this study, the modified photocatalyst were performed under 450 W Xenon lamp equipped with sharp cut-off filter  $\lambda > 380$  nm. The commercial of TiO<sub>2</sub> (P25) was used as benchmark (**Fig. 32**). The highest glucose conversion of P25 was observed at 9 h with 62%. The main products were arabinose, formic acid, gluconic and xylitol with the yield of 26.08%, 23.36%, 10.92% and 10.42%, respectively. Further, applied material as graphitic carbon nitride (*g*-C<sub>3</sub>N<sub>4</sub>) is a special characteristic on photocatalytic conversion in term of productivity and selectivity (**Fig. 33**). The *g*-C<sub>3</sub>N<sub>4</sub> could be enhance the conversion of 77% at 12 h. Interestingly, the different main products were gluconic acid and formic acid comparing with benchmark (P25). The yield of gluconic acid, formic acid, arabinose, and xylitol were 35.2,

29.7, 8.9 and 4.4%, respectively. However, others synthesized quantum-compound including ZAIS, AIS, CuO, and  $V_2O_5$  were no substantial effect on the photocatalytic performance (data not shown). The fabricated photocatalyst will be further study on glucose conversion in order to compare the performance with photocatalysts nanoparticles.

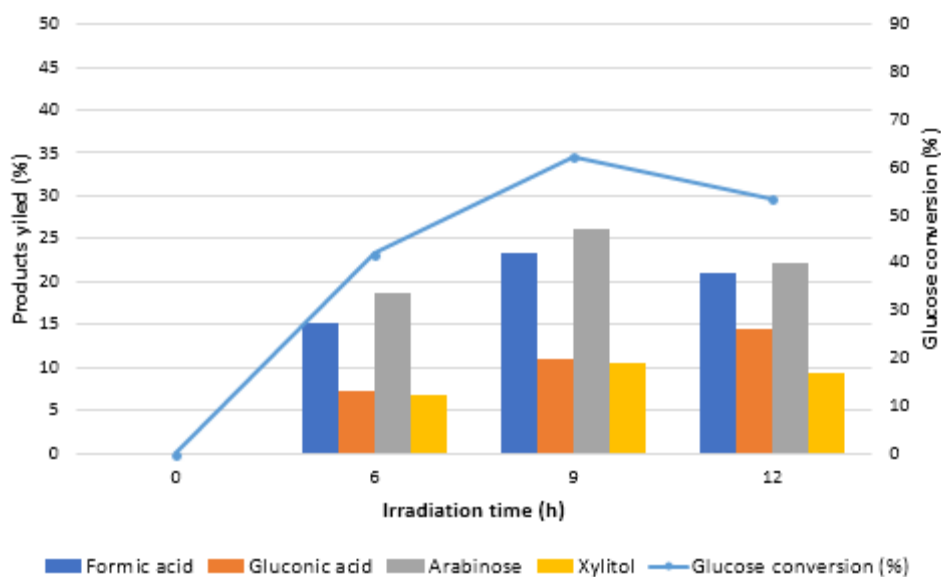


**Fig. 32.** Photocatalytic conversion of glucose under visible light irradiation in the presence of  $TiO_2$  (P25)

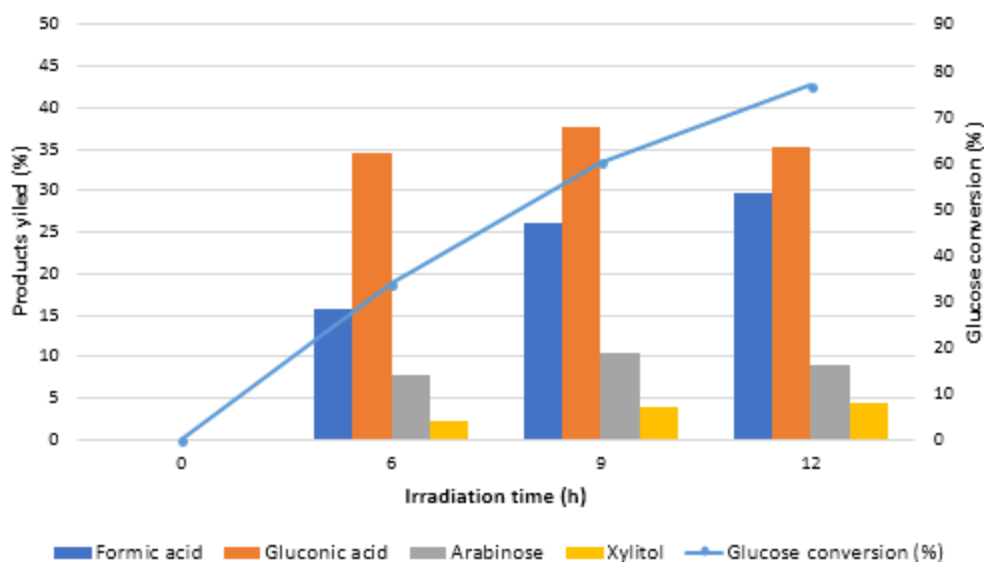


**Fig. 33.** Photocatalytic conversion of glucose under visible light irradiation in the presence of graphitic carbon nitride (g-C<sub>3</sub>N<sub>4</sub>)

### 1.3.8 Photocatalytic conversion of lignin to high value fuels and chemicals

Cellulose is the main component of lignocellulosic, while lignin is the second abundant composition. So lignin has high potential for production of chemicals. There are many techniques to convert lignin to value added chemical, such as pyrolysis, gasification, and depolymerization. These technologies use high temperature and high energy consumption.

So, photocatalytic is an interesting process. The photocatalytic conversion of kraft lignin catalyzed by P25 TiO<sub>2</sub> under UV irradiation present various products. The main products from lignin conversion are 2-methyl-naphthalene, 4-hydroxy-benzaldehyde, and vanillin (Fig. 34 and Table 9).

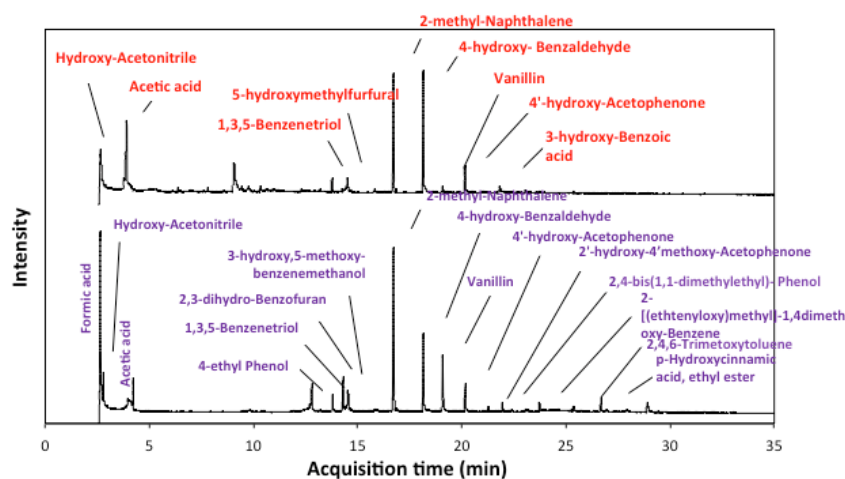


**Fig. 34.** GC-MS spectra of hydrocarbon compounds derived from photocatalytic conversion of kraft lignin catalyzed by P25 TiO<sub>2</sub> under UV irradiation for 2 h and 5 h.

**Table 9.** Products Obtained from Photocatalytic Lignin Conversion of Pristine TiO<sub>2</sub> and TiO<sub>2</sub>/Lignin Composite Photocatalysts (Identified by GC/MS)

| Entry | Compounds identified                        | Structure | Entry | Compounds identified  | Structure |
|-------|---|-----------|-------|---|-----------|
| 1     | Butanedinitrile                             |           | 7     | 4-Hydroxy-3-methoxy acetophenone (Apocynin, Acetovanillone) |           |
| 2     | Benzoic acid                                |           | 8     | 3-Ethoxy-benzoic acid                                       |           |
| 3     | 1,3-Bis(1,1-dimethylethyl) benzene          |           | 9     | Butylated hydroxytoluene (BHT)                              |           |
| 4     | 4-Hydroxybenzaldehyde                       |           | 10    | 3-Hydroxy-4-methoxy benzoic acid (Isovanillic acid)         |           |
| 5     | 3-Ethoxy-4-methoxy phenol                   |           | 11    | 4-Hydroxy-3-methoxy propiophenone (Propiovanillone)         |           |
| 6     | 4-Hydroxy-3-methoxy benzaldehyde (Vanillin) |           | 12    | 4-Hydroxy-3-methoxy cinnamaldehyde (Coniferyl aldehyde)     |           |

### 1.3.9 Combination of photocatalysis to conventional processes for enhancement of biomass pretreatment/hydrolysis

The pretreatment of biomass using photocatalytic process catalyzed P25 TiO<sub>2</sub> under UV irradiation for 24 h was preliminary carried out. The result showed that the amounts of individual sugar, as well as the total sugar yields, were low in the cases of no catalyst and no UV irradiation. TiO<sub>2</sub> photocatalysts could accelerate the separation of biomass compositions. Thus, a lot of products (native) were produced much compared with the photolysis (**Fig. 35**).

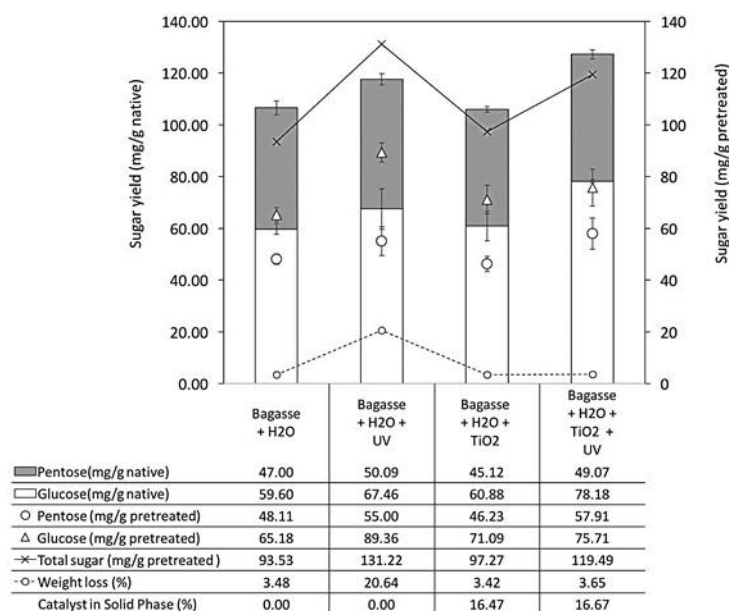


**Fig. 35.** Sugar digestibility yields in photocatalytic pretreatment (solvent = water) compared with blanks (no catalyst and/or no UV irradiation).

### 1.3.10 Further extension of the catalyst design: Preparation of molecularly imprinted TiO<sub>2</sub> hollow nanofibers

According to the procedures confirmed by Roongraung *et al.* in 2016, we prepared TiO<sub>2</sub> hollow nanofibers by electrospinning technique. SEM and TEM images of electrospun TiO<sub>2</sub> hollow nanofibers are indicated in **Fig. 36**.

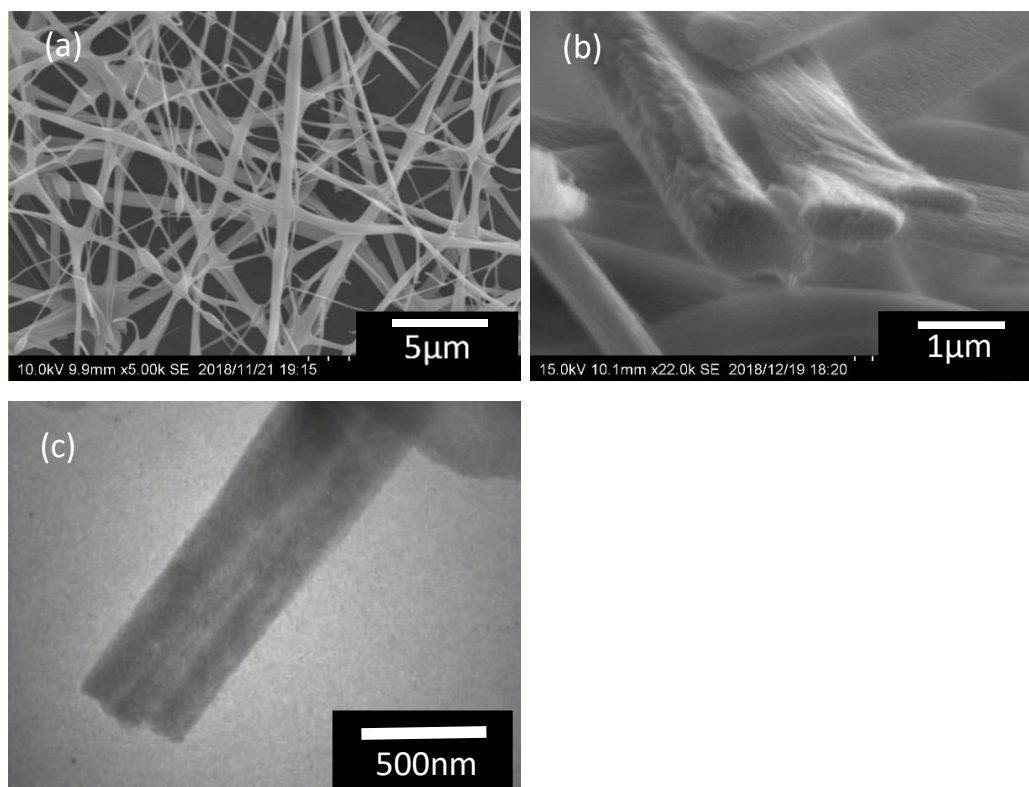


**Fig. 36.** SEM (a, b) and TEM (c) images of electrospun TiO<sub>2</sub> hollow nanofibers.

Photodegradation of methyl orange (MO) with TiO<sub>2</sub> hollow nanofibers under the irradiation of uv-vis light with 500 W Xe lamp was performed. Pseudo first order kinetic constant ( $k$ ) for degradation of MO was estimated from the time course changes of the absorption peak at 508 nm. It was found that TiO<sub>2</sub> hollow nanofibers has the highest catalytic activity ( $k = 2.68 \times 10^{-4} \text{ s}^{-1}$ ) as compared with those of TiO<sub>2</sub> single nanofibers ( $2.03 \times 10^{-4} \text{ s}^{-1}$ ) or TiO<sub>2</sub> (P25) nanoparticles ( $1.50 \times 10^{-4} \text{ s}^{-1}$ ). Further characterization of the crystalline phases, specific surface area, and porosity of those materials in addition to the evaluations of the photocatalytic activity are still underway. Furthermore, methyl red-based molecularly imprinted TiO<sub>2</sub> hollow nanofibers were also prepared as follows: Polymerizable target molecule for imprinting was initially prepared with chlorotitanium (IV) triisopropoxide and methyl red in methanol. Thereafter, polyvinylpyrrolidone, acetylacetone, and titanium (IV) butoxide were mixed with the above solution of the polymerizable target molecule to prepare the precursor solution for shell part of the spinning. While mineral oil was used for core part. Electrospinning was performed with coaxial needles under 15 kV biased conditions. Soaking in n-octane for 6h and washing with 1% NH<sub>3</sub> aqueous solution for 3h followed by the desiccation at 60 °C for 1d and calcination with raising the temperature with 10 °C min<sup>-1</sup> ramping from room temperature to 600°C and hold for 3h at 600 °C in air. Optical images of the obtained fiber mats after soaking in n-octane, washing with 1% NH<sub>3</sub>, and calcination process were shown in **Fig. 37**. Further characterization and the evaluations of the photocatalytic activity are now in progress.

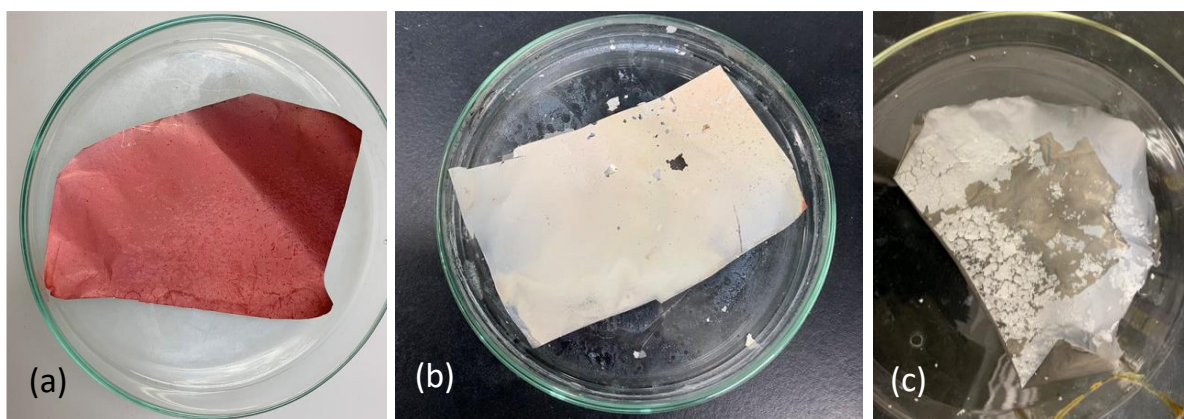


**Fig. 37.** Optical images of the obtained fiber mats after soaking in n-octane (a), washing with 1%  $\text{NH}_3$  (b), and calcination (c).

#### 1.4 Conclusions

The photocatalytic reaction can convert glucose to value added chemical such as gluconic acid, arabinose, xylitol and formic acid. The modification of  $\text{TiO}_2$  by CTAB and zeolite can improve the photocatalytic activity.  $\text{TiO}_2$  can also be used as photocatalyst to convert lignin to value-added chemicals. Some high value chemicals, e.g. 2-methyl-naphthalene, 4-hydroxy-benzaldehyde, and vanillin, were obtained from the lignin as the converted products. Moreover, photocatalysis can be used for pretreatment of biomass. Consequently,  $\text{TiO}_2$  could accelerate the separation of biomass compositions better than photolysis. Furthermore, several extensions of the catalysts design for improvement of the catalysis and the selectivity have been performed though characterization and evaluations of their catalytic activity for conversion of glucose or lignin under the illumination of the light are still underway.

#### 1.5 Project Outputs

##### 1.5.1 Publications Publications (The publications 1-6 did not acknowledge JST. Papers 7-9 had already been cited JST.)

1. Navaporn Kaerkitcha, Surawut Chuangchote, and Takashi Sagawa (2016) "Control of physical properties of carbon nanofibers obtained from coaxial electrospinning of PMMA and PAN with adjustable inner/outer nozzle-ends," *Nanoscale Research Letters*, 11(1), 1-9.
2. Witchaya Arpavate, Surawut Chuangchote, Navadol Laosiripojana, Jatuphorn Wootthikanokkhan, and Takashi Sagawa (2016) "ZnO Nanorod Arrays Fabricated by Hydrothermal Method Using Different Thicknesses of Seed Layers for Applications in Hybrid Photovoltaic Cells," *Sensors and Materials*, 28(5), 403-408.
3. Kamonchanok Roongraun, Navadol Laosiripojana, Surawut Chuangchote (2016) "Development of Photocatalytic Conversion of Glucose to Value-added Chemicals by Supported- $\text{TiO}_2$  Photocatalysts," *Applied Mechanics and Materials*, 839, 39-43.
4. Mathana Wongaree, Siriluk Chiarakorn, Surawut Chuangchote, and Takashi Sagawa (2016) "Photocatalytic Performance of Electrospun CNT/ $\text{TiO}_2$  Nanofibers in a Simulated

- Air Purifier under Visible Light Irradiation," *Environmental Science and Pollution Research*, 23, 21395-21406.
5. Navaporn Kaerkittha, Surawut Chuangchote, Kan Hachiya, and Takashi Sagawa (2017) "Influence of the Viscosity Ratio of Polyacrylonitrile/Poly(methyl methacrylate) Solutions on Core-Shell Fibers Prepared by Coaxial Electrospinning", *Polymer Journal*, 49, 497-502.
  6. Jiraporn Payormhorm, Surawut Chuangchote, Kunlanan Kiatkittipong, Siriluk Chiarakom, and Navadol Laosiripojana (2017) "Xylitol and Gluconic Acid Productions via Photocatalytic-Glucose Conversion Using  $\text{TiO}_2$  Fabricated by Surfactant-Assisted Techniques: Effects of Structural and Textural Properties", *Materials Chemistry and Physics*, 196, 29-36.
  7. Jiraporn Payormhorm, Surawut Chuangchote, and Navadol Laosiripojana (2017) "CTAB-Assisted Sol-microwave Method for Fast Synthesis of Mesoporous  $\text{TiO}_2$  Photocatalysts for Photocatalytic Conversion of Glucose to Value-added Sugars", *Materials Research Bulletin*, 95, 546-555.
  8. Nutsanun Klueb-arb, Surawut Chuangchote, Kamonchanok Roongraung, Navadol Laosiripojana, and Takashi Sagawa (2017) "Fabrication of Several Metal-Doped  $\text{TiO}_2$  Nanoparticles and Their Physical Properties for Photocatalysis in Energy and Environmental Applications", *Journal of Sustainable Energy & Environment*, accepted.
  9. Puangphen Hongdilokkul, Surawut Chuangchote, Navadol Laosiripojana, and Takashi Sagawa (2017) "Conversion of Lignin via Photocatalysis Using Synthesized Ag- $\text{TiO}_2$  Photocatalysts Sintered under Different Atmospheres", *Journal of Sustainable Energy & Environment*, accepted.
  10. Nattida Srisasiwimon, Surawut Chuangchote, Navadol Laosiripojana, and Takashi Sagawa (2018) "TiO<sub>2</sub>/lignin-based carbon composited photocatalysts for enhanced photocatalytic conversion of lignin to high value chemicals", *ACS Sustainable Chemistry & Engineering*, 6, 13968-13976.

### **1.5.2 Conference Proceeding**

1. Navaporn Kaerkittha, Surawut Chuangchote, Takashi Sagawa, Control of the physical properties of carbon nanofibers obtained from coaxial electrospinning of PAN and PMMA with adjustable inner/outer nozzle ends, EMN Hong Kong Meeting, Hong Kong, PRC, 2016/12/10.
2. Navaporn Kaerkittha, Surawut Chuangchote, Takashi Sagawa, Control of the physical properties of carbon nanofibers obtained from coaxial electrospinning of PAN and PMMA with adjustable inner/outer nozzle ends, Ajou – Kyoto University Joint Symposium 2016, Swon, South Korea, 2016/1/28.
3. Navaporn Kaerkittha, Surawut Chuangchote, Kan Hachiya, Takashi Sagawa, "Suitable outer/inner viscosity ratio of polymer solutions for fabrication of core-shell fibers by coaxial electrospinning," The 11th SPSJ International Polymer Conference (IPC2016), Fukuoka, 2016/12/16.
4. Kamonchanok Roongraun, Navadol Laosiripojana, and Surawut Chuangchote, 2015, "Development of Photocatalytic Conversion of Glucose to Value-added Chemicals by

- Supported-TiO<sub>2</sub> Photocatalysts," World Future Alternatives (Naresuan University, Phitsanulok, November 30-December 2), School of Renewable Energy Technology.
5. Jiraporn Payormhorm, Xiaobo Li, Thomas Maschmeyer, Navadol Laosiripojana, and Surawut Chuangchote, 2016 "The Study of Photocatalytic Oxidation of Benzyl Alcohol with g-C<sub>3</sub>N<sub>4</sub> under Visible Light: Effect of pH and Salt," 2016 5th International Conference on Material Science and Engineering Technology (ICMSET 2016) (Tokyo, Japan, October 29-31), University of Tokyo.
  6. Patcha Pattanapibul, Surawut Chuangchote, Navadol Laosiripojana, Verawat Champreda, Jerawut Kaewsanee, 2017 "Enhancement of Enzymatic Hydrolysis and Lignin Removal of Bagasse Using Photocatalytic Pretreatment," The 3<sup>rd</sup> International Conference on Renewable Energy Technologies (ICRET2017) (Thammasat University, Bangkok, Thailand, January 22-24), ICRET Organization.
  7. Surawut Chuangchote, 2017 "Electrospun TiO<sub>2</sub> Nanofibers Composed of Bundle of Aligned Nanofibrils: Fabrication, Structural and Photoluminescent Properties," 11<sup>th</sup> South East Asean Technical University Consortium (Ho Chi Minh City University of Technology (HCMUT), Vietnam, March 13-15), Ho Chi Minh City University of Technology.
  8. Puangphen Hongdilokkul, Surawut Chuangchote, Navadol Laosiripojana, Takashi Sagawa, 2017 "Effects of Sintering Conditions in Ag-TiO<sub>2</sub> Nanoparticles on Photocatalytic Degradation of Lignin," International Conference on Materials Processing Technology 2017 (MAPT 2017) (Ramada Plaza Bangkok Menam Riverside, Bangkok, November 30-December 1), King Mongkut's University of Technology Thonburi, NM\_01.
  9. Nutsanun Klueb-arb, Surawut Chuangchote, Navadol Laosiripojana, Takashi Sagawa 2017 "Modifications of TiO<sub>2</sub> Nanoparticle Catalysts by Dopes with Transition Metals (Ag and Cu) or Alkali Metal (Rb)," International Conference on Materials Processing Technology 2017 (MAPT 2017) (Ramada Plaza Bangkok Menam Riverside, Bangkok, November 30-December 1), King Mongkut's University of Technology Thonburi, NM\_01.
  10. Nattida Srisasiwimon, Surawut Chuangchote, Navadol Laosiripojana, Takashi Sagawa (2018) "Carbon/TiO<sub>2</sub> Composite Photocatalysts and Their Applications for Lignin Conversion under Visible Light Irradiation," 2018 International Conference on Engineering, Technology, and Applied Science-Summer Session (ICETA-Summer 2018) (Sapporo Convention Center, Sapporo, Hokkaido, Japan, August 17-19), Setsunan University, ISSN 2411-9318, pp. 125-132.
  11. Oranoot Sittipunsakda, Surawut Chuangchote, Navadol Laosiripojana, Verawat Champreda, Takashi Sagawa (2018) "Sr-Modified TiO<sub>2</sub> Photocatalyst for Photocatalytic Hydrogen Production from Urine," 2018 International Conference on Engineering, Technology, and Applied Science-Summer Session (ICETA-Summer 2018) (Sapporo Convention Center, Sapporo, Hokkaido, Japan, August 17-19), Setsunan University, ISSN 2411-9318, pp. 118-123.
  12. Kamonchanok Roongraung, Surawut Chuangchote, Navadol Laosiripojana, and Takashi Sagawa (2018) "TiO<sub>2</sub> Hollow Nanofibers Fabricated by Coaxial Electrospinning for Photocatalytic Glucose Conversion to High Value Chemicals," 2018 International Conference on Engineering, Technology, and Applied Science-Summer Session (ICETA-Summer 2018) (Sapporo Convention Center, Sapporo, Hokkaido, Japan, August 17-19), Setsunan University, ISSN 2411-9318, pp. 104-109.

13. Kamonchanok Roongraung, Surawut Chuangchote, and Navadol Laosiripojana (2018) "Development of Green Synthesis of Value-added Chemicals using Photocatalytic Conversion of Glucose with TiO<sub>2</sub>/Supporter," The International Conference on Advanced and Applied Petroleum, Petrochemicals, and Polymers 2018 (ICAPPP 2018) (Chulalongkorn University, Bangkok, Thailand, December 18-20), The Petroleum and Petrochemical College, pp. 58 (#O-ACC-4).

### 1.5.3 Award

1. The Best Presentation Award in The 3rd International Conference on Renewable Energy Technologies (ICRET2017) (Ms. Patcha Pattanapibul).

### 1.5.4 Exchange Researches

**Table 1.** Exchange researches in JASTIP

| Name                          | Exchange Period            | Research Topic  |
|-------------------------------|----------------------------|---|
| Ms. Kamonchanok Roongraung    | 18 Feb 2016 - 19 July 2016 | Nano-scaled Photocatalysts for Energy Applications  |
| Mr. Suriyachai Nopparat       | 28 Sep 2016 - 31 May 2017  | Modification of Visible Light Photocatalytic Activity for Biomass Conversion to Value-added Chemicals           |
| Ms. Nutsanun Klueb-arb        | 14 Nov 2016 - 23 Dec 2016  | A Study of Reaction Pathways in Photocatalytic Conversion of Sugars to High-Value Fuels and Chemicals           |
| Ms. Puangphen Hongdilokkul    | 14 Nov 2016 - 23 Dec 2016  | Photocatalytic Upgrading of Lignin to High Value Products by Nanostructured Catalysts                           |
| Ms. Kanyanee Sanglee          | 6 Feb 2017 - 17 Mar 2017   | Development of Visible-Light Irradiation Responded Metal Oxide for Photocatalytic and Photovoltaic Applications |
| Ms. Nattida Srisasiwimon      | 29 May 2017 - 29 June 2017 | Modification of Photocatalysts for Lignin Conversion  |
| Ms. Oranoot Sittipunsakda     | 29 May 2017 - 29 June 2017 | Development of Metal-doped Photocatalysts for Hydrogen Evolution  |
| Ms. Nattakarn Sakarapunthip   | 09 Oct 2018 - 27 Oct 2018  | Perovskite Materials for Photovoltaic Applications  |
| Ms. Tunnapat Worarutariyachai | 09 Oct 2018 - 27 Oct 2018  | Fabrication of Carbon Fibers from Bio-resource Materials  |
| Mr. Surachet Soontontaweesub  | 18 Nov 2018 - 22 Dec 2018  | Preparation of B,N-containing TiO <sub>2</sub> Hollow Nanoribbons   |

## References

- Awungacha, L. C., Hild, J., Czermak, P., and Herrenbauer, M. (2014). Photocatalytic active coatings for lignin degradation in a continuous packed bed reactor, *International Journal of Photoenergy*, 2014.
- Bahadur, N., Jain, K., Pasricha, R., and Chand, S. (2011), Selective gas sensing response from different loading of Ag in sol-gel mesoporous titania powders, *Sensors and Actuators B: Chemical*, **159**, 1, 112-120.
- Chaudhary, V., Srivastava, A.K., and Kumar, J. (2011), On the Sol-gel Synthesis and Characterization of Titanium Oxide Nanoparticles, *Materials Research Society*, **1352**.
- Cheng, G., Akhtar, M.S., Yang, O.B., and Stadler, F.J. (2013), Structure modification of anatase TiO<sub>2</sub> nanomaterials-based photoanodes for efficient dye-sensitized solar cells, *Electrochimica acta*, **113**, 527-535.
- Colmenares J.C., Magdziarz A., and Bielejewska A. (2011), High-value chemicals obtained from selective photo-oxidation of glucose in the presence of nanostructured titanium photocatalysts, *Bioresource Technology*, **102**, 11254-11257.
- Fan, H. X., Li, H. P., Liu, Z. H., Yang, F., and Li, G. (2015). Production of fine chemicals by integrated photocatalytical degradation of alkali lignin solution in corrugated plate reactor and cyclic extraction technology, *Industrial Crops and Products*, **74**, 497-504.
- Fu, D., Gong, Y., Wu, Y., Liu, J., Zhang, Z., Li, C., and Niu, L., (2016). Photocatalytic enhancement of TiO<sub>2</sub> by B and Zr co-doping and modulation of microstructure. *Applied Surface Science*. **379**, 83–90.
- Gomathisankar, P., Yamamoto, D., Katsumata, H., Suzuki, T., and Kaneco, S. (2013), Photocatalytic hydrogen production with aid of simultaneous metal deposition using titanium dioxide from aqueous glucose solution, *International Journal of Hydrogen Energy*, **38**, 5517-5524.
- Gong, Y., Fu, C., Ting, L., Chenu, J., Zhao, Q., and Li, C., Exploring the effect of boron and tantalum codoping on the enhanced photocatalytic activity of TiO<sub>2</sub>. *Applied Surface Science*. (2015), **351**, 746–752.
- Hwang, K.J., Lee, J.W., Shim, W.G., Jang, H.D., Lee, S.I., and Yoo, S.J. (2012), Adsorption and photocatalysis of nanocrystalline TiO<sub>2</sub> particles prepared by sol-gel method for methylene blue degradation, *Advance Powder Technology*. **23**, 414-418.
- Jaimy, K. B., Vidya, K., Saraswathy, H. U. N., Hebalkar, N. Y., and Warriar, K. G. K. (2014), Dopant-free anatase titanium dioxide as visible-light catalyst: Facile sol-gel microwave approach, *Journal of Environmental Chemical Engineering*.

Kadam, A.; Dhabbe, R.; Shin, D. S.; Garadkar, K.; Park, J. (2017), Sunlight Driven High Photocatalytic Activity of Sn Doped N-TiO<sub>2</sub> nanoparticles Synthesized by a Microwave Assisted Method. *Ceram. Int.* **43**, 5164–5172.

Kameyama, T., et al., (2015), Controlling the Electronic Energy Structure of ZnS–AgInS<sub>2</sub> Solid Solution Nanocrystals for Photoluminescence and Photocatalytic Hydrogen Evolution. *J. Phys. Chem. C.* **119**, 24740–24749.

Li, H., Lei, Z., Liu, C., Zhang, Z., and Lu, B. (2015). Photocatalytic degradation of lignin on synthesized Ag–AgCl/ZnO nanorods under solar light and preliminary trials for methane fermentation, *Bioresource Technology.* **175**, 494-501.

Liu, J., Han, R., Zhao, Y., Wang, H., Lu, W., Yu, T., and Zhang, Y., (2011), Enhanced Photoactivity of V-N Codoped TiO<sub>2</sub> Derived from a Two-Step Hydrothermal Procedure for the Degradation of PCP-Na under Visible Light Irradiation. *J. Phys. Chem. C.* **115**, 4507–4515.

Mozia S., Heciak A., and Morawski A.W. (2011), Photocatalytic acetic acid decomposition leading to the production of hydrocarbons and hydrogen on Fe-modified TiO<sub>2</sub>, *Catalysis Today*, **161**, 189-195.

Murugan, K., Subasri, R., Rao, T.N., Gandhi, A.S., and Murty, B.S. (2013), Synthesis, characterization and demonstration of self-cleaning TiO<sub>2</sub> coatings on glass and glazed ceramic tiles, *Progress in Organic Coatings*, **76**, 1756-1760.

Mutuma, B. K., Shao, G. N., Kim, W. D., and Kim, H. T. (2015), Sol-gel synthesis of mesoporous anatase-brookite and anatase-brookite-rutile TiO<sub>2</sub> nanoparticles and their photocatalytic properties, *Journal of colloid and interface science*, **442**, 1-7.

Nasralla, N., Yeganeh, M., Astuti, Y., Piticharoenphuna, S., Shahtahmasebi, N., Kompany, A., Karimipour, M., Mendis, B.G., Poolton, N.R.J., Siller, L., (2013), "Structural and spectroscopic study of Fe-doped TiO<sub>2</sub> nanoparticles prepared by sol–gel method", *Scientia Iranica.* **20**, 1018-1022.

Oh, J. K., Lee, J. K., Kim, S. J., and Park, K. W. (2009), Synthesis of phase- and shape-controlled TiO<sub>2</sub> nanoparticles via hydrothermal process, *Journal of Industrial and Engineering Chemistry*, **15**, 2, pp. 270-274.

Ong, W.J., Tan, L.L., Ng, Y.H., Yong, S.T., and Chai, S.P., (2016), Graphitic carbon nitride (g-C<sub>3</sub>N<sub>4</sub>)-based photocatalysts for artificial photosynthesis and environmental remediation: Are we step closer to achieving sustainability?. *Chem. Rev.* **116**, 7159-7329.

Payormporn, J., Chuangchote, S., Kiatkittipong, K., Chiarakorn, S., and Laosiripojana, N., (2017), Xylitol and gluconic acid productions via photocatalytic-glucose conversion using TiO<sub>2</sub> fabricated by surfactant-assisted techniques: Effects of structural and textural properties. *Materials Chemistry and Physics.* **196**, 29-36.

- Prado, R., Erdocia, X., and Labidi, J. (2013). Effect of the photocatalytic activity of TiO<sub>2</sub> on lignin depolymerization, *Chemosphere*, **91**, 1355-1361.
- Park, J.Y., Yun, J.J., Hwang, C.H., and Lee, I.H. (2010), Influence of silver doping on the phase transformation and crystallite growth of electrospun TiO<sub>2</sub> nanofibers, *Materials Letters*. **64**, 2692-2695.
- Pelaez, M., et al., (2012), A review on the visible light active titanium dioxide photocatalysts for environmental applications. *Applied Catalysis B: Environmental*. **125**, 331-349.
- Shamaila, S., Sajjad, A.K.L., Chen, F., Zhang, J., (2010), Study on highly visible light active Bi<sub>2</sub>O<sub>3</sub> loaded ordered mesoporous titania. *Appl. Catal. B: Environ.* **94**, 272–280.
- Shen, X., Zhang, J., and Tian, B. (2011), Microemulsion-mediated solvothermal synthesis and photocatalytic properties of crystalline titania with controllable phases of anatase and rutile, *Journal of hazardous materials*, **192**, 651-657.
- Shi, J., & Wang, X. (2011). Growth of rutile titanium dioxide nanowires by pulsed chemical vapor deposition. *Crystal Growth & Design*, **11**, 949-954.
- Shojaie, A.F., and Loghmani, M.H. (2010), La<sup>3+</sup> and Zr<sup>4+</sup> co-doped anatase nano TiO<sub>2</sub> by sol-microwave, *Chemical Engineering Journal*, **157**, 263-269.
- Song, S., Yang, T., Li, Y., Pang, Z., Lin, L., Lv, M., and Han, S. (2009), Structural, electrical and optical properties of ITO films with a thin TiO<sub>2</sub> seed layer prepared by RF magnetron sputtering, *Vacuum*, **83**, 1091-1094.
- Srisasiwimon, N., Chuangchote, S., Laosiripojana, N., Sagawa, T., (2018), TiO<sub>2</sub>/Lignin-Based Carbon composited photocatalysts for enhanced photocatalytic conversion of lignin to high value chemicals. *ACS Sustainable Chem. Eng.* **6**, 13968-13976.
- Su, C., Hong, B.Y., and Tseng, C.M. (2004), Sol-gel preparation and photocatalysis of titanium dioxide, *Catalysis today*, **96**, 119-126.
- Suwarnkar, M. B., Dhabbe, R. S., Kadam, A. N., & Garadkar, K. M. (2014). Enhanced photocatalytic activity of Ag doped TiO<sub>2</sub> nanoparticles synthesized by a microwave assisted method. *Ceramics International*, **40**, 5489-5496.
- Tahir, A.A., Peiris, T.A., and Wijayantha, K.G. (2012), Enhancement of Photoelectrochemical Performance of AACVD-produced TiO<sub>2</sub> Electrodes by Microwave Irradiation while Preserving the Nanostructure, *Chemical Vapor Deposition*, **18**, 107-111.
- Tanaka, Y., Sakai, H., Tsuke, T., Uesugi, Y., Sakai, Y., and Nakamura, K. (2011), Influence of coil current modulation on TiO<sub>2</sub> nanoparticle synthesis using pulse-modulated induction thermal plasmas, *Thin Solid Films*, **519**, 7100-7105.

Tobaldi, D. M., Škapin, A. S., Pullar, R. C., Seabra, M. P., & Labrincha, J. A. (2013). Titanium dioxide modified with transition metals and rare earth elements: phase composition, optical properties, and photocatalytic activity. *Ceramics International*. **39**, 2619-2629.

Torimoto, T., Adachi, T., Okazaki, K., Sakuraoka, M., Shibayama, T., Ohtani, B., Kudo, A., and Kuwabata, S., (2007), Facile Synthesis of ZnS-AgInS<sub>2</sub> Solid Solution Nanoparticles for a Color-Adjustable Luminophore. *J. AM. CHEM. SOC.* **129**, 12388-12389.

Vijayalakshmi, R., and Rajendran, V. (2012), Synthesis and characterization of nano-TiO<sub>2</sub> via different methods, *Arch App Sci Res*, **4**, 2, 1183-1190.

Xu, G., Zeng, S., Zhang, B., Swihart, M.T., Yong, K.T., and Prasad, P.N., (2016), New Generation Cadmium-Free Quantum Dots for Biophotonics and Nanomedicine. *Chem Rev.* **116**, 12234-12327.

Zhang, Y., Zheng, H., Liu, G., and Battaglia, V. (2009), Synthesis and electrochemical studies of a layered spheric TiO<sub>2</sub> through low temperature solvothermal method, *Electrochimica Acta*, **54**, 16, 4079-4083.

Zhao, Y., Li, C., Liu, X., Gu, F., Jiang, H., Shao, W., and He, Y. (2007), Synthesis and optical properties of TiO<sub>2</sub> nanoparticles, *Materials Letters*, **61**, 1, 79-83.

# **Development of Carbons from Biomass for Energy Storage Applications**

## 2. Development of Carbons from Biomass for Energy Storage Applications

Research team:

Dr. Sumittra Charojrochkul, MTEC, NSTDA (Project leader, Thai side)

Prof. Dr. Takeshi Abe, Kyoto University (Project leader, Japan side)

Dr. Yatika Somrang, MTEC, NSTDA

Dr. Yuto Miyahara, Kyoto University

Dr. Vituruch Goodwin MTEC, NSTDA

Mr. Thanathon Sesuk, MTEC, NSTDA

### 2.1 Introduction

There have been many researches currently investigating the potential of using biomass as a source to produce activated carbons from carbonisation or hydrothermal carbonization. Pyrolysis or carbonisation is a conventional process; hence, it is not a complicate technology. Only some modification/configuration to the traditional method, i.e. introduction of porogen for pore activation, can significantly improve the properties of the carbon. Hence, due to its simplicity but high impact to the properties of carbon products, this technology is chosen in this work.

The knowledge of how each biomass constituent affects the properties of activated carbon materials in aspect of physical and electrochemical characteristic is crucial to enhance the production of high-quality carbon materials for energy storage application. Thailand is an agricultural-based country with abundant resources of biomass. However, the majority of biomass in Thailand, especially agricultural leftover, has not yet been exploited extensively. Currently, the use of biomass as fuel for energy production has been widely studied and utilised. Introducing the transformation of biomass- to valuable materials benefits the promotion of bio-based economy. Biomass which mainly contains cellulose, hemicellulose and lignin can be converted into chemicals or valuable products. In fact, biomass is a major carbon source which can potentially be used in energy storage devices.

This project investigate various 'challenging' biomass, i.e. palm empty fruit bunch (PEFB), durian peel and etc. The aims to understand the biomass constituents relation to the physical and electrochemical properties of the activated carbons and production of activated carbon from palm empty fruit bunch using carbonisation/hydrothermal and/or chemical activation. This work is jointly collaborated between MTEC/NSTDA, responsible for producing activated carbon from biomass and performing physical characterisation of the obtained carbon, and Kyoto University, in charge of conducting electrochemical characterisation of the carbons for supercapacitor applications.

## 2.2 Research Progress

### 2.2.1 Experimental

#### 2.2.1.1 Activated Carbon Preparation and Characterisation

Activated carbon samples were prepared from various biomass, including palm empty fruit bunch (EFB), palm shell (PS), and sugarcane bagasse (SB). All biomass was first washed with water and dried to eliminate soil particles and other impurities. Afterwards, it was ground, milled and sieved to 75-150  $\mu\text{m}$ . All biomass was thermally carbonised at 500 $^{\circ}\text{C}$  for 2 hours to obtain char. Followed by chemical activation with KOH at 1:1 and 2:1 KOH : Char weight ratio (Effect of KOH : Char ratio on physical properties) under  $\text{CO}_2$  atmosphere at 700-900  $^{\circ}\text{C}$  (Effect of activation temperature on physical properties). The activated carbon samples were characterised for their microstructure by SEM and TEM techniques. Specific surface area (BET) and porosity were analysed using  $\text{N}_2$  adsorption at -196  $^{\circ}\text{C}$ . XRD patterns were obtained for crystalline and amorphous phase identification. More activated carbon samples were prepared from two different sections of palm empty fruit bunch (EFB) which are the EFB-core (EFB-C) and EFB-stem (EFB-S). Each section has different C H N ratio and proximate analysis results which may affect the physical properties of the activated carbon. Thus, these EFB-C and EFB-S are undergoing a further physical and electrochemical properties investigation. Eucalyptus wood chip (WC) and durian peel (DUR) were additionally included as these two biomass contain different C H N ratio compared to EFB. Eucalyptus wood chip contains high amount of cellulose. Durian peel has high amount of nitrogen and sulfur which may be beneficial for activation process. These additional biomass samples were characterised for elemental analysis i.e., C, H, N, O and S content and the activated carbon samples microstructure were disclosed by SEM and TEM techniques. Characterisation of crystalline and amorphous phase by XRD and specific surface area (BET) and porosity analysis were performed. The effect of preparation conditions including KOH: Char ratio at 1:1 and 2:1 by weight and activation temperature at 700C-900 $^{\circ}\text{C}$  are investigated.

#### 2.2.1.2 Carbon Electrode Preparation and Electrochemical Performance Evaluation

Activated carbon samples from thermal carbonisation and chemical activation process of biomass were made into an electrode sheet of up to 1 mm thickness and 5mm x 5mm square for electrochemical performance evaluation. A three-electrode cell system was employed to investigate galvanostatic charge-discharge and cyclic voltammetry. The prepared electrode was enveloped in a platinum holder which functions as the working electrode. The counter electrode was made from platinum mesh and the reference electrode is Ag/AgCl. The electrolyte was 1 M  $\text{H}_2\text{SO}_4$  saturated with Argon by purging. Cyclic voltammetry test was performed with the scan rate from 1 to 20  $\text{mV s}^{-1}$  and galvanostatic charge-discharge with the current density from 0.1 to 2  $\text{A g}^{-1}$ . The value of specific capacitance was calculated from the galvanostatic chargedischarge.

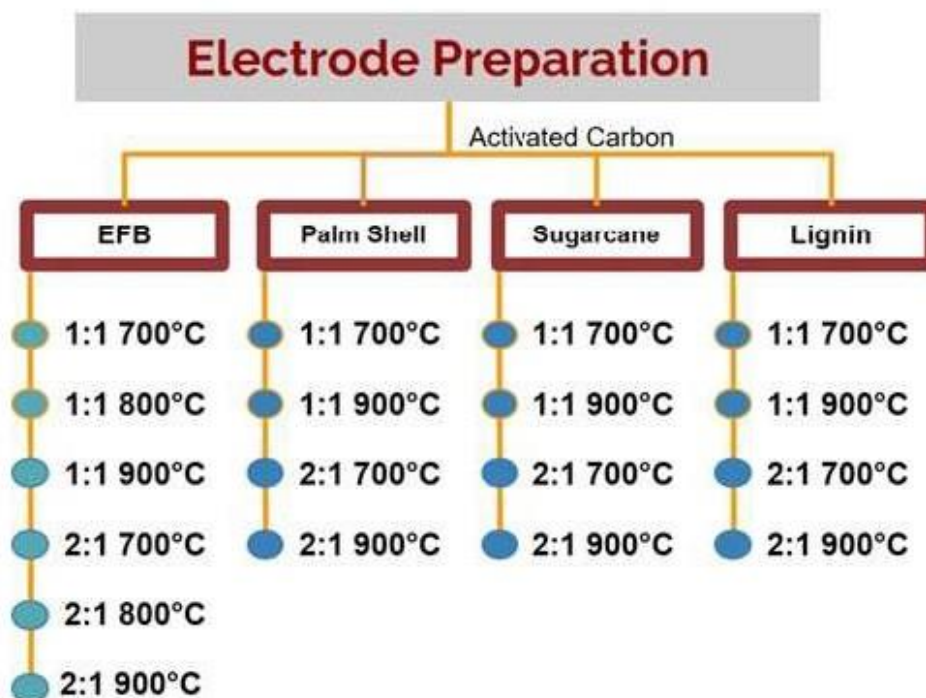


Figure 1 List of biomass types and activation conditions applied that had been tested for electrochemical performance

## 2.2.2 Results and Discussion

### 2.2.2.1 Biomass Characterisation

The proximate and ultimate analysis results of the biomass (dry basis) are presented in Table 1. Table 2 and 3 show the yield by weight of various biomass char obtained by carbonisation at 500°C under N<sub>2</sub> atmosphere and the yield by weight of activated carbon activated at 700 and 900°C, respectively. Palm shell contains highest fixed carbon content at 21.2 % but all biomass has similar fixed carbon from 15.3-21.2%. Durian peel and EFB contain high amount of nitrogen at 1.2 and 1.4%, respectively. From table 2, lignin (chemical grade) gave the highest char yield. The activated carbon yield reflects from fixed carbon amount of biomass and affected by temperature.

Table 1 Proximate and Ultimate analysis results of biomass

| Biomass                      | Proximate analysis (%db) |              |     | Ultimate analysis (%db) |     |     |      |
|------------------------------|--------------------------|--------------|-----|-------------------------|-----|-----|------|
|                              | Volatiles                | Fixed Carbon | Ash | C                       | H   | N   | O    |
| Palm empty fruit bunch (EFB) | 77.3                     | 17.0         | 5.7 | 46.2                    | 5.7 | 1.4 | 40.9 |
| Sugarcane bagasse (SB)       | 75.0                     | 16.2         | 8.8 | 47.6                    | 5.8 | 0.6 | 37.4 |
| Palm shell (PS)              | 77.0                     | 21.2         | 1.8 | 54.0                    | 5.2 | 0.6 | 38.4 |
| Eucalyptus wood chip (WC)    | 82.7                     | 16.8         | 0.5 | 47.7                    | 6.8 | 0.1 | 44.9 |
| Durian peel (DUR)            | 77.5                     | 18.2         | 4.3 | 44.3                    | 5.9 | 1.2 | 44.3 |
| EFB-C                        | 80.3                     | 15.3         | 4.4 | 41.8                    | 6.1 | 0.7 | 47.0 |
| EFB-S                        | 82.7                     | 15.4         | 1.9 | 46.5                    | 6.2 | 0.9 | 44.5 |

Table 2 Yield of biomass char obtained by carbonization at 500 °C

| Biomass                             | Yield (wt%) |
|-------------------------------------|-------------|
| Palm empty fruit bunch (EFB)        | 27.28       |
| Sugarcane bagasse (SB)              | 26.49       |
| Palm shell (PS)                     | 32.13       |
| Lignin (LN)                         | 58.59       |
| Cellulose (CL)                      | 23.99       |
| Eucalyptus wood chip (WC)           | 28.62       |
| Durian (DUR)                        | 31.54       |
| Palm empty fruit bunch (EFB-S)      | 31.22       |
| Palm empty fruit bunch-Core (EFB-C) | 25.74       |

Table 3 Yield of Activated Carbon obtained by various biomass at 700°C and 900°C

| Biomass                | Sample code | Activated Temp.(°C) | Yield (%) |
|------------------------|-------------|---------------------|-----------|
| Palm empty fruit bunch | 11700-EFB   | 700                 | 13.24     |
|                        | 21700-EFB   |                     | 13.06     |
|                        | 11800-EFB   | 800                 | 13.26     |
|                        | 21800-EFB   |                     | 10.69     |
|                        | 11900-EFB   | 900                 | 10.26     |
|                        | 21900-EFB   |                     | 9.44      |
| Palm shell             | 11700-PS    | 700                 | 17.34     |
|                        | 21700-PS    |                     | 17.67     |
|                        | 11900-PS    | 900                 | 12.15     |
|                        | 21900-PS    |                     | 12.73     |
| Sugarcane bagasse      | 11700-SB    | 700                 | 10.69     |
|                        | 21700-SB    |                     | 12.03     |
|                        | 11900-SB    | 900                 | 7.77      |
|                        | 21900-SB    |                     | 9.34      |
| Eucalyptus wood chip   | 11700-WC    | 700                 | 16.20     |
|                        | 21700-WC    |                     | 15.50     |
|                        | 11900-WC    | 900                 | 9.84      |
|                        | 21900-WC    |                     | 9.86      |
| Durian                 | 11700-DUR   | 700                 | 10.13     |
|                        | 21700-DUR   |                     | 12.83     |
|                        | 11900-DUR   | 900                 | 8.83      |
|                        | 21900-DUR   |                     | 9.75      |
| EFB-S                  | 11700-EFB-S | 700                 | n/a       |
|                        | 21700-EFB-S |                     | 10.02     |
|                        | 11900-EFB-S | 900                 | 12.93     |
|                        | 21900-EFB-S |                     | 8.95      |

#### 2.2.2.2 Activated Carbon Characterisation

The surface area and pore volume of the activated carbons are summarized in Table 4. All activated carbon samples showed that micropores dominated the pore structure, as indicated by the large surface area as well as percentage of micropore volume ( $V_{\text{micro}}$ ). For EFB, as the activation temperature is increased, the surface area increases. With increasing KOH: Char ratio, the surface area also increases. Activated carbon prepared at activation temperatures of 700-900°C showed the mesopore volume less than 50%. This may indicate both a widening of pores at high temperature and generation of new pores by activating agent. At some condition, the highest surface area sample does not have the largest total pore volume, this indicates that the effect of pore widening could be compensated by the

increase of surface area by a generation of more pores. The average pore diameter were nearly the same for all samples, approximately 4-6 Å. The size of the solvated HSO<sub>4</sub><sup>-</sup> ion size is approximately 3-4 Å, therefore the pore size of activated carbon is large enough to accommodate H<sub>2</sub>SO<sub>4</sub> electrolyte ions.

Table 4 Surface area, total pore volume ( $V_{tot}$ ), micro- ( $V_{micro}$ ) and mesopore ( $V_{meso}$ ) volume and percentage of micro- and mesopore volume in biomass activated carbon at 700-900°C

| Sample code | $S_{BET}$<br>(m <sup>2</sup> /g) | $V_{tot}^*$<br>(cm <sup>3</sup> /g) | $V_{micro}$ (t-plot) |       | $V_{meso}$         |       | Pore width<br>(Å) |
|-------------|----------------------------------|-------------------------------------|----------------------|-------|--------------------|-------|-------------------|
|             |                                  |                                     | cm <sup>3</sup> /g   | %     | cm <sup>3</sup> /g | %     |                   |
| 21600-EFB   | 597.09                           | 0.37                                | 0.21                 | 56.76 | 0.16               | 43.24 | 4.22              |
| 11700-EFB   | 1103.35                          | 0.43                                | 0.40                 | 93.02 | 0.03               | 6.98  | 6.01              |
| 21700-EFB   | 1203.80                          | 0.47                                | 0.46                 | 97.87 | 0.01               | 2.13  | 4.17              |
| 11800-EFB   | 1378.07                          | 0.58                                | 0.50                 | 86.20 | 0.08               | 13.79 | 4.34              |
| 21800-EFB   | 1515.43                          | 0.96                                | 0.47                 | 48.96 | 0.49               | 51.04 | 4.73              |
| 11900-EFB   | 1545.13                          | 0.65                                | 0.58                 | 89.23 | 0.07               | 10.76 | 4.35              |
| 21900-EFB   | 1571.03                          | 0.83                                | 0.53                 | 63.86 | 0.30               | 36.14 | 5.22              |
| 11700-WC    | 1076.28                          | 0.41                                | 0.40                 | 97.56 | 0.01               | 2.43  | 4.33              |
| 21700-WC    | 1432.08                          | 0.57                                | 0.53                 | 92.98 | 0.04               | 7.54  | 4.21              |
| 11900-WC    | 1691.02                          | 0.74                                | 0.62                 | 83.78 | 0.10               | 16.12 | 5.94              |
| 21900-WC    | 1702.06                          | 0.77                                | 0.62                 | 80.15 | 0.15               | 19.48 | 4.22              |
| 11700-LN    | 1144.04                          | 0.47                                | 0.43                 | 91.48 | 0.04               | 8.51  | 5.66              |
| 21700-LN    | 1657.00                          | 0.75                                | 0.59                 | 78.66 | 0.16               | 21.33 | 5.46              |
| 11900-LN    | 1451.91                          | 0.59                                | 0.55                 | 93.22 | 0.04               | 6.77  | 4.27              |

| Sample code | $S_{BET}$<br>( $m^2/g$ ) | $V_{tot}^*$<br>( $cm^3/g$ ) | $V_{micro}$ (t-plot) |       | $V_{meso}$ |       | Pore width<br>( $\text{\AA}$ ) |
|-------------|--------------------------|-----------------------------|----------------------|-------|------------|-------|--------------------------------|
|             |                          |                             | $cm^3/g$             | %     | $cm^3/g$   | %     |                                |
| 21900-LN    | 1650.51                  | 0.79                        | 0.57                 | 72.15 | 0.22       | 27.84 | 4.26                           |
| 11700-PS    | 1005.36                  | 0.40                        | 0.38                 | 95.00 | 0.02       | 5.00  | 4.94                           |
| 21700-PS    | 1540.34                  | 0.61                        | 0.59                 | 96.72 | 0.02       | 3.27  | 4.26                           |
| 11900-PS    | 1158.63                  | 0.45                        | 0.43                 | 95.55 | 0.02       | 4.44  | 5.94                           |
| 21900-PS    | 1470.07                  | 0.59                        | 0.55                 | 93.22 | 0.04       | 6.77  | 4.26                           |
| 11700-SB    | 1217.73                  | 0.47                        | 0.47                 | 100   | -          | -     | 4.46                           |
| 21700-SB    | 1850.69                  | 0.81                        | 0.68                 | 78.16 | 0.13       | 16.04 | 5.73                           |
| 11900-SB    | 1243.83                  | 0.55                        | 0.46                 | 83.63 | 0.09       | 16.36 | 4.06                           |
| 21900-SB    | 1542.29                  | 0.74                        | 0.54                 | 72.97 | 0.20       | 27.02 | 5.35                           |
| Char-EFB    | 5.77                     | 0.0023                      | -                    | n/a   | 0.0023     | 100   | 5.33                           |
| Char-LN     | 3.34                     | 0.0059                      | 0.0024               | 40.67 | 0.0035     | 59.33 | 7.14                           |
| Char-PS     | 7.74                     | 0.0061                      | 0.0099               | -     | -          | -     | 5.65                           |
| Char-SB     | 192.14                   | 0.058                       | 0.085                | -     | -          | -     | 5.65                           |

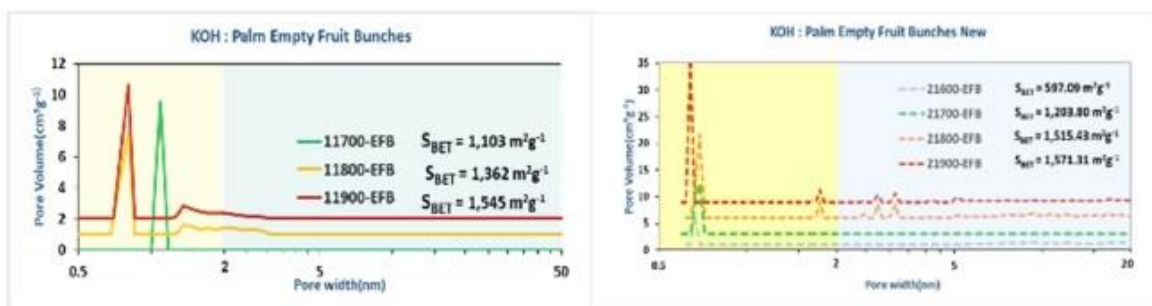


Figure 2 Pore volume vs. Pore width of KOH: Char EFB 1:1(left) and 2:1(right)

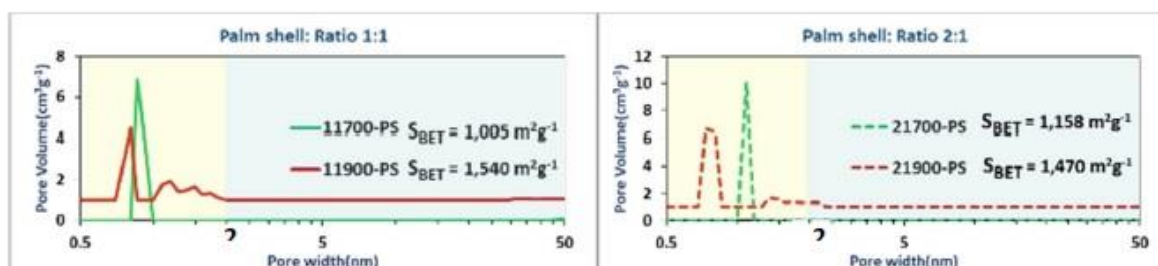


Figure 3 Pore volume vs. Pore width of KOH: Char PS 1:1(left) and 2:1(right)

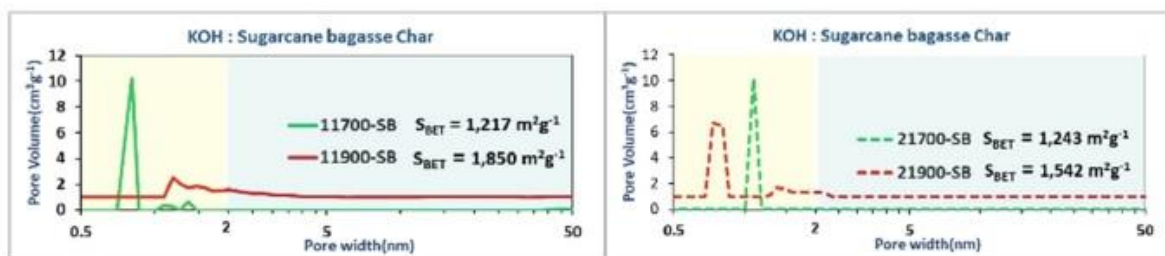


Figure 4 Pore volume vs. Pore width of KOH: Char SB 1:1(left) and 2:1(right)

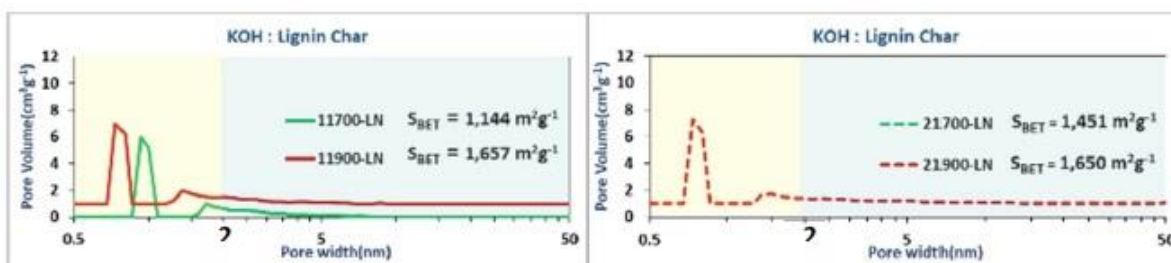


Figure 5 Pore volume vs. Pore width of KOH: Char LN 1:1(left) and 2:1(right)

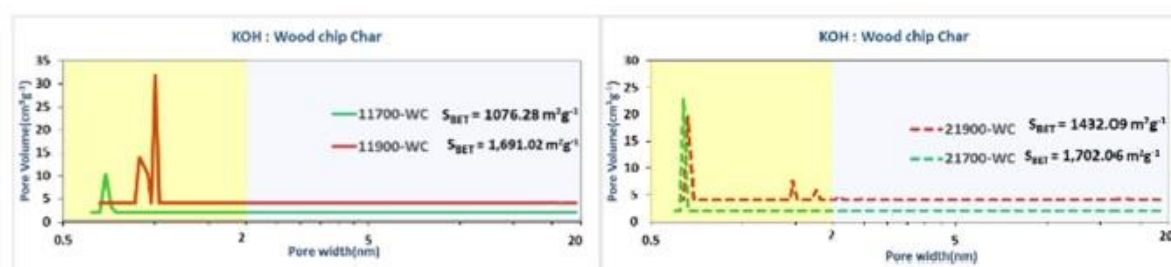


Figure 6 Pore volume vs. Pore width of KOH: Char WC 1:1(left) and 2:1(right)

From Figures 2-6, Plots of Pore volume vs. Pore width showed that activated carbon produced using KOH: Char ratio equal to 1 contained mainly microspore and slightly developed mesopore. At 900 °C activation temperature microspore volume decreased compared to at 700 °C. While at KOH: Char ratio equal to 2, a development of mesopore is increased thus slightly decreased in microspore volume for activation temperature at 900 °C.

X-ray diffraction patterns of activated carbon samples are shown in Figures 7. The results for all samples had broad peaks at  $2\theta \approx 24^\circ$  and  $44^\circ$  indicating amorphous carbon structure. No impurity phases were observed.

In Figure 7 (a), X-ray diffraction results from activated carbon samples from EFB (21900-EFB) had a small peak at  $26^\circ$ . The peak corresponding to a short range order (graphite-like) structure which may be formed as indicated by the peaks at  $2\theta \approx 26.5^\circ$  and  $44.5^\circ$  (JCPDS no. 75-1621) assigned to the (002) and (100) planes, respectively. The formation of graphite-like structure may have been facilitated by the combination of high temperature and high KOH content. It should be noted that the peak is broad compared to that observed in pure graphite, implying the sample consisted of majority amorphous carbon structure albeit with higher graphitic content than other activated carbon samples.

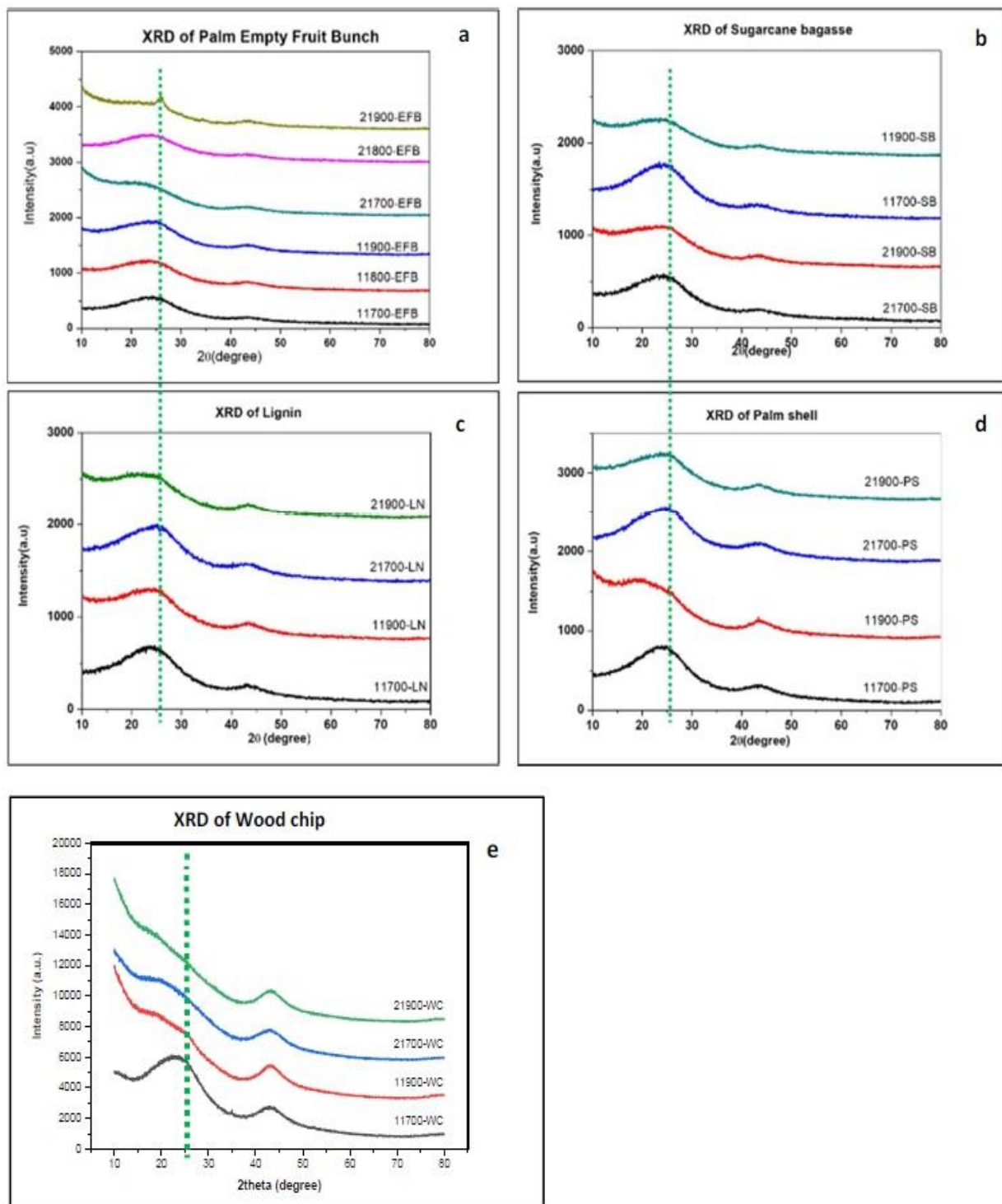
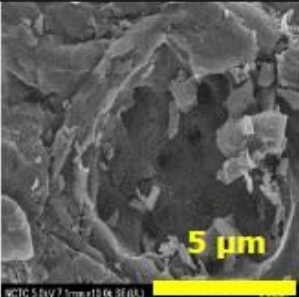
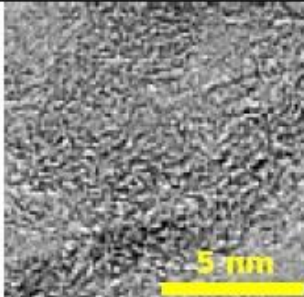
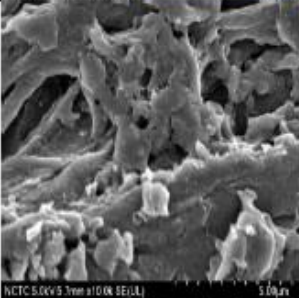
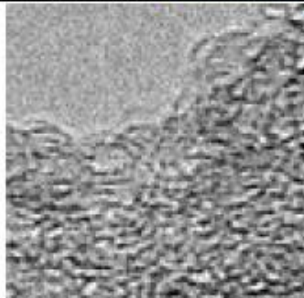
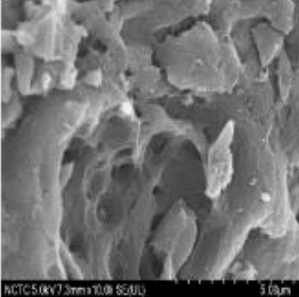
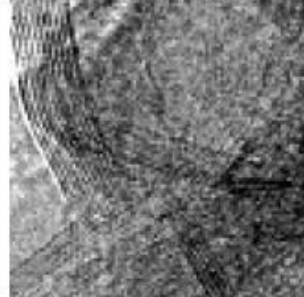
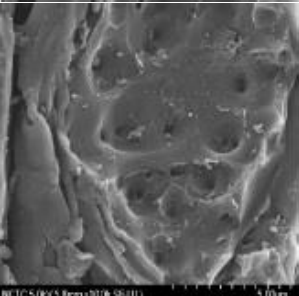
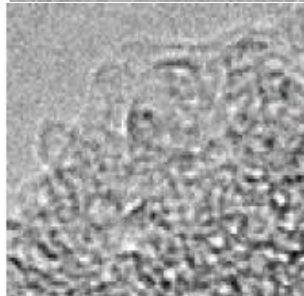
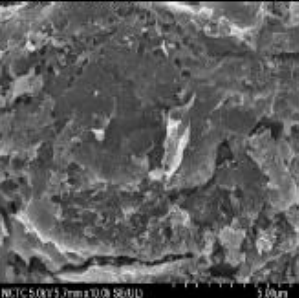
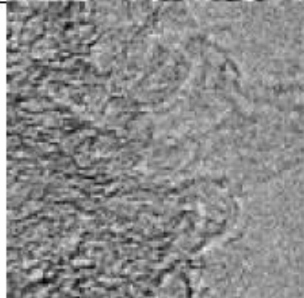
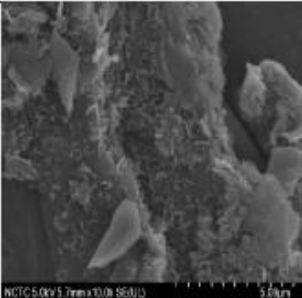
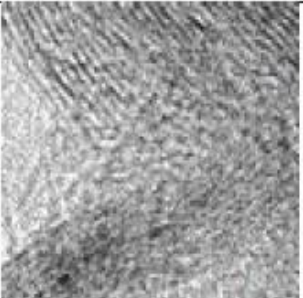
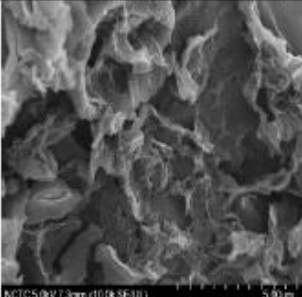
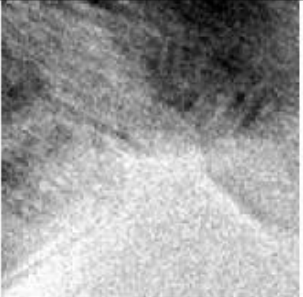
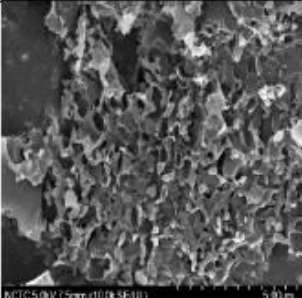
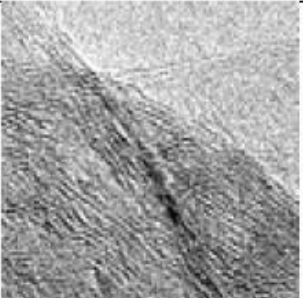
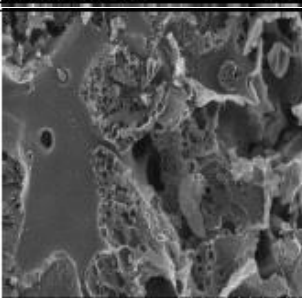
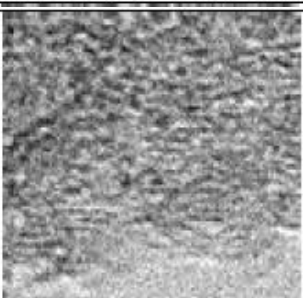
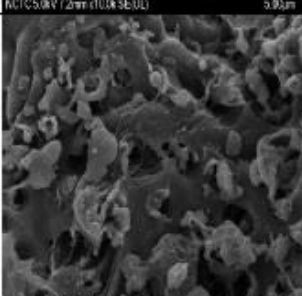


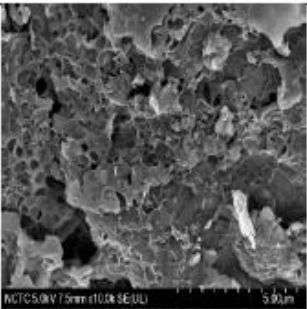
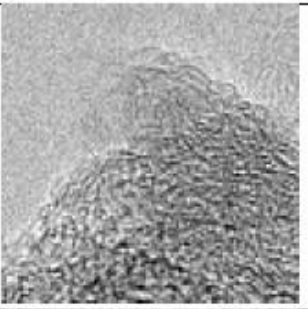
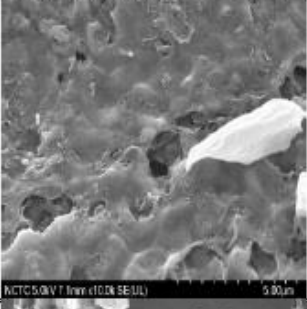
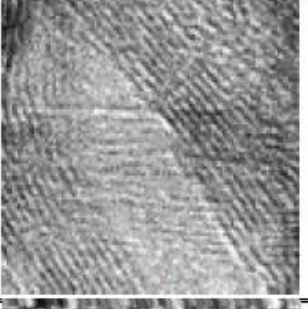
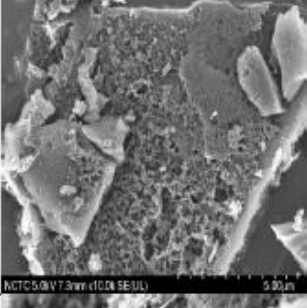
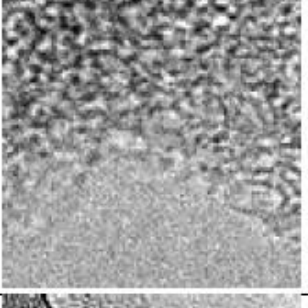
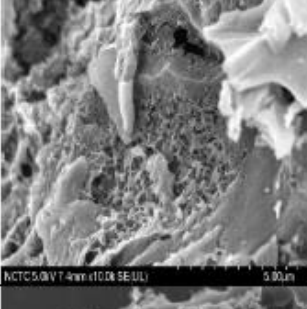
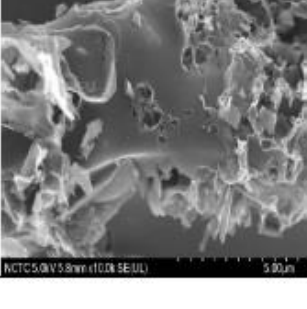
Figure 7 X-ray diffraction patterns of biomass activated carbon (a) EFB, (b) SB, (c) LN, (d) PS and (e) WC

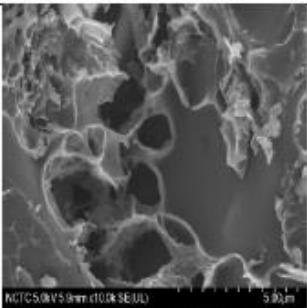
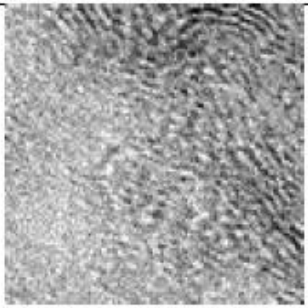
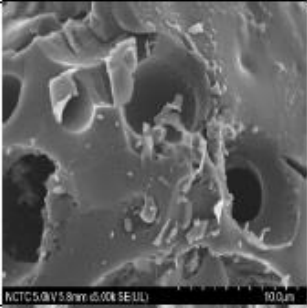
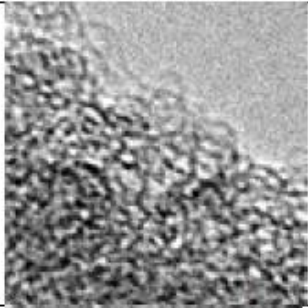
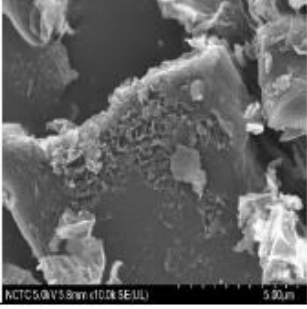
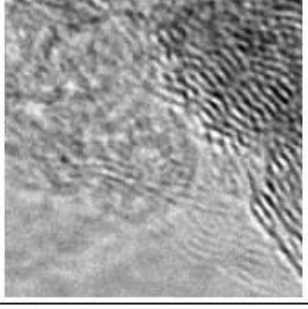
Table 5 compiles Scanning electron images (SEM) and Transmission electron images (TEM) of activated carbons synthesised under various conditions.

Table 5 SEM and TEM images of biomass activated carbon

| Biomass                                  | KOH : Char<br>(by weight) | Activation<br>Temp. (°C) | SEM  | TEM   |
|--|---------------------------|--------------------------|--|---|
| Palm<br>Empty<br>Fruit<br>Bunch<br>(EFB) | 1:1                       | 700                      |    |    |
| Palm<br>Empty<br>Fruit<br>Bunch<br>(EFB) | 1:1                       | 800                      |   |   |
| Palm<br>Empty<br>Fruit<br>Bunch<br>(EFB) | 1:1                       | 900                      |  |  |
| Palm<br>Empty<br>Fruit<br>Bunch<br>(EFB) | 2:1                       | 700                      |  |  |
|  |                           | 800                      |  |  |

| Biomass            | KOH : Char<br>(by weight) | Activation<br>Temp. (°C) | SEM  | TEM   |
|--------------------|---------------------------|--------------------------|--|---|
|                    |                           | 900                      |    |    |
| Palm shell<br>(PS) | 1:1                       | 700                      |    |    |
|                    |                           | 900                      |   |   |
| Palm shell<br>(PS) | 2:1                       | 700                      |  |  |
|                    |                           | 900                      |  |  |

| Biomass                      | KOH : Char<br>(by weight) | Activation<br>Temp. (°C) | SEM  | TEM   |
|------------------------------|---------------------------|--------------------------|--|---|
| Sugarcane<br>bagasse<br>(SB) | 1:1                       | 700                      |    |    |
| Sugarcane<br>bagasse<br>(SB) | 1:1                       | 900                      |    |    |
| Sugarcane<br>bagasse<br>(SB) | 2:1                       | 700                      |   |   |
|                              | 2:1                       | 900                      |  |  |
| Lignin<br>(LN)               | 1:1                       | 700                      |  |  |

| Biomass        | KOH : Char<br>(by weight) | Activation<br>Temp. (°C) | SEM   | TEM  |
|----------------|---------------------------|--------------------------|---|--|
|                |                           | 900                      |   |   |
| Lignin<br>(LN) | 2:1                       | 700                      |   |   |
|                |                           | 900                      |  |  |

Scanning electron micrographs for activated carbon samples activated at 700 °C using KOH: Char ratio equal to 1 have relatively smooth surface. When increasing the amount of KOH used to KOH: Char equal to 2:1, the activated carbon show macrospores clearly visible on the surface. Transmission electron micrographs of all activated carbon samples contained amorphous carbon, except the activated carbon which was activated at 900 °C showed a small graphite-like structure which was a short range ordered structure imbedded in the amorphous matrix.

### 2.2.2.3 Electrochemical Performance Evaluation

To prepare working electrodes, activated material (Activated carbon) derived from various biomass was mixed with acetylene black (DENKA black Li-100) and binder PTFE (DuPont 6-J) in a mass ratio of 80:10:10, using ethanol as a dispersant. The obtained mixture was then made into a sheet and cut to 5mm x 5mm, then dried in vacuum oven at 80°C for 12 hours. The electrochemical performance of the prepared electrodes was studied in a three-electrode system (Figure 8) using a HZ-Pro S12 Multi Electrochemical Measurement System (at Kyoto University, Japan). An Ag/AgCl electrode, and a Pt mesh were used as a reference electrode and a counter electrode, respectively. Aqueous 1M H<sub>2</sub>SO<sub>4</sub> is a base electrolyte.

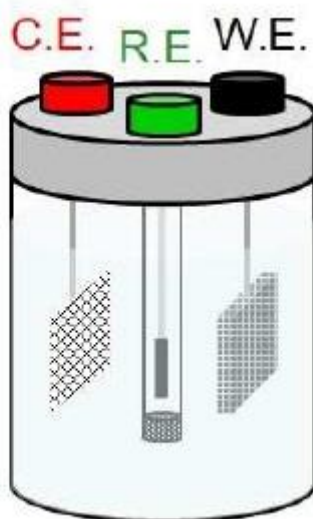


Figure 8 The three-electrode system for electrochemical performance testing

#### Cyclic Voltammetry

The three-electrode cells with activated carbon electrode were subjected to cyclic voltammetry measurements, in order to determine the mechanism(s) for charge storage. A reaction peak in CV results would indicate that a charge storage takes place via reactions, which would yield pseudocapacitance. If no reaction peaks are observed, a charge storage is assumed to be mainly by electrostatic forces. Figure 9 shows the cyclic voltammetry results for the best-performing cells, where the carbon electrode is made from various biomass activated at 700°C using KOH: Char = 2:1 by weight. The trend with voltage scan rate was typical for supercapacitor cells, in that a wider voltammogram, i.e., higher current, was observed when a higher scan rate was used. The generated current is proportional to the scan rate. However, at slower scan rate, this process allows slower reaction to take place. Activation conditions affect the capacity, when increasing the KOH: Char ratio, the results tend towards high capacity and increasing of activation temperature tend towards the square shape and larger CV area at 20 mVs<sup>-1</sup>. Activated carbon sample from EFB at KOH: Char ratio equal to 2 has the largest CV area and thus has the best electrochemical performance.

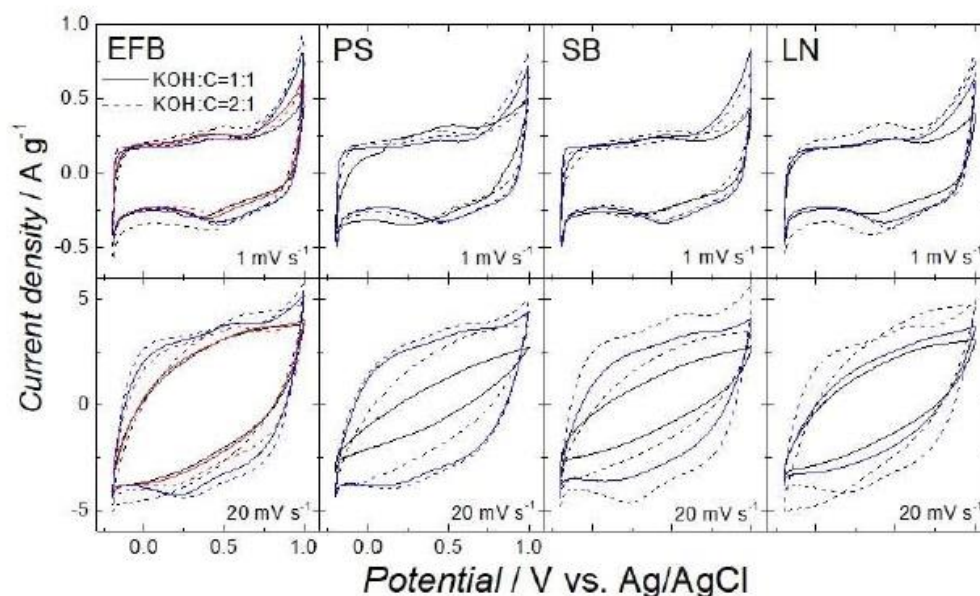


Figure 9 Typical cyclic voltammetry results of 3-electrode supercapacitor cell with biomass activated carbon electrode, Empty palm fruit bunch (EFB), Palm shell (PS), Sugarcane bagasse (SB) and Lignin (LN)

#### Galvanostatic Charge-Discharge

The three-electrode cells made from various biomass-derived activated carbons were tested by charging and discharging between 0 – 0.6 V using constant current levels of 0.1, 0.2, 0.5, 1 and 2 A/g of activated carbon. The specific capacitance,  $C_{sp}$ , which is calculated per weight of activated

$$C_{sp} \left( \frac{F}{g} \right) = \left( \frac{i \Delta t}{M \Delta V} \right) \quad (1)$$

where  $i$  is the discharge current (A),  $\Delta t$  is the amount of time to discharge (s),  $\Delta V$  is the difference in voltage from charged to discharged state (V), not including the IR drop due to equivalent series resistance (ESR) and  $M$  is the mass of the activated carbon in the electrodes (g). Typical charge-discharge diagram is shown in Figure 10.

A summary of the specific capacitance values obtained by galvanostatic chargedischarge test for the activated carbon samples synthesised under various conditions are shown in Figures 11-12. All activated carbons activated at 700°C had slightly higher capacitance than those activated at 900°C. For these samples, when comparing those treated using the same amount of KOH, the BET surface area and total pore volume values were not drastically different. However, the relative amount of micropore to mesopore was higher in those treated at 700 °C, which may have contributed to the higher capacitance. However, with increasing KOH: Char ratio at both activation temperatures, from 1:1 to 2:1 yielded higher specific capacitance value that may be contributed by high BET surface area as well as high pore volume.

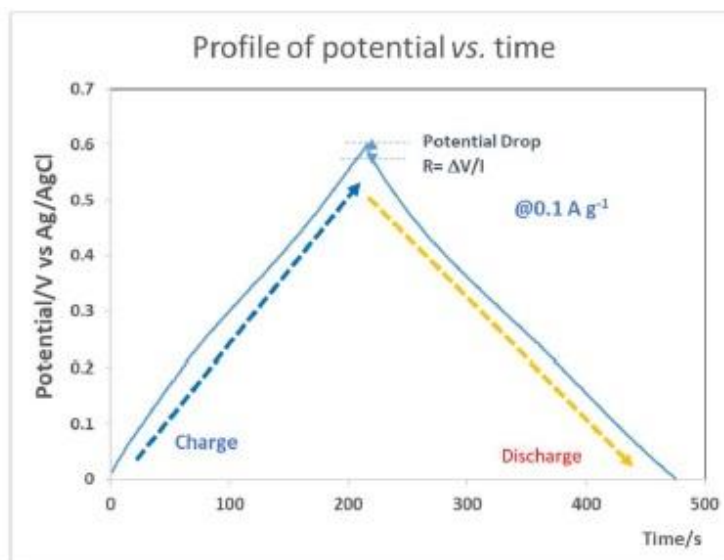


Figure 10 Typical Galvanostatic Charge-Discharge diagram

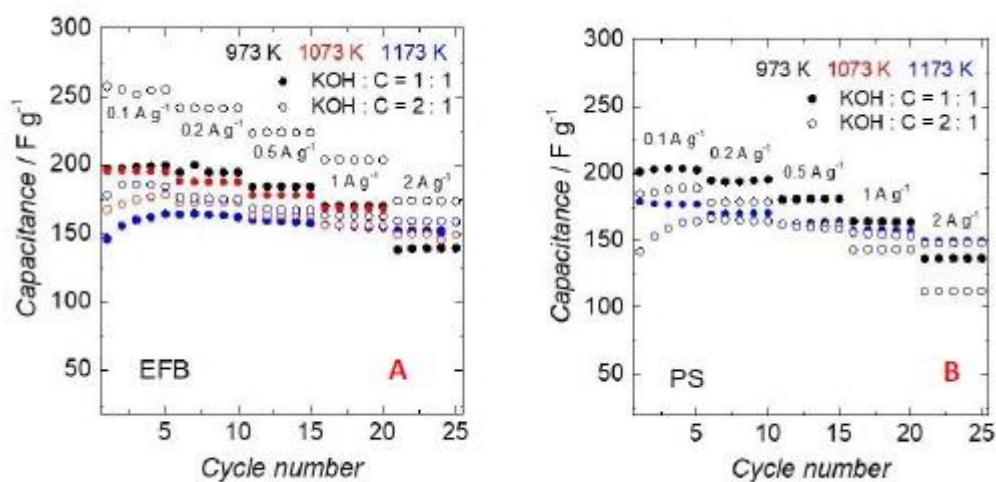


Figure 11 Capacitance VS cycle number at each current density (A) EFB, (B) PS

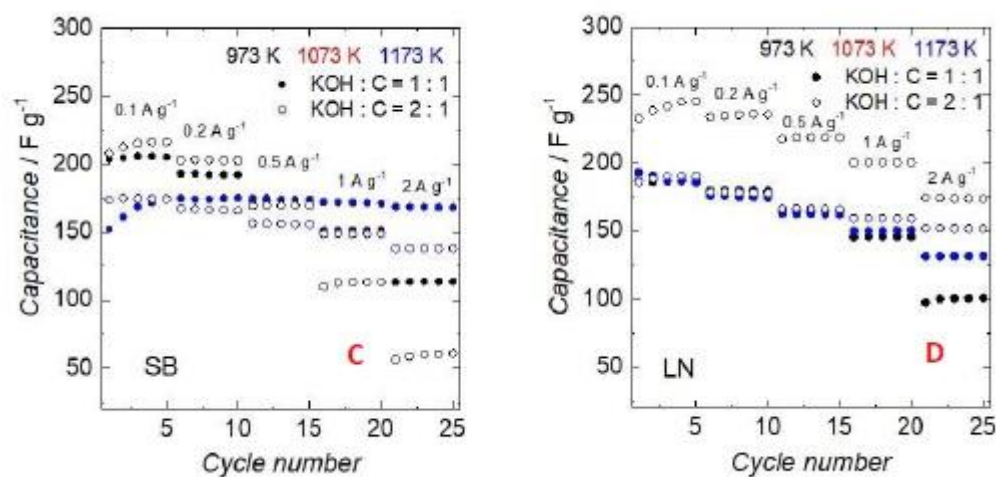


Figure 12 Capacitance VS cycle number at each current density (C) SB, (D) LN

Table 6 Summary of capacitance of activated carbon electrodes from each condition

| Materials                       | KOH:C     | Activation Temp. | Capacitance at each current density, F g <sup>-1</sup> |                       |                       |                     |                     |
|---------------------------------|-----------|------------------|--|-----------------------|-----------------------|---------------------|---------------------|
|                                 | by weight | °C               | 0.1 A g <sup>-1</sup>                                  | 0.2 A g <sup>-1</sup> | 0.5 A g <sup>-1</sup> | 1 A g <sup>-1</sup> | 2 A g <sup>-1</sup> |
| Lignin (LN)                     | 1:1       | 700              | 186.73   | 180.04                | 165.35                | 145.94              | 99.99               |
|                                 |           | 900              | 176.55   | 170.39                | 160.41                | 149.38              | 123.28              |
|                                 | 2:1       | 700              | 254.46   | 252.64                | 242.29                | 231.54              | 214.78              |
|                                 |           | 900              | 189.35   | 178.36                | 166.47                | 159.40              | 151.99              |
| Palm Empty Fruits Bunches (EFB) | 1:1       | 700              | 198.58   | 195.80                | 184.25                | 170.30              | 139.07              |
|                                 |           | 800              | 195.58   | 187.74                | 177.84                | 168.27              | 149.56              |
|                                 |           | 900              | 157.61   | 163.53                | 158.94                | 155.39              | 153.20              |
|                                 | 2:1       | 700              | 277.02   | 251.03                | 228.26                | 212.36              | 188.97              |
|                                 |           | 800              | 175.28   | 172.93                | 163.08                | 155.87              | 148.55              |
|                                 |           | 900              | 183.89   | 175.79                | 167.51                | 162.83              | 159.00              |
| Sugarcane Bagasse (SB)          | 1:1       | 700              | 192.40   | 194.17                | 184.49                | 169.15              | 131.84              |
|                                 |           | 900              | 165.78   | 174.73                | 174.21                | 171.87              | 168.51              |
|                                 | 2:1       | 700              | 213.85   | 203.17                | 169.68                | 112.55              | 59.39               |
|                                 |           | 900              | 178.14   | 166.72                | 156.29                | 148.84              | 138.06              |
| Palm Shell (PS)                 | 1:1       | 700              | 289.47   | 223.75                | 193.48                | 157.23              | n/a                 |
|                                 |           | 900              | 182.06   | 170.43                | 163.30                | 157.59              | 149.97              |
|                                 | 2:1       | 700              | 223.52   | 212.30                | 171.56                | 187.70              | 154.30              |
|                                 |           | 900              | 156.31   | 165.37                | 159.99                | 154.61              | 147.82              |

A summary of the specific capacitance values obtained from galvanostatic chargedischarge testing for the activated carbons synthesised under various conditions is shown in Table 6. Activated carbon samples from EFB, SB, and Lignin prepared at activation temperature of 700 °C and KOH: Char ratio equal to 2 exhibit the highest capacity at 0.1 A/g charge/discharge rate, except PS (11700=PS) sample from KOH: Char = 1:1 that has the highest capacity at 0.1 A/g charge/discharge rate. The rate capability should be evaluated together with the specific capacity value. From current results, activated carbon prepared at activation temperature 900°C and KOH: Char = 2:1 has shown better rate capability. Thus the optimum condition for this electrochemical storage system is still ongoing to improve both capacity value and rate capability.

## 2.3 Project output

### 2.3.1 Student exchange

- Two students, Miss Sicha Arayatham and Mr. Tan Vongvarotai, from Thammasat University visited Kyoto University under the W&W Internship program in December 2018.

# **Nanocarbon Materials for Sustainable Production and Storage of Green Fuels and Platform Chemicals**

### 3. Nanocarbon Materials for Sustainable Production and Storage of Green Fuels and Platform Chemicals

Research team:

Prof.Dr. Noriaki Sano, Kyoto University (PI, Japan side)

Dr. Kajornsak Faungnawakij, NANOTEC, NSTDA (PI, Thailand side)

Dr. Sanchai Kuboon, NANOTEC, NSTDA

Dr. Pongkarn Chakthranont, NANOTEC, NSTDA

Miss. Sutarat Thongratkaew, NANOTEC, NSTDA

Dr. Supawadee Namuangruk, NANOTEC, NSTDA

Dr. Chompoonut Rungnim, NANOTEC, NSTDA

Dr. Pussana Hirunsit, NANOTEC, NSTDA

Dr. Manaschai Kunaseth, NANOTEC, NSTDA

Assoc. Prof. Tawatchai Charinpanitkul, Chulalongkorn University

Dr. Chompoopitch Termvidchakorn, Chulalongkorn University

Dr. Sareeya Bureekaew, VISTEC

Asst. Prof. Thongthai Witoon, Kasetsart University

#### 3.1 Purpose of Collaborative Research

The catalytic production of carbon-based materials, biofuels and biochemicals is a key activity in biorefinery industry. Also, developments in catalytic energy conversion and energy storage using bioactivities are important for sustainable societies. Consequently, searching for renewable resources that are reliable, sustainable and environmentally friendly is the big challenge, and these lead to green concepts including biorefinery and bio-energy devices where renewable resources drive the world. Under such circumstances, the collaborative researches carried out by the groups in NANOTEC/NSTDA (Faungnawakij's team) and Kyoto University (Sano's team) will attack this issue via accumulating innovative knowledge about biomass conversion to useful materials and development of bio-energy devices.

In this year, three major research activities have been done as follows.

- Investigation of Hydrogen Adsorption Mechanism on CNH using DFT Calculation
- Investigation of Carbon-Based Catalysts for an Electrochemical H<sub>2</sub>O<sub>2</sub> Production from O<sub>2</sub>
- Investigation of Nanocatalysts for gamma-valerolactone production from biomass derivatives

## 3.2 Research Progress

### 3.2.1 Investigate hydrogen adsorption mechanism on CNH using DFT calculation

#### 3.2.1.1 Generated CNH structures

The shape of carbon nanohorn relates to the number of pentagon rings at the cone tip. In this work, carbon nanohorn was represented by a cone model with five pentagon rings suggested from the cone declination of  $19^\circ$  in the TEM images of single-wall CNH tips. We modeled the pristine CNH and named it as NH model which consists of 103 carbon atoms. The Pt supported on mono-vacancy nanohorn was created by removing one carbon atom at the tip of CNH (called as vNH) and then replaced a Pt atom and a Pt<sub>4</sub> cluster at this single vacancy site named as Pt-vNH and Pt<sub>4</sub>-vNH models, respectively. Likewise, the model of GP with single Pt on its mono-vacancy is named Pt-vGP model. The optimized geometries of the three models are depicted in Figure 1-1. Note that all models in this work are non-hydrogen terminated models. All structures were optimized by Gaussian09 software package using the Becke three-parameter hybrid functional (B3LYP). The 6-311G(d,p) basis set was applied for C and H atoms while the cc-pVTZ-PP basis set was employed for Pt atoms.

All calculations were calculated at singlet state which is the low lying energy state of the systems. Thermodynamic results such as Gibbs free energy (G) derived from statistical thermodynamics have been computed at 298 K in the gas phase at the same level of theory. The optimized C-C bond distances of pristine nanohorn (NH model) are in the range of  $1.42 \pm 0.04$  Å and the H-H bond distance of H<sub>2</sub> molecule is 0.74 Å, which agrees with reported experimental and theoretical studies. All natural atomic charges in this work were calculated from the natural bond orbital (NBO) analysis using NBO version 3.

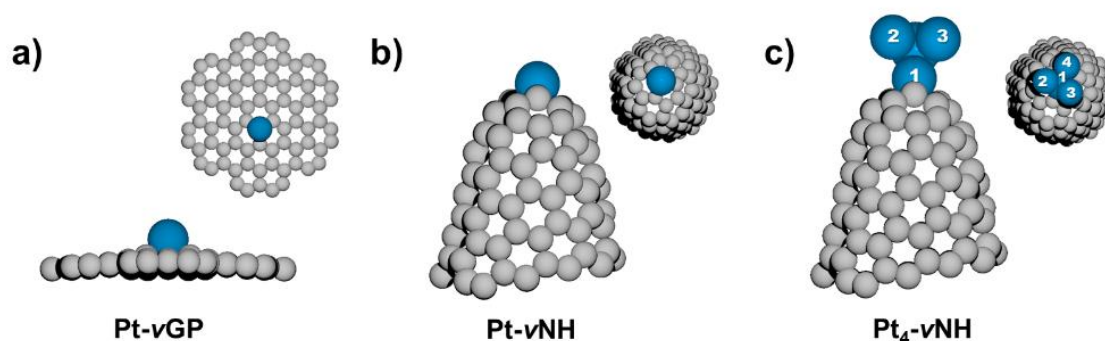


**Figure 1-1.** Optimized geometries of a Pt atom supported on mono-vacancy of a) graphene and b) carbon nanohorn. c) a Pt<sub>4</sub> cluster supported on mono-vacancy-carbon nanohorn.

#### 3.2.1.2 Calculated hydrogen adsorption energy

Basically, H<sub>2</sub> adsorption over metal supported carbon-based materials can be classified into two different types; (1) non-dissociative H<sub>2</sub> adsorption named as Kubas adsorption (K-mode) and (2) dissociated dihydride adsorption (D-mode). For d<sup>10</sup> transition metals such as Ni, Pt, and Pd, it has been reported that the H<sub>2</sub> adsorption over those single

metals supported on GP and CNT are stable in both K- and D-modes depending on position and configuration of the metal on carbon supports.

On Pt-vGP, the Pt reactivity toward  $H_2$  adsorption is not powerful due to the Pt-C interactions at the vacancy site are very strong. As a result, the  $H_2$  adsorptions in K- and D-modes are very weak with the  $E_{ads}$  of -0.10 and -0.07 eV, respectively. In contrast, the  $H_2$  adsorptions in the K- and D-mode on the Pt-vNH are more stable with  $E_{ads}$  of -0.42 and -0.43 eV, respectively. We have tested the  $H_2$  adsorption in Pt-vNH model with H-termination and observed the  $E_{ads}$  of -0.31 and -0.33 eV for the K- and D-mode of  $H_2$  adsorption, respectively. Thus, the  $H_2$  adsorption at the vNH cone tip in the present study has been affected by H-termination in small extent. In both Pt-vGP and Pt-vNH systems, only one  $H_2$  molecule can be adsorbed on the supported Pt atom. Without the supported Pt atom, weak  $H_2$  physisorption is detected on pristine NH model ( $E_{ads} \sim -0.09$  eV) and pristine GP (-0.01 eV). Therefore, the presence of Pt atom in Pt-vNH obviously enhances the  $H_2$  adsorption strength compared to the adsorption on NH, GP, and Pt-vGP. We note that the removing of the hydrogenated Pt ( $PtH_2$ ) from vNH requires the large energy of 4.92 eV. Thus, this  $PtH_2$  is strongly bound at the vacancy site of vNH with Pt-C bond around 1.9 - 2.1 Å.

Effect of Pt particle size on the hydrogen adsorption has been considered on  $Pt_4$ -vNH. The first  $H_2$  molecule is readily dissociated on a Pt atom of the  $Pt_4$  cluster with  $E_{ads}$  of -1.73 eV and each H atom hold positive charge at  $0.05e$ . The adsorption capacity is measured by increasing number of adsorbed H atoms. As shown in Figure 1-2, up to six  $H_2$  molecules can be dissociated and chemisorbed on the supported  $Pt_4$  with  $E_{ads/H_2}$  of -0.79 eV/ $H_2$ . As a result of unavailable dissociative adsorption site on the  $Pt_4$  cluster, the seventh  $H_2$  molecule becomes physisorption with  $\Delta E$  of -0.07 eV. The maximum dissociative adsorption capacity per Pt atom raises up from 1 to 1.5  $H_2$ /Pt when the size of metal cluster is enlarged from a Pt atom to  $Pt_4$  cluster. Note that the maximum capacity is lower than that of the unsupported  $Pt_4$  cluster (2  $H_2$ /Pt).

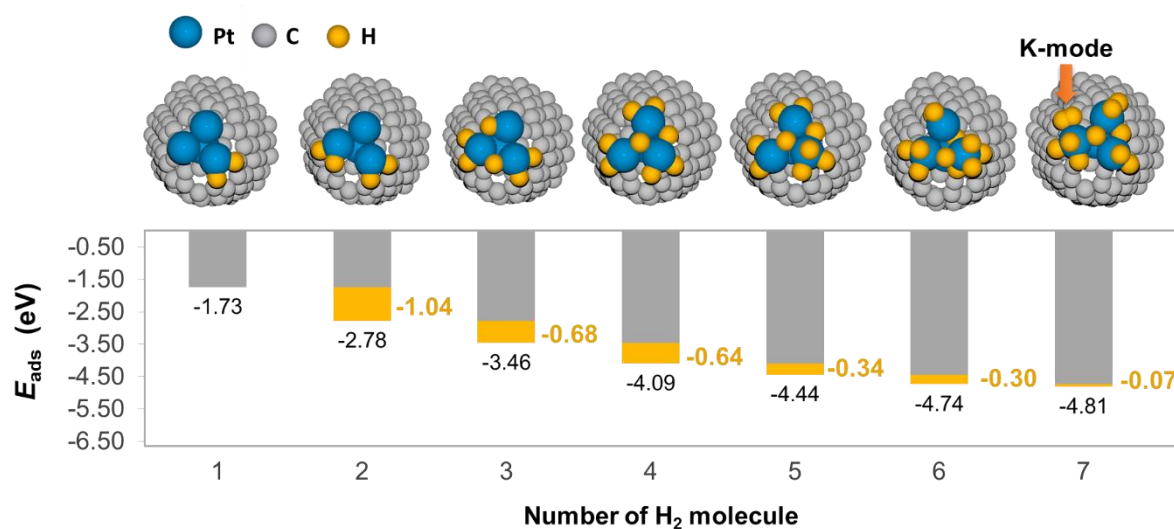


**Figure 1-2.**  $H_2$  adsorption energies and optimized geometries of various dissociative hydrogen adsorptions on  $Pt_4$ -vNH. The sequential  $H_2$  adsorption energy ( $\Delta E$ ) is shown in the yellow color.

In non-defective carbon systems such as GP and CNT, the binding strength of small metal nanoparticles are moderately stable with the binding energies < 2 eV. When  $H_2$  is coordinate to the system, metal-carbon bond distances in GP and CNT supports increase around 0.02 – 0.17 Å. Such

increase in the metal-carbon distance results in weakening interactions between metal and non-defective carbon support that might activate metal-H<sub>2</sub> complex migration and aggregation. For Pt<sub>4</sub>-vNH in this work, the full H-saturated Pt<sub>4</sub> cluster or Pt<sub>4</sub> with 6 adsorbed H<sub>2</sub> molecules (Pt<sub>4</sub>H<sub>12</sub>) firmly settles at the vacancy site of vNH with a strong Pt-C bond in the length of 1.9–2.0 Å. Additionally, the removing Pt<sub>4</sub> cluster with 6 Pt<sub>4</sub>H<sub>12</sub> from vNH requires high energy at least 7.22 eV. As a result, the defective CNH is a proper material for metal support in the H<sub>2</sub> storage application. The metal firmly deposited at the vacancy site of vNH even when the metal meets H<sub>2</sub> saturation.

### 3.2.2 Investigation of Carbon-Based Catalysts for an Electrochemical H<sub>2</sub>O<sub>2</sub> Production from O<sub>2</sub>

#### 3.2.2.1 CNHs Catalyst Preparation

Carbon nanohorns (CNHs) were synthesized using the aforementioned gas-injected arc-in-water (GI-AIW) method. In short, a set of graphite anode and cathode was submerged in de-ionized water contained in a beaker. Direct electrical current of 80 amperes was supplied from a power source for generating arc discharge between both electrodes. The anode was moved toward the inner surface of the cathode hole by a step motor with a speed of 5.25 mm/s. In this work, 2 types of graphite rods with a diameter of 6 mm and a length of 75 mm, one with 99.9995% purity and the other with unknown purity, were used as anodes. The CNHs synthesized from high purity and unknown purity were denoted as CNH1 and CNH2 respectively. A graphite rod with a diameter of 20 mm and a length of 55 mm was used as a cathode. The synthesized products were collected after being dried in an oven set at 90 °C overnight.

Oxygen-doped CNHs catalyst, O-CNH, was synthesized by immersing a mixture of CNHs and KOH with 1:4 weight ratio in water for 8 hours. The mixture was dried in an oven at 80 °C overnight, followed by heating in air with a heating rate of 3 °C/min ramp and hold at 600 °C for 1 hour. The catalyst was washed and dried again at 90 °C overnight.

Nitrogen-doped CNHs catalyst, N-CNH, was synthesized by immersing a mixture of CNHs and melamine with 1:6 weight ratio in 80% ethanol-water for 5 hours. The mixture was dried in an oven at 105 °C overnight, followed by heating in N<sub>2</sub> atmosphere using a ramp rate of 10 °C/min ramp and hold at the 850 °C for 2 hour.

Catalyst inks were prepared by adding 5 mg of the CNH catalyst into a vial, followed by 980 µL of 200 proof ethanol and 20 µL of 5 wt% Nafion solution. The mixture was dispersed by sonication for 1 hour. 10 µL of the ink solution was added to the 4 mm diameter glassy carbon disk (Sigradur G HTW Hochtemperatur-Werkstoffe GmbH) and spin-dried at 300 rpm for at least 30 minutes.

#### 3.2.2.2 Characterizations

Crystallographic identification of each typical catalyst was performed by X-ray diffractometry (XRD, Bruker, D8 advance) using CuKα radiation operated at 40 kV and 100 mA with a scanning step of 0.03°/min in a range of 10–80°. Samples were prepared using Si low background as a sample holder.

Morphology of each catalyst sample were investigated by transmission electron microscope (TEM, JEOL, JEM-2100Plus).

BET surface area of each carbonaceous support material and catalyst samples was characterized by N<sub>2</sub> sorption. Brunauer–Emmett–Teller (BET) equation was used to determine the specific surface area of each sample.

Thermal stability analysis of each catalyst sample was conducted by thermogravimetric analyzer (TGA, PerkinElmer, TGA 8000). Sample of each catalyst placed in a ceramic pan was heated in an oxygen flow from the ambient temperature up to 1000 °C with a heating rate of 5 °C/min.

Hydrogen-temperature-programmed reduction (H<sub>2</sub>-TPR) analysis of each catalyst was performed using chemisorption analyzer (Quantachrome, ChemStar) equipped with a thermal conductivity detector to confirm the reduction behaviors of the catalyst. 20 mg of each catalyst was put in a U-tube sample cell and then pretreated under He atmosphere at 150°C for 1 h. After being purged by Ar flow for 30 min and cooled down to 50°C, the catalyst sample was heated again to 850°C with a heating rate of 5°C/min in a 5% H<sub>2</sub>/Ar flow.

### 3.2.2.3 Electrochemical Testing

The electrochemical O<sub>2</sub> reduction activity of each catalyst was measured using a rotating ring-disk electrode (RRDE) setup, which is a 4-electrode electrochemical system consisting of a carbon disk working electrode, a platinum ring working electrode, a platinum wire counter electrode, and a Ag/AgCl reference electrode. The reaction was performed in 0.1M KOH (99.99%, Sigma-Aldrich) continuously purged with 99.99% O<sub>2</sub> gas with a flow rate of 50 mL/min. RRDE experiment was carried out by scanning the disk potential from 0.2 V and 1.1 V vs. RHE at 10 mV/s while holding the Pt ring at 1.2 V vs. RHE to oxidize H<sub>2</sub>O<sub>2</sub> formed on the disk electrode. The rotating speed of the RRDE was 1600 rpm.

The system's ring collection efficiency was determined using the reversible [Fe(CN)<sub>6</sub>]<sup>4-/3-</sup> redox couple. RRDE measurement using Pt disk and Pt ring was performed in 10 mM of K<sub>4</sub>Fe(CN)<sub>6</sub> in 0.1 M KOH at varying rotating speed (400, 900, 1600, 2500, 3600 rpm). The selectivity of H<sub>2</sub>O<sub>2</sub> can be calculated as follow:

$$\text{H}_2\text{O}_2(\%) = 200 \frac{\frac{I_R}{N}}{I_D + \frac{I_R}{N}}$$

Where I<sub>R</sub> is the ring current, I<sub>D</sub> is the disk current, and N is the ring collection efficiency.

The ORR activity was measured by subtracting the current density of carbon disk measured in O<sub>2</sub>-purged electrolyte by current density measured in Ar-purged electrolyte. The CV was corrected for 100% ohmic loss, measured by impedance spectroscopy. Lastly the electrochemical active surface area (ECSA) was assessed by CV scans between -0.2 to 0.2 V vs. Ag/AgCl at varying scan rate (5, 10, 25, 50, 100 mV/s) in an Ar-purged electrolyte.

### 3.2.2.4 Results and Discussion

#### - Ring Efficiency Measurement

To quantify the amount of H<sub>2</sub>O<sub>2</sub> generated from the catalyst, the ring collection efficiency of the system must be quantified by performing RRDE measurements at 400, 900, 1600, 2500, and 3600 rpm rotating speed as shown in Figure 2-1. The ring collection efficiency, which is the ratio of

detectable product vs. produced product, was estimated by fitting a linear relationship through  $I_R$  and  $I_D$  measured at the diffusion limited current (0 V vs. Ag/AgCl) and found to be 0.2481.

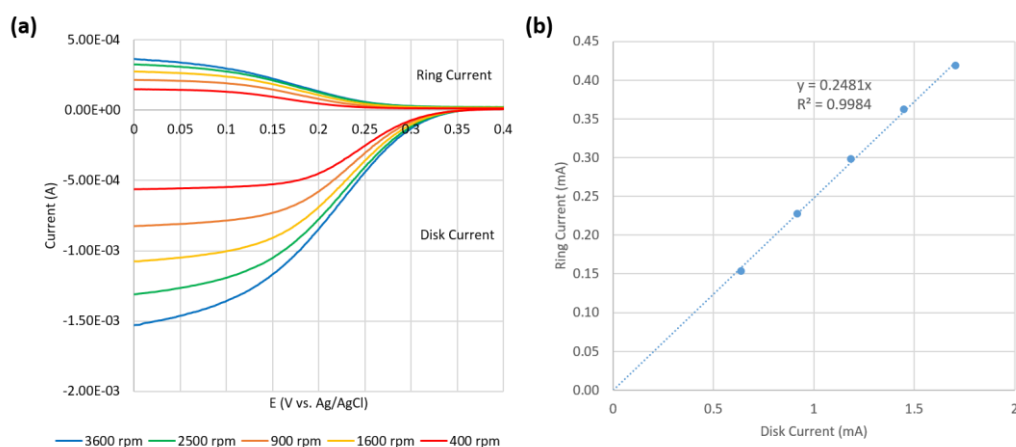


**Figure 2-1. (a) RRDE experiment in 10 mM of  $K_4Fe(CN)_6$  in 0.1 M KOH at varying scan rates and (b) the Ring collection efficiency**

### - Physical and Chemical Characterizations

XRD patterns in Figure 2-2 demonstrate that all CNHs catalysts exhibit a characteristic peak at  $2\theta$  of 26.8 degree, representing the graphitic structure. The intensity of graphitic peak in CNH1 is stronger than CNH2, implying higher crystallinity. Interestingly, the graphitic peaks for both O-CNH1 and O-CNH2 are stronger than that of regular CNHs and N-CNHs. TEM images in Figure 2-3 show that the structure of CNH1 and CNH2 and their derivatives appear similar and the characteristic structure of CNHs can be easily seen in CNH1 and O-CNH1, and less so in CNH2 and O-CNH2. However, the structures differ significantly in the case of N-CNHs.

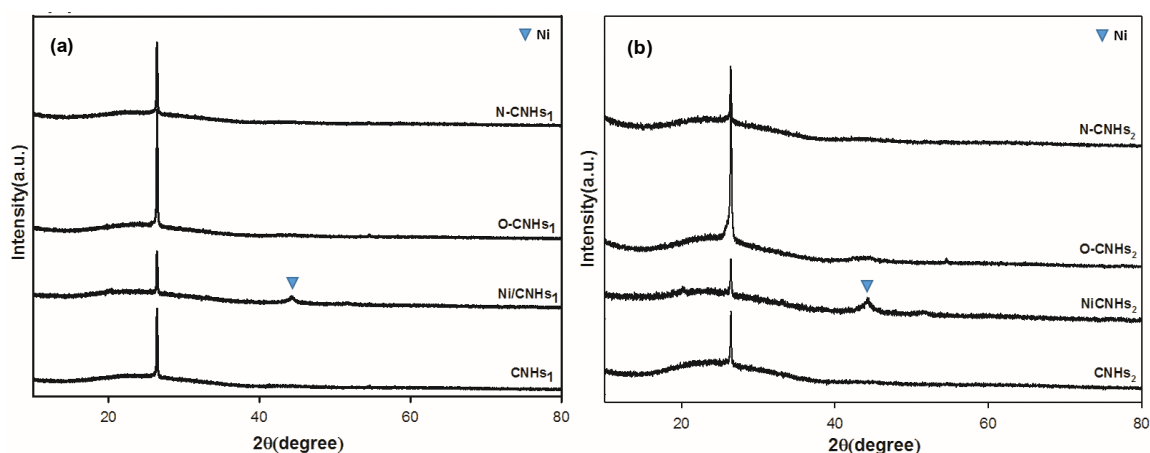


**Figure 2-2. XRD patterns of (a) CNH1 and (b) CNH2 with various surface treatment.**

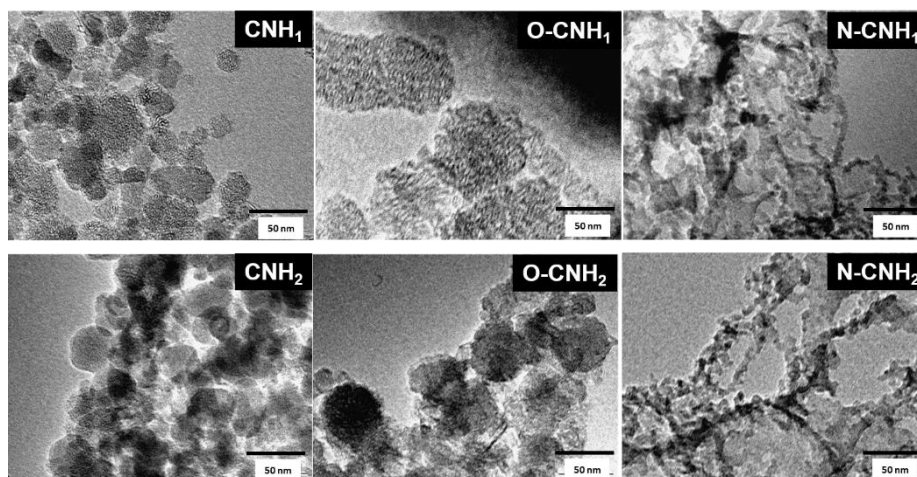


**Figure 2-3. TEM images of CNHs with various surface treatment.**

BET surface areas of each catalyst is shown in Table 2-1. Overall, the CNH1 catalysts and their derivatives has higher BET surface areas. The O-CNHs exhibit roughly 3 times increase in BET surface area compared to that of undoped CNHs. N-CNHs also demonstrate higher BET surface area compared to undoped CNHs.

**Table 2-1. BET surface area of each catalyst sample**

| Catalysts | BET surface area [m <sup>2</sup> /g] |
|-----------|--------------------------------------|
| CNH1      | 301.1                                |
| O-CNH1    | 912.6                                |
| N-CNH1    | 499.7                                |
| CNH2      | 207.1                                |
| O-CNH2    | 585.9                                |
| N-CNH2    | 318.9                                |

Figure 2-4 shows that the TPR profile of CNH1 and O-CNH1 consists of one reduction peak at 700 C which belongs to O-species, while the TPR profile of N-CNH1 has an extra peak at 400 C which is the reduction peak of N-species.

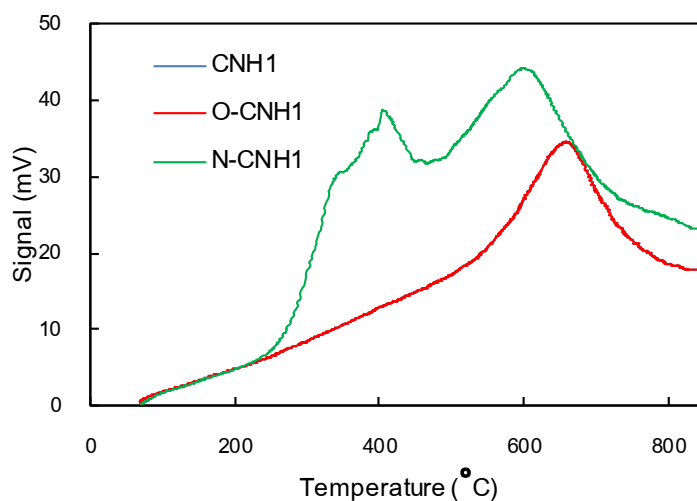


**Figure 2-4. TPR profiles of CNH1 catalysts**

### - Electrochemical Activity

Electrochemical measurements from the RRDE show that the CNH2 catalyst and its derivatives are highly active for the ORR. Doping the CNH2 with O and N can drastically improve the current onset (at  $-0.1 \text{ mA/cm}^2$ ) from  $0.77 \text{ V vs. RHE}$  to  $0.78$  and  $0.89$  for O-CNH2 and N-CNH2 respectively (Figure 2-5 a and Table 2-2). However, doping reduces the selectivity of CNH2 catalyst towards  $\text{H}_2\text{O}_2$ . At  $0.5 \text{ V vs. RHE}$ , the selectivity  $\text{H}_2\text{O}_2$  of CNH2, O-CNH2, and N-CNH2 are  $70.7\%$ ,  $58.8\%$ , and  $21.3\%$  respectively (Figure 2-5 b).

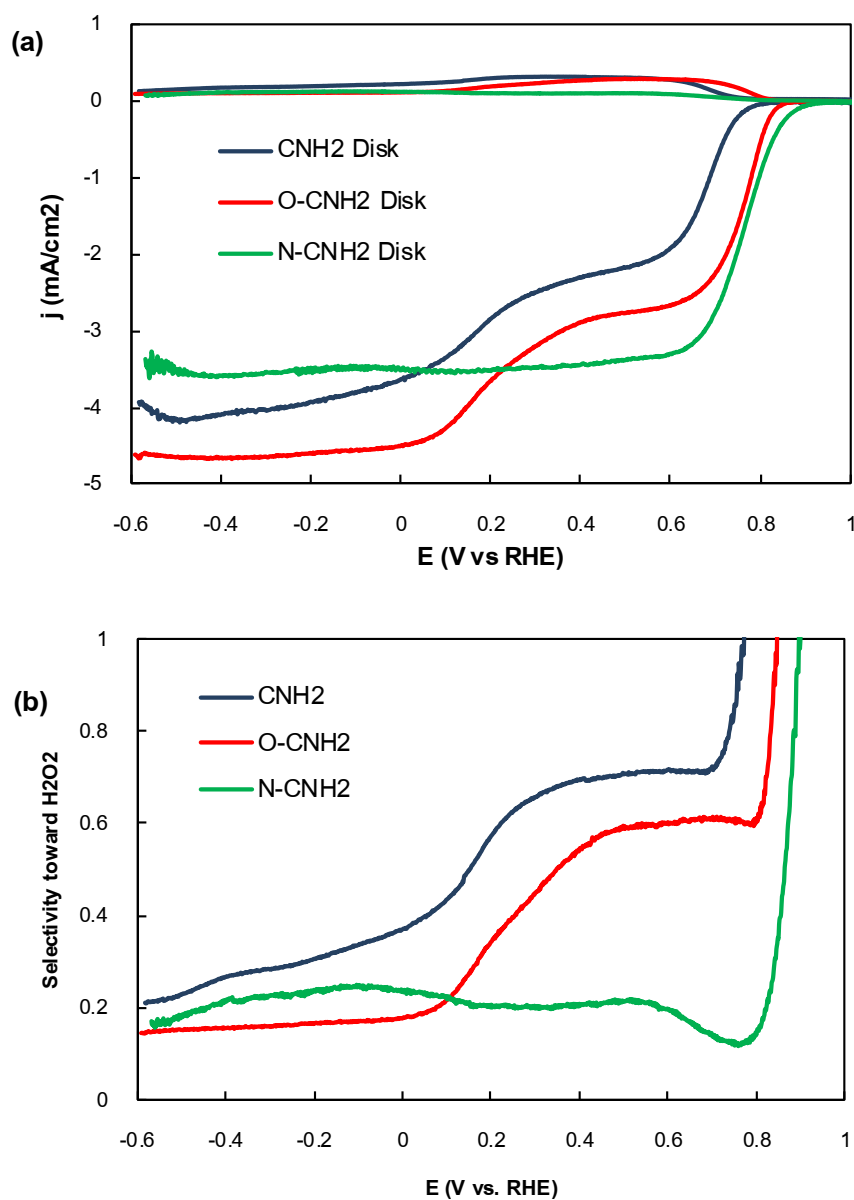


Figure 2-5. Electrochemical activity (a) Ring and Disk current density and (b) selectivity toward H<sub>2</sub>O<sub>2</sub>.

Table 2-2. Loading, double layer capacitance ( $C_m$ ), and H<sub>2</sub>O<sub>2</sub> selectivity of each catalyst sample.

| Carbon catalyst | Loading ( $\mu\text{g}/\text{cm}^2$ ) | $C_m$ (F/g) | C ( $\mu\text{F}/\text{cm}^2$ ) | %O    | %N   | H <sub>2</sub> O <sub>2</sub> Selectivity (%) at 0.5 V vs. RHE | Onset potential at -0.1 mA/cm <sup>2</sup> |
|-----------------|---------------------------------------|-------------|---------------------------------|-------|------|--|--|
| CNH2            | 282.69                                | 9.32        | 2634.39                         | 3.34  | 1.29 | 70.70  | 0.77                                       |
| O-CNH2          | 269.63                                | 18.70       | 5042.91                         | 11.66 | 0    | 58.82  | 0.78                                       |
| N-CNH2          | 285.81                                | 10.72       | 3064.03                         | 2.31  | 2.05 | 21.31  | 0.89                                       |

### 1.2.2.5 Conclusion

CNHs catalysts were synthesized and modified to increase the O and N content. The catalysts were characterized by XRD, TEM, BET, TPR, and XPS. The electrochemical activity for the ORR of these catalysts are extremely promising. The as-prepared CNH2 demonstrated superb H<sub>2</sub>O<sub>2</sub> selectivity while the selectivity was lowered by the addition of O and even more so when N was added. The next step was to investigate the effects of doping concentrations on the activity and selectivity of these catalysts.

### 1.1.1 Comparative study for GVL production over non-carbon based supported catalysts

According to the previous report on excellent catalytic behavior of Ni hybridized with CNHs (Ni/CNHs) for GVL production, the CNHs showed superior behavior over other carbon-based support materials (activated carbon and carbon nanotubes). In this report, we would like to extend our study over a non-carbon based support, SBA-15 which is a well-known mesoporous material employed as versatile supports in many reactions. Moreover, an introduction of copper to the supported Ni catalysts for enhancement of GVL selectivity was investigated.

### 1.2.3.1 Catalyst Preparation

SBA-15 silica was synthesized via a hydrothermal process where] 4.0 g of Pluronic P123 (Sigma-Aldrich Chemical Co.) was dissolved in 150 mL of 1.6 mol/L HCl (Carlo Erba Reagents) solution. The resulting mixture was stirred for about 1 h until the solution became transparent. Then, 8.50 g of tetraethyl orthosilicate (TEOS, 98%, Sigma-Aldrich Chemical Co.) was added dropwise under continuous stirring at 40 °C. After stirring for 24 h, the mixture was transferred into an autoclave for a reaction at 100 °C for next 24 h. The precipitate product was collected by filtration and washed with water and followed by ethanol (Sigma-Aldrich Chemical Co.) for 3 times each. The sample was subsequently dried at 100 °C and then calcined at 550 °C for 6 h to remove the surfactant. The Ni/SBA-15, Cu/SBA-15, or Ni-Cu/SBA-15, catalysts were prepared by a glycol-assisted impregnation route. A typical catalyst, 5 wt % Ni and 5 wt % Cu on SBA-15, was synthesized by dispersing 0.11 g of Ni(NO<sub>3</sub>)<sub>2</sub>·6H<sub>2</sub>O (Ajax Finchem Pty Ltd), 0.08 g of Cu(NO<sub>3</sub>)<sub>2</sub>·3H<sub>2</sub>O (Ajax Finchem Pty Ltd), and 0.5 g of SBA-15 into 10 mL of ethylene glycol (Sigma-Aldrich Chemical Co.) and then the mixture was stirred overnight under vacuum. Subsequently, the samples were dried in a vacuum oven at 80 °C until the solvent was completely evaporated. Then the sample was calcined at 550 °C for 4 h in N<sub>2</sub>, followed by another 2 h in air. Finally, we obtained the product via reduction at 500 °C for 4 h in 5 % H<sub>2</sub>/Ar. This sample was denoted as Ni-Cu/SBA-15(EG). For comparison, Ni-Cu/SBA-15 catalysts were also prepared by a conventional impregnation method using water as a solvent. The impregnation procedure consists of dissolving the aforementioned amount of Ni(NO<sub>3</sub>)<sub>2</sub>·6H<sub>2</sub>O and Cu(NO<sub>3</sub>)<sub>2</sub>·3H<sub>2</sub>O in 10 mL of deionized water and added the solution to the beaker containing 0.5 g of SBA-15. The mixture was stirred overnight and then dried in an ambient pressure at 80 °C for 12 h. After that, the sample was calcined at 550 °C for 6 h in air and reduced at 500 °C for 4 h in 5 % H<sub>2</sub>/Ar. The obtained sample was denoted as Ni-Cu/SBA-15(IM).

### 1.2.3.2 Characterization

Phase identity and crystallinity of the samples were assessed by X-ray diffraction (XRD) using an X-ray diffractometer (D8 ADVANCE, Bruker, Ltd., Germany). The radiation source was Cu K $\alpha$  and

the measurement was operated at 40 kV and 40 mA over a  $2\theta$  range of  $15^\circ - 80^\circ$  with a step of  $0.02^\circ \text{ s}^{-1}$  and 0.5 s per step. The size, morphology, and elemental composition of the catalyst particles were examined by transmission electron microscopy (TEM) equipped with an energy dispersive spectrometer (EDS), which was operated at 200 kV (JEOL JEM-2100Plus).

The specific surface area as well as details on pore volume and diameter of the samples was measured by a  $\text{N}_2$  sorption technique (Nova 2000e, Quantachrome Instruments) at  $-196^\circ \text{C}$ . Prior to the measurements, the samples underwent a degas process at  $150^\circ \text{C}$  for 3 h under vacuum. The calculation for the specific surface area was done using the Brunauer-Emmett-Teller (BET) method. Pore size distribution was determined using the Barrett-Joyner-Halenda (BJH) method from the desorption branch. The reduction temperature profiles as well as the catalyst reduction process prior to experiments were obtained by the hydrogen temperature-programmed reduction ( $\text{H}_2$ -TPR) method in a CHEMBET-Pulsar (Quantachrome Instruments). The sample amount of 150 mg was pretreated at  $120^\circ \text{C}$  for 0.5 h in a He flow. The reduction was performed in a range of  $50\text{--}500^\circ \text{C}$  ( $10^\circ \text{C min}^{-1}$ ) in a  $\text{H}_2/\text{Ar}$  flow (5 vol%) at  $30 \text{ cm}^3 \text{ min}^{-1}$ .

The information on the local structure, geometry, and oxidation state during the reduction process was obtained by an X-ray absorption near edge structure (XANES) analysis at Cu K-edge (8979 eV) and Ni K-edge (8333 eV) at the XAS Beamline (BL-5.2) of the Synchrotron Light Research Institute (Public Organization), Thailand, employing a double monochromator. A pressed thin pellet of sample was used in the experiment and inserted in the *in situ* XAS cell [37]. The measurement was performed starting at room temperature under a  $\text{N}_2$  flow ( $20 \text{ cm}^3 \text{ min}^{-1}$ ) and then heated to  $500^\circ \text{C}$  at a rate of  $2^\circ \text{C min}^{-1}$  in a  $\text{H}_2/\text{N}_2$  flow (33 vol%). Afterward, the cooling process was conducted in a  $\text{N}_2$  atmosphere. The data were collected in transmission mode at varying temperatures during the heating and cooling cycles. Bulk Cu foil,  $\text{Cu}_2\text{O}$ , CuO,  $\text{Cu}(\text{NO}_3)_2$ , Ni foil, and NiO were used as reference compounds. The linear combination fitting (LCF) and EXAFS curve fitting were done on the Athena and EXAFSPAK programs, respectively [38, 39]. Metal leaching into the reaction solution was quantified by inductively coupled plasma–atomic emission spectroscopy (ICP-AES, VISTA-MPX).

### 1.2.3.3 Catalytic Evaluation

Activity testing was conducted in a 120 mL stainless steel reactor. 59.4  $\mu\text{L}$  Methyl levulinate (Sigma-Aldrich Chemical Co.), 24 mL of 2-propanol (Fisher Scientific UK), and 0.1 g of the catalyst were used in each catalytic run and the mixture was stirred at 300 rpm. The reactor was purged 5 times with  $\text{N}_2$  before the reaction tests, otherwise stated. In general, the reactor pressure varies from 0 to 18 bar during the reaction. The product mixture was collected in an ice cold trap and analysed by gas chromatography (GC-2010, Shimadzu) with a flame ionization detector at  $300^\circ \text{C}$  using DB-WAX (30 m in length, 0.25 mm i.d., and 0.25  $\mu\text{m}$  film thickness) with the oven temperature ramping from  $50 - 210^\circ \text{C}$ . The results were further confirmed by GC-MS at detector temperature of  $400^\circ \text{C}$  (QP-5050, Shimadzu). The methyl levulinate conversion and the GVL product selectivity and yield were calculated using the following equations:

$$\text{Conversion (\%)} = \left( \frac{\text{mole of consumed ML}}{\text{mole of initial ML}} \right) \times 100 \quad (1)$$

$$\text{Selectivity (\%)} = \left( \frac{\text{mole of produced GVL}}{\text{mole of consumed ML}} \right) \times 100 \quad (2)$$

$$\text{Yield (\%)} = \left( \frac{\text{Conversion of ML} \times \text{Selectivity of GVL}}{100} \right) \quad (3)$$

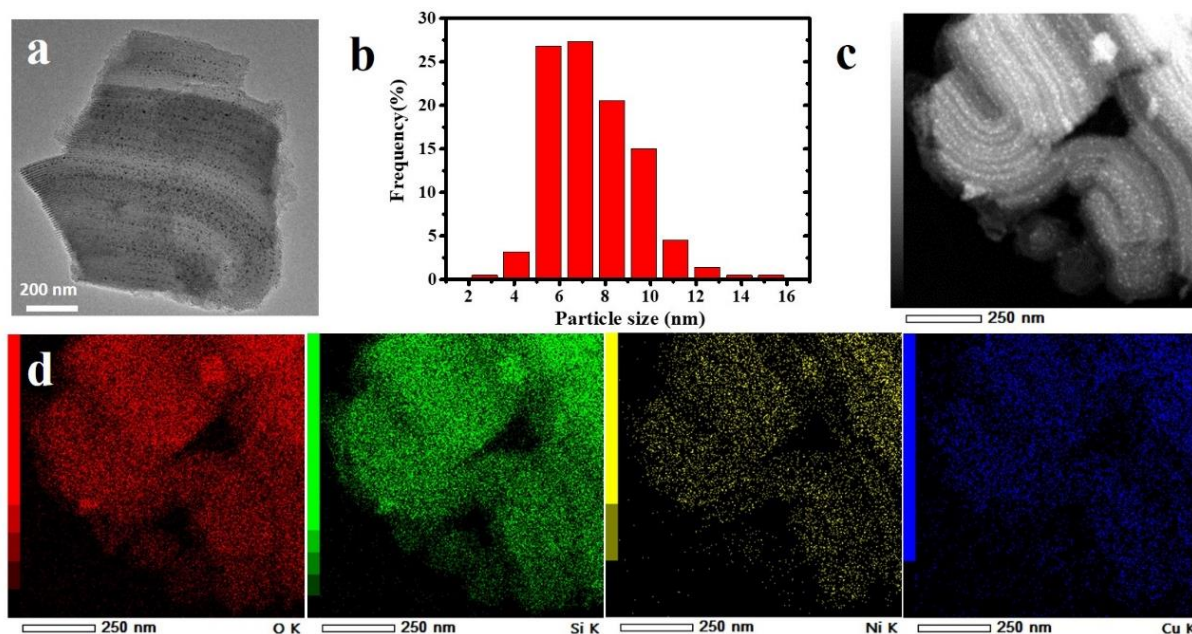
The numbers of mole of ML and GVL were obtained from the peak area analysis using GC-FID.

### 1.2.3.4 Results and Discussion

**Table 3-1** Comparative catalytic properties of Ni-Cu/SBA-15(IM), Ni-Cu/SBA-15(EG), their monometallic catalysts with the previously reported CNHs supported catalyst.

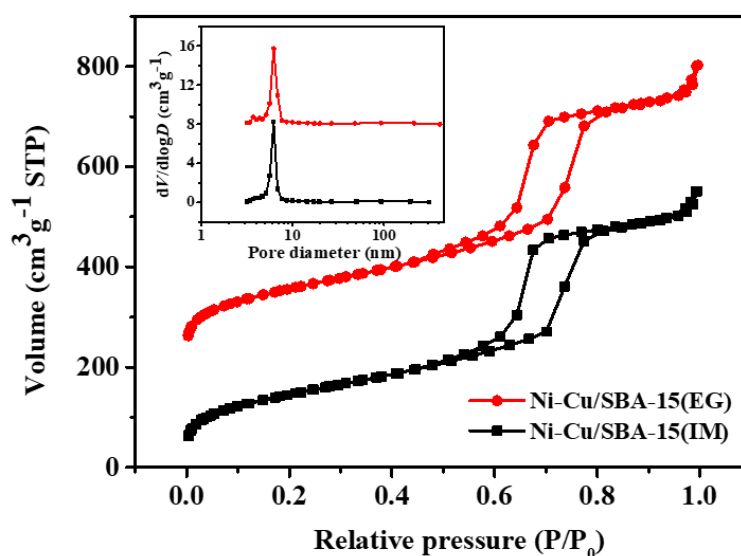
| Catalysts        | ML/EL/LA<br>Conversion<br>(%) | GVL<br>Selectivity<br>(%) | GVL<br>Yield (%) | Reaction<br>temperature<br>(°C) | Reaction<br>time (h) | Reference        |
|------------------|-------------------------------|---------------------------|------------------|---------------------------------|----------------------|------------------|
| Ni-Cu/SBA-15(IM) | 91.1                          | 82.9                      | 75.6             | 170                             | 3                    | This work        |
| Ni-Cu/SBA-15(EG) | 94.2                          | 92.7                      | 87.3             | 170                             | 3                    | This work        |
| Ni/SBA-15(EG)    | 94.4                          | 90.4                      | 85.4             | 170                             | 3                    | This work        |
| Cu/SBA-15(EG)    | 87.0                          | 90.6                      | 78.8             | 170                             | 3                    | This work        |
| Ni-Cu/SBA-15(EG) | 91.3                          | 89.7                      | 81.9             | 140                             | 3                    | This work        |
| red-oxd-Ni/CNHs  | 96.2                          | 93.0                      | 89.4             | 200                             | 3                    | Previous<br>work |

It could be obviously observed in Table 3-3 that the Ni-Cu/SBA-15(EG) requires lower reaction temperature as well as shorter reaction time to provide comparable catalytic behaviours as other previously reported catalysts for GVL production. It could also see that the Cu/SBA-15(EG), Ni/SAB-15(EG), and Ni-Cu/SAB-15(EG) showed slight difference in catalytic properties. Both Ni/SAB-15(EG), and Ni-Cu/SAB-15(EG) showed higher ML conversion than Cu/SBA-15(EG) while Ni-Cu/SAB-15(EG) seemed to be the most selective catalyst for GVL production. This could imply that Cu, Ni, and Ni-Cu could act as active centers for ML conversion but the presence of Ni is more preferable. On the other hand the presence of Cu could enhance the GVL selectivity in the Ni-Cu/SAB-15(EG). Considering the red-oxd-Ni/CNHs catalyst, it could be clearly observed that this catalyst provided comparable activity and selectivity with the Ni-Cu/SAB-15(EG) catalyst. However, it requires the temperature up to 200 °C which is higher than that of the SBA-15 supported catalysts (170 °C). This results could suggest that SBA-15 might be slightly more active than the CNHs during its use as a support in GVL production.



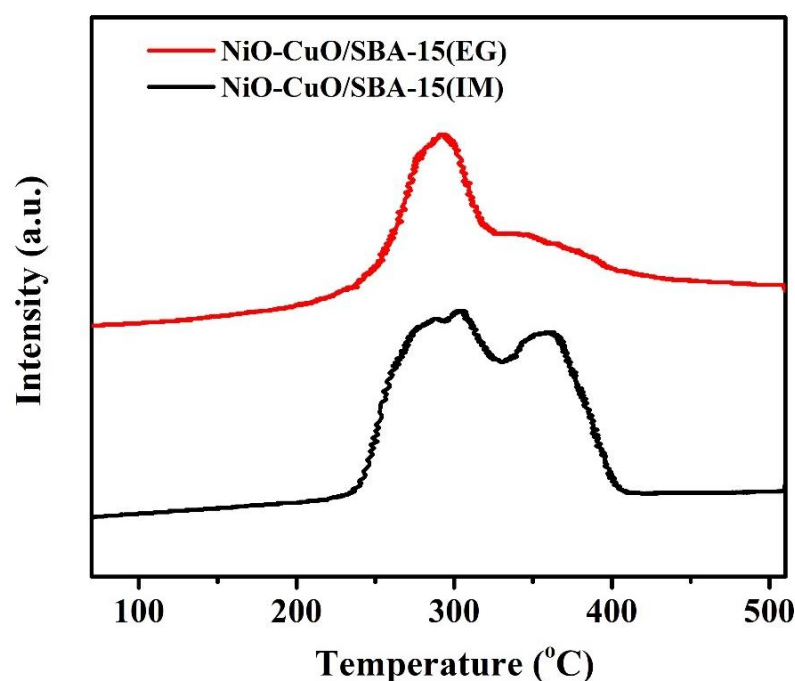
**Figure 3-1. (a) TEM image, (b) metal particle size distribution, (c) HAADF-STEM image and (d) elemental mapping of the Ni-Cu/SBA-15(EG).**

Fig. 3-1a shows the TEM image of the Ni-Cu/SBA-15(EG) catalyst and homogenous dispersion of nanoparticles can be clearly observed. Particularly, small nanoparticles uniformly distributed in the mesoporous channels and are isolated from each other. Fig. 2b shows the metal particle size distribution of the Ni-Cu/SBA-15(EG) catalyst. The particles on SBA-15 are in the range of 2-16 nm with the average particle size of 7 nm. The high-angle annular dark field-scanning transmission electron microscopy (HAADF-STEM) image (Fig. 2c) demonstrates highly ordered arrays of nanoparticles located in the long-range ordered mesoporous silica. The corresponding elemental mapping images for the different elements in this selected area are presented in Fig. 2d, which exhibits the homogenous dispersion of nanoparticles on the silica matrix. Moreover, the mapping shapes of Ni and Cu elements are following the tunnel arrays of SBA-15, implying that both metals were located inside the mesoporous channels. The strong association of Ni and Cu species in the X-ray images suggested the formation of NiCu alloy structures.



**Figure 3-2. N<sub>2</sub> adsorption-desorption isotherms and pore size distributions (inset) of the catalysts.**

N<sub>2</sub> adsorption-desorption was performed to evaluate the texture and porosity of the catalysts, and the results are shown in Fig. 3-2. The N<sub>2</sub> adsorption-desorption isotherms of both catalyst samples reveal a typical type IV(a) curve with type H1 hysteresis loops, a characteristic feature of a mesoporous material with uniform porosity according to the IUPAC definition. In the inset of Fig. 4, the pore size distribution of both catalysts show a sharp peak at around 6 nm, corresponding to the internal cavity of SBA-15. Additionally, the Ni-Cu/SBA-15(EG) shows a multi-modal pore distribution in the range of 3-8 nm originates from the presence of metal nanoparticles inside the mesoporous channels. By deriving the N<sub>2</sub> adsorption-desorption isotherms, the pore structural parameters are given in Table 1 and the information of SBA-15 is shown as a reference. The calculated BET surface areas and pore volumes of the Ni-Cu/SBA-15(EG) and Ni-Cu/SBA-15(IM) catalysts are 559 m<sup>2</sup> g<sup>-1</sup>, 520 m<sup>2</sup> g<sup>-1</sup> and 0.89 cm<sup>3</sup> g<sup>-1</sup>, 0.81 cm<sup>3</sup> g<sup>-1</sup>, respectively. The surface area and pore volume of both Ni-Cu/SBA-15(EG) and Ni-Cu/SBA-15(IM) are smaller than those of SBA-15 (724 m<sup>2</sup> g<sup>-1</sup> and 0.96 cm<sup>3</sup> g<sup>-1</sup>). The results suggest that metal nanoparticles could fill in or block the pores of SBA-15, resulting in the reduction of the surface area and pore volume. Furthermore, the Ni-Cu/SBA-15(EG) presents larger specific surface area and pore volume than those of Ni-Cu/SBA-15(IM), which can be arise from the better dispersion of nanoparticles.



**Figure 3-3. H<sub>2</sub>-TPR profiles of catalysts**

The H<sub>2</sub>-TPR profiles (Fig. 3-3) show the reduction behaviors of these two catalysts. Previous studies have demonstrated that the reduction of bulk CuO generally occurs below 300 °C and the reduction peaks of NiO on silica take place above 370 °C. It was also reported that the presence of Ni and Cu lowers the reduction temperature of their corresponding oxides. The XRD result of NiO-CuO/SBA-15(IM) shows the presence of CuO and Ni<sub>0.75</sub>Cu<sub>0.25</sub>O phases. The reduction curves of NiO-CuO/SBA-15(IM) possesses three peaks. The peaks located at 286 °C and 304 °C can be assigned to the reduction of CuO and Ni<sub>0.75</sub>Cu<sub>0.25</sub>O species having a weak or negligible interaction with the silica. The third H<sub>2</sub> consumption peak centered at 357 °C is ascribable to the reduction of Ni<sub>0.75</sub>Cu<sub>0.25</sub>O which strongly interact with the silica. The observed shift of reduction peaks to lower temperature can be describable to formation of Ni<sub>x</sub>Cu<sub>1-x</sub>O solid solution. Next, the reduction profile of NiO-CuO/SBA-15(EG) is

composed of one reduction peak situated at 290 °C with a weak shoulder peak centered at 335 °C, corresponding to the reduction of the well dispersed  $\text{Ni}_x\text{Cu}_{1-x}\text{O}$  species which have weak and enhanced interaction, respectively. In  $\text{H}_2$ -TPR, the area of the reduction peak, corresponding to the consumption of  $\text{H}_2$ , directly reveals the amount of the reducible species. The area of the reduction peak of NiO-CuO/SBA-15(IM) is larger than that of NiO-CuO/SBA-15(EG), implying more surface reducible oxides on NiO-CuO/SBA-15(IM).

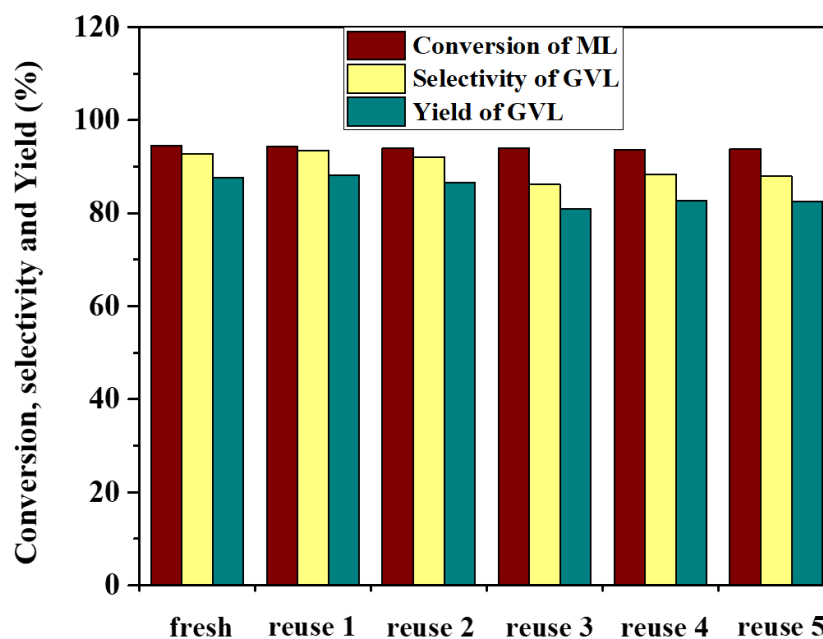


**Figure 3-4 Reusability of Ni-Cu/SBA-15(EG) catalyst. Reaction conditions: catalyst, 0.1 g; 2-propanol 24 mL; methyl levulinate/2-propanol = 0.02 mol/L; reaction temperature, 170 °C; reaction time, 3 h.**

The reusability of Ni-Cu/SBA-15(EG) catalyst was also studied in view of its excellent performance in the CTH reaction, and the results are shown in Fig. 3-4. The spent catalyst was separated from the product by centrifugation and then used for the next run without further activation. ML conversion around 94 % was achieved in all the runs. Moreover, Ni-Cu/SBA-15(EG) exhibited very stable selectivity and yield of GVL in the first 3 cycles and declined slightly in the next 3 runs. GVL yield can be maintained at 82.5 % even in the 6<sup>th</sup> run. The data shows that the Ni-Cu/SBA-15(EG) catalyst did not suffer from severe deactivation under the relatively harsh conditions, demonstrating great stability during the hydrogenation process. During the catalytic transfer hydrogenation of ML, two-dimensional hexagonal mesoporous channels restricted the diffusion of the metal nanoparticles in the channel, repressing the agglomeration as well as leaching of metal nanoparticles into the reaction solution. This could be the possible reason that the Ni-Cu/SBA-15(EG) catalyst exhibited excellent stability during the hydrogenation process.

### 1.2.3.5 Conclusion

In summary, our work presents a practical glycol-assisted impregnation method for the synthesis of well dispersed Ni-Cu nanoparticles on SBA-15. A highly efficient Ni-Cu/SBA-15(EG) catalyst was successfully prepared and found to exhibit much better catalytic activity in the CTH reaction by using 2-propanol as the H-donor at 140-170 °C than the Ni-Cu/SBA-15 synthesized by conventional aqueous impregnation method, providing higher ML conversion of 91.3 % with greater GVL selectivity of 89.7 % at 140 °C for 3 h. The presence of copper could provide higher selectivity towards GVL

product. Characterization of the catalysts showed that small particle size, high homogeneity in metal composition, and even distribution of the metal nanoparticles on the mesoporous substrate were responsible for the high reactivity of the Ni-Cu/SBA-15(EG) catalyst. Our catalyst retained fairly high reaction efficiency during the recycling test and can be reused at least 5 times without drastic loss in catalytic activity and yield towards GVL formation. The excellent stability could be ascribed to the restricted diffusion of the metal nanoparticles in the channel, repressed agglomeration as well as leaching of metal nanoparticles into the reaction solution. Therefore, the developed Ni-Cu/SBA-15 catalyst is a promising candidate for selective hydrogenation of ML to GVL under mild conditions without using external H<sub>2</sub>. Moreover, the catalysts prepared in this work show similar catalytic performance with that of the red-oxd-Ni/CNHs catalysts at low reaction temperature.

#### 1.2.4 Reaction mechanism study of GVL production over non-supported Ni-Cu catalysts

As it could be observed from the results displayed above about SBA-15 supported catalysts and the previously reported CNHs supported nickel catalysts that both carbon and non-carbon based materials shows great potential as supports for nickel in GVL production. Moreover, the addition of second element, copper could enhance GVL selectivity. Therefore, an investigation of metal active sites without any support materials was conducted for GVL reaction mechanism study. Besides copper, cobalt chromium, and iron were selected to elucidate their roles in assisting GVL production of nickel catalysts.

##### 1.2.4.1 Catalyst Preparation

All metal nitrate salts were purchased from Ajax Finchem Pty Ltd. with minimum purity of 98%. Metal oxide and their Cu-based mixed metal oxides were simply prepared by thermal decomposition of metal nitrate salts. For metal oxide preparation, a chosen nitrate salt of 0.042 mole of each metal was dissolved in 10 ml of DI water. While a mixture of 0.021:0.021 mole ratio of  $Cu(NO_3)_2 \cdot 3H_2O$  and one of the other metal (Ni, Co, Cr, or Fe) nitrate was selected for Cu-base mixed metal oxide preparation. After dissolution of metal salts in DI water, the sample was dried and calcined at 800 °C for 5 h in air and collected after cooling down at room temperature.

##### 1.2.4.2 Characterization

Powder X-ray diffraction (XRD) patterns of samples from both conventional and *in situ* experiments were analyzed by an X-ray diffractometer (D8 ADVANCE, Bruker, Ltd., Germany) using Cu K<sub>α</sub> radiation at 40 kV and 40 mA over the 2θ range of 10 < 2θ < 80 degree. For the *in situ* experiment, the sample was heated with a heating rate of 12 °C /min under hydrogen atmosphere (99.99%) at the flow rate of 20 ml/min from room temperature to 600 °C on a Rh-Pt alloy substrate. Hydrogen temperature programmed reduction (H<sub>2</sub>-TPR) was carried out using CHEMBET-Pulsar Quantachrome Instruments (Germany) equipped with a thermal conductivity detector (TCD). The catalyst (20 mg) was reduced in 5 vol% H<sub>2</sub> in argon at a flow rate of 30 ml/min with a heating rate of 10 °C /min from room temperature to 800 °C. X-ray photoelectron spectroscopy (XPS) was conducted using PHI 5000 Versaprobe II (ULVAC-PHI, Inc., Japan). The obtained data was fitted and interpreted using XPSPEAK4.1 program.

### 1.2.4.3 Catalytic Evaluation

All catalytic transfer hydrogenation reactions were carried out in a 130 ml stainless steel autoclave with a magnetic stirrer (500 rpm). 0.58 ml of methyl levulinate (ML), 24 ml of alcohol, and 1 g of a metal oxide or mixed metal oxide catalyst were loaded in an autoclave and heated up to 200 °C with heating rate of 5 °C /min. A liquid sample analyzed by gas chromatograph using a flame ionization detector or GC-FID (GC-2010, Shimadzu, Japan) and a mass spectrometry detector or GC-MS (GCMS-QP2020, Shimadzu, Japan), and a capillary column (DB-WAX, Agilent technologies, USA) with 30 m in length, 0.25 mm inner diameter, and 0.25 µm film thickness). The methyl levulinate conversion and the GVL product yield were calculated using the following equations:

$$\text{Conversion (\%)} = \left( \frac{\text{mole of consumed ML}}{\text{mole of initial ML}} \right) \times 100 \quad (1)$$

$$\text{Yield (\%)} = \left( \frac{\text{mole of produced GVL}}{\text{theoretical mole of GVL}} \right) \times 100 \quad (2)$$

The numbers of mole of ML and GVL were obtained from the peak area analysis using GC-FID while other by-products were detected by GC-MS. Hydrogen content remaining in the reaction was calculated according to the ideal gas law. In brief, the final pressure was recorded after the reactor was cooled down to room temperature. The value of remaining pressure in atm was then subjected to equation (3).

$$n = \frac{PV}{RT} \quad (3)$$

where V = 0.1 L (actual volume of the reactor), R = 0.08206 L.atm/(mol.K) and T = 298.15 K. The gas was later analyzed using micro-GC for acquiring purity of hydrogen (CP 4900, Agilent Technologies, USA) and multiplied with the calculated total mole number of remaining gas.

### 1.2.4.4 Results and Discussion

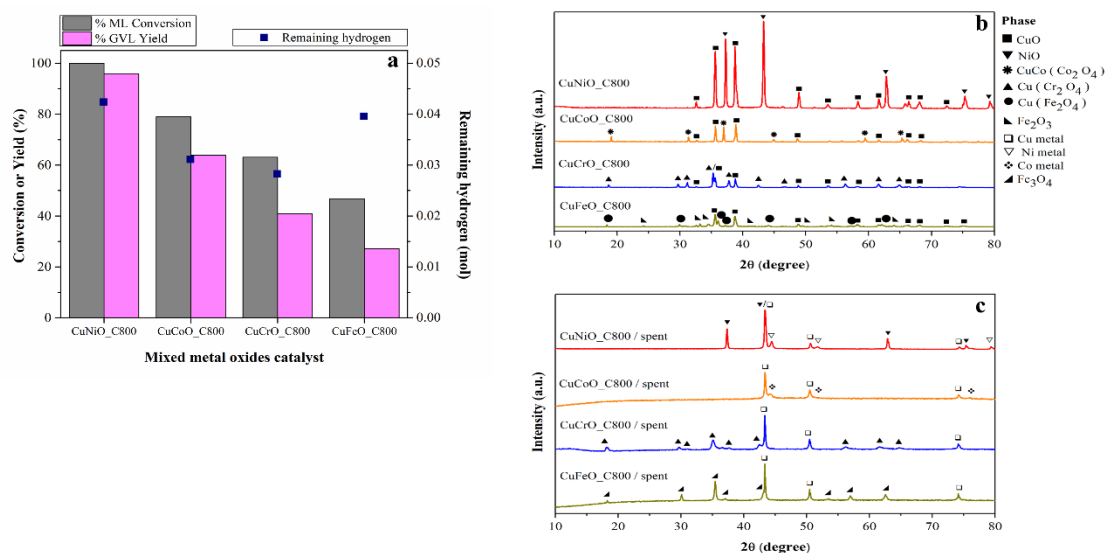


**Figure 4-1 (a) Catalytic performance in terms of ML conversion, GVL yield, and hydrogen production of copper mixed oxide catalysts at 200 °C for 3 h using 0.2 M ML in 24 ml of 2-PrOH, (b) XRD patterns of (a) fresh catalysts and (c) spent catalysts.**

Single phase metal oxides and mixed metal oxides catalysts were compared for GVL production from ML. Initially, five single phase metal oxides including CuO, NiO, Co<sub>3</sub>O<sub>4</sub>, Cr<sub>2</sub>O<sub>3</sub>, and Fe<sub>2</sub>O<sub>3</sub> were tested as catalysts for production of gamma-valerolactone (GVL) from methyl levulinate (ML) by catalytic transfer hydrogenation (CTH) in a 2-propanol (2-PrOH) system. Catalytic evaluation results of these metal oxides showed neither catalytic behavior toward 2-propanol dehydrogenation nor GVL production at 200 °C during the reaction period of 3 h. These results were supported by unchanged reaction pressures caused by 2-propanol evaporation and undetectable or negligible hydrogen gas, acetone, methanol, or GVL throughout the course of the reactions. Consecutively, the four Cu-based mixed oxides were employed as catalysts giving catalytic results provided in Fig. 4-1a. CuNiO showed high catalytic property. The order of catalytic performance in terms of ML conversion and GVL yield is as follows; CuNiO > CuCoO > CuCrO > CuFeO. The formation of H<sub>2</sub> was labelled as amount of remaining hydrogen. For the CuNiO catalyst, it was quite obvious that both 2-PrOH dehydrogenation and ML hydrogenation could take place effectively. CuCoO and CuCrO also showed similar behavior to CuNiO but with less catalytic activity. On the other hand, CuFeO did not show high ML conversion but gave almost the same amount of remaining H<sub>2</sub> as that of CuNiO. This indicated that CuFeO catalyst tended to be an active catalyst for 2-PrOH dehydrogenation but was not effective for ML hydrogenation. XRD patterns of the catalysts before and after the reaction. It could be seen that CuO was completely reduced to Cu metal while NiO was partially reduced to Ni metal after the reaction. The presence of Ni/NiO phase with the presence of Cu metal could provide efficient GVL production. The XRD pattern of CuCoO\_800 showed complete reduction of both CuO to metallic Cu and Co<sub>3</sub>O<sub>4</sub> to metallic Co, respectively. The conversion of ML over this catalyst was around 80%. The CuCrO catalyst showed moderate catalytic activity for both 2-PrOH dehydrogenation and ML conversion. The XRD pattern after reaction of CuCrO catalyst represented in Fig. 4-1c showed 2 phases of Cu metal and CuCr<sub>2</sub>O<sub>4</sub>. CuFeO catalyst did not show high activity towards GVL production but provided large amount of hydrogen gas. Hence, the synergy of various oxidation states (Cu<sup>0</sup>, Fe<sup>2+</sup>, Fe<sup>3+</sup> and O<sup>2-</sup>) in Cu and Fe<sub>3</sub>O<sub>4</sub> system during the dehydrogenation process should be responsible for its good H<sub>2</sub> production.

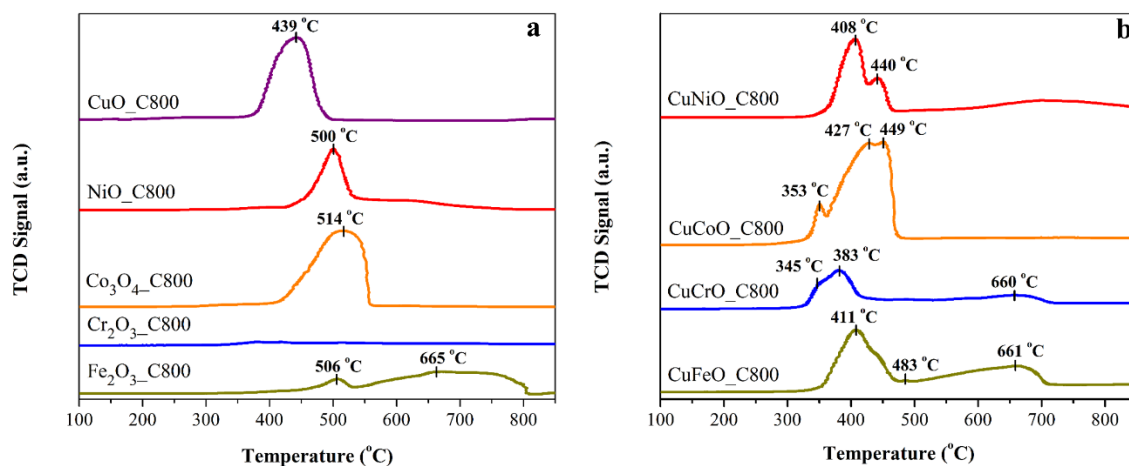


**Figure 4-2 H<sub>2</sub>-TPR profiles of (a) single phase metal oxide (b) mixed metal oxides catalysts.**

To further elucidate the reduction behaviors associated with the catalytic performance of the Cu-based mixed oxide catalysts and their host metal oxides. The hydrogen temperature programmed reduction (H<sub>2</sub>-TPR) was conducted and the results were shown in Fig. 4-2. CuO catalyst showed a large bell peak at 439 °C representing a complete reduction from Cu<sup>2+</sup> to Cu<sup>0</sup>. NiO catalyst showed a major reduction peak at 500 °C suggesting a reduction of Ni<sup>2+</sup> to Ni<sup>0</sup>. In addition, an appearance of a low intensity flat curve at around 620 °C could be related to a difficultly reduced species of high crystalline NiO. Co<sub>3</sub>O<sub>4</sub> catalyst showed only one broadly asymmetric reduction peak at 514 °C. Fe<sub>2</sub>O<sub>3</sub> catalyst was reduced at two different temperatures of 506 and 665 °C. There was a small peak observed at around 380 °C in Cr<sub>2</sub>O<sub>3</sub> catalyst which could be attributed to the reduction of small portion of Cr<sup>6+</sup> presented in Cr<sub>2</sub>O<sub>3</sub> to Cr<sup>3+</sup>. Moreover, it was clear that all five single phase metal oxides catalysts prepared in this work showed smaller degree of reduction or appeared at higher reduction temperature compared to the similar metal oxides synthesized at lower calcination temperatures in other reports. The inferior reduction behavior of all metal oxides which resulted in a lack of their active metallic sites lead to their poor catalytic performance towards GVL production. Further investigation in the H<sub>2</sub>-TPR study of the copper mixed oxide catalysts indicated that each catalyst had at least two reduction peaks as shown in Fig. 2b. The CuNiO catalyst showed two main reduction peaks at 408 and 440 °C with a very broadly flat curve at around 700 °C. As it could be observed in the corresponding XRD pattern (Fig. 4-1b), two phases of CuO and NiO were presented in the CuNiO catalyst. The first reduction peak belonged to the reduction of CuO to metallic copper (Cu<sup>0</sup>) while the second peak was assigned to the reduction of NiO to metallic nickel (Ni<sup>0</sup>). CuCoO showed three reduction peaks at 353, 427, and 449 °C. Based on the XRD pattern of CuCoO catalyst shown in Fig. 1b, this catalyst had two major phases of CuO and CuCo(Co<sub>2</sub>O<sub>4</sub>) spinel. Therefore, the first small peak at the lowest temperature should be assigned to the easily reduced CuO phase while the peak at 427 °C should correspond to the reduction of Cu<sup>2+</sup> to Cu<sup>0</sup> and Co<sup>3+</sup> to Co<sup>2+</sup> in the spinel structure. The highest reduction peak at 449 °C belonged to the reduction of Co<sup>2+</sup> to metallic Co. Interestingly, XRD pattern of CuCrO showed two different phases of CuO and Cu(Cr<sub>2</sub>O<sub>4</sub>) spinel without the presence of Cr<sub>2</sub>O<sub>3</sub> phase. This meant that the formation of copper oxide and chromium oxide could alter the oxidation states of chromium. In addition, TPR profile of CuCrO displayed two overlapped peaks at 345 and 383 °C as well as another broad peak at 660 °C. The first peak at 345 °C was attributed to the reduction of Cu<sup>2+</sup> in CuO to Cu<sup>0</sup>. The second peak at 383 °C was a reduction of Cu<sup>2+</sup> in the Cu(Cr<sub>2</sub>O<sub>4</sub>) spinel to Cu<sup>0</sup> and the last peak at 660 °C was attributed to the reduction of Cr<sup>3+</sup> in Cu(Cr<sub>2</sub>O<sub>4</sub>) spinel to Cr<sup>2+</sup>. Lastly, CuFeO also showed three

reduction peaks at 411, 483, and 661 °C while its XRD pattern in Fig. 1b showed three phases of CuO, Cu(Fe<sub>2</sub>O<sub>4</sub>) and Fe<sub>2</sub>O<sub>3</sub>. The first peak at 411 °C indicated the reduction of Cu<sup>2+</sup> in CuO to Cu<sup>0</sup>. A shoulder appeared at around 450 °C could be assigned to the reduction of Fe<sup>3+</sup> in Fe<sub>2</sub>O<sub>3</sub> to Fe<sup>2+</sup> in a spinel Fe<sub>3</sub>O<sub>4</sub>. A very small peak shown at 483 °C could represent the reduction of Cu<sup>2+</sup> in Cu(Fe<sub>2</sub>O<sub>4</sub>). Finally, the broad asymmetric peak at 661 °C could both be attributed to the partial reduction of Fe<sup>3+</sup> in Cu(Fe<sub>2</sub>O<sub>4</sub>) to Fe<sup>2+</sup> in (CuFe)(Fe<sub>2</sub>O<sub>4</sub>) spinel and the complete reduction from Fe<sup>3+</sup> in both rhombohedral and spinel structures to FeO and/or Fe<sup>0</sup>. In brief, the CuNiO was composed of two separated phases of CuO and NiO; however, the reduction temperature of both CuO and NiO were lower than their host metal oxides. On the other hand, the addition of copper oxide to the cobalt oxide (CuCoO) created the new phase of CuCo(Co<sub>2</sub>O<sub>4</sub>) spinel structure while maintaining the CuO phase but without the presence of pure the Co<sub>3</sub>O<sub>4</sub> phase. The reduction profile of CuCoO indicated that CuO could be reduced at low temperature. The formation of copper oxide and chromium oxide created the more reducible phase of Cu(Cr<sub>2</sub>O<sub>4</sub>). Finally, the formation of copper and iron mixed metal oxides (CuFeO) could create the new CuFe<sub>2</sub>O<sub>4</sub> phase but still maintained their host metal oxides of CuO and Fe<sub>2</sub>O<sub>3</sub>. All reductions of Cu<sup>2+</sup> and Fe<sup>3+</sup> were shifted to lower temperatures. In all cases, the reducibility of metal ions were improved after the mixed oxide formation with copper oxide. The alteration of catalyst redox behaviors was strongly related to the enhanced catalytic performance.

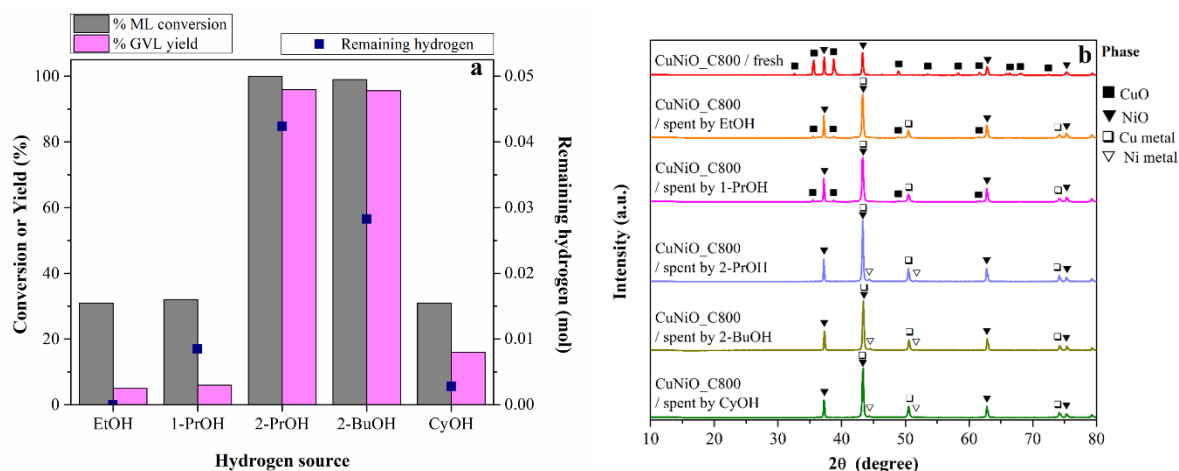


**Figure 4-3 (a) Catalytic performance in terms of ML conversion, GVL yield, and hydrogen production of CuNiO catalyst at 200 °C for 3 h using 0.2 M ML in 24 ml of various alcohols and (b) XRD patterns of fresh and spent CuNiO catalyst after the reaction.**

With the consistent results among XRD, H<sub>2</sub>-TPR, and catalytic performance evaluation, it could be confirmed that CuNiO was the most effective catalyst for GVL production from ML. Subsequently, various alcohols including aliphatic primary alcohols (ethanol, EtOH and 1-propanol, 1-PrOH), aliphatic secondary alcohols (2-propanol, 2-PrOH and 2-butanol, 2-BuOH), and a cyclic secondary alcohol (cyclohexanol, CyOH) were selected for catalytic testing to verify effect of alcohol types on GVL production over the CuNiO catalyst. Catalytic results presented in Fig. 3a showed that the secondary alcohols were more suitable than primary alcohols in this reaction. EtOH and 1-PrOH gave about 30% of ML conversion and less than 10% of GVL yield. Formation of a stronger bond between the catalyst active sites and alkoxide species generated from the primary alcohol compared to that of the secondary alcohol could support the ineffectiveness of the primary alcohols.<sup>30</sup> On the other hand, the aliphatic secondary alcohols (2-PrOH and 2-BuOH) showed drastically better catalytic activity than the cyclic secondary alcohol (CyOH). This was due to a high adsorption tendency of CyOH over the catalyst surface. In addition, its high viscosity could also affect ML dispersion in the solution which lowered

ML conversion. A very low amount of H<sub>2</sub> generated after reaction as shown in Fig. 4-3 indicated that CyOH has low tendency for hydrogen production. Both 2-PrOH and 2-BuOH provided high ML conversion and more than 95% of GVL yield. In addition, the highest remaining hydrogen amount was obtained in the 2-PrOH system. As mentioned above, generated hydrogen species from alcohol could perform as a reducing agent for the activation of metal oxide catalyst to generate metal active sites. Phase alteration of CuNiO catalyst after reactions in various alcohols was determined by XRD technique as shown in Fig. 4-3b. In the primary alcohol system, Cu metal phase was formed with the presence of CuO and NiO. Aliphatic secondary alcohols; on the other hand, showed higher degree of catalyst reduction where metallic nickel was also observed. Surprisingly, although low ML conversion, low GVL yield, and low H<sub>2</sub> production were observed in CyOH system (Fig. 3a) both metallic Cu and Ni were generated after the reaction. This means that the CyOH could reduce CuNiO catalyst. However, its strong adsorption on the catalyst as well as its high viscosity could be the reasons for its ineffective role in GVL production.

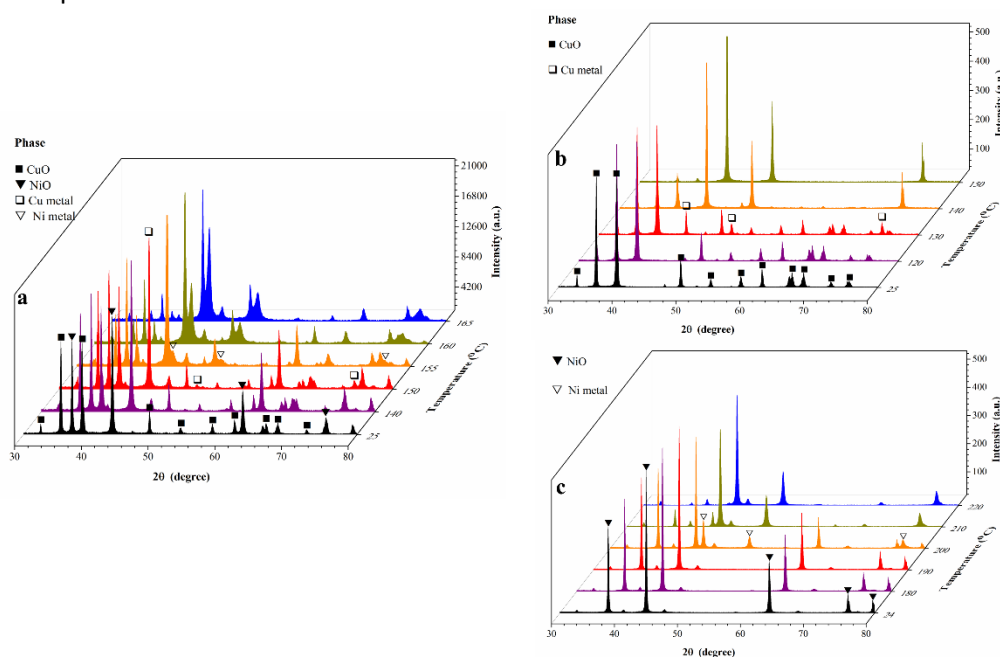


**Figure 4-4** *In situ* XRD patterns during reduction of (a) CuNiO, (b) CuO, and (c) NiO catalysts under pure H<sub>2</sub> gas flow of 20 ml/min.

To confirm and gain more insight information on the reducibility enhancement of CuO addition in the copper mixed oxide catalysts, the CuNiO was further selected for an *in situ* XRD reduction experiment in comparison with the CuO and NiO catalysts. Phase transformation of each catalyst was recorded while the catalyst was reduced under pure hydrogen atmosphere at elevated temperature. The *in situ* reduction of CuNiO result shown in Fig. 4a indicated that CuO was reduced to form metallic copper at around 150 °C, following by NiO reduction to form metallic nickel at around 155 °C. While the reduction profile of CuO shown in Fig. 4b indicated that Cu metal was created when the temperature reached 130 °C. The reduction behavior of NiO was displayed in Fig. 4c where Ni metal was generated at 200 °C. It can be seen that CuO phase in the CuO catalyst was reduced to Cu metal at lower temperature than CuO in CuNiO while NiO phase in the NiO catalyst was reduced at higher temperature than that of the CuNiO catalyst. The shift of CuO reduction temperature to higher

temperature (from 130 to 150 °C) and the shift of NiO reduction temperature to lower temperature (from 200 to 155 °C) was an important evidence of the complementary reduction between CuO and NiO in this catalyst. In addition, the occurrence of CuO and NiO reduction temperatures in the CuNiO catalyst at a very close values (150 and 155 °C, respectively) could support that there was a good interaction between these two oxides in the structure. In brief, the *in situ* XRD results obtained here could confirm the spillover effect of hydrogen species from the created Cu metal to its neighboring NiO for generating nickel metal active sites at lower temperature.

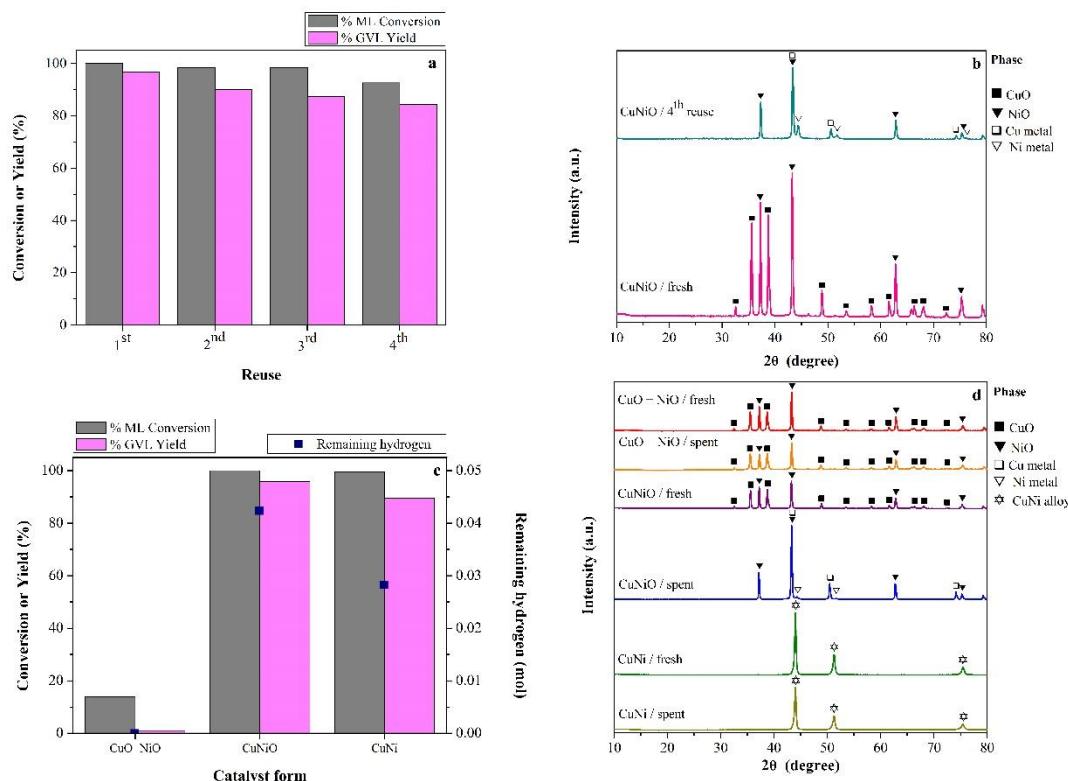


**Figure 4-5 (a) Catalytic performance of reused CuNiO catalyst up to 4 times at 200 °C for 3 h using 0.2 M ML in 24 ml of 2-PrOH, (b) XRD patterns of fresh CuNiO and after its 4<sup>th</sup> reuse, (c) catalytic**

The spent CuNiO catalyst was employed for four more times for the GVL production. The results depicted in Fig. 5a revealed that this catalyst showed only a small decrease in terms of ML conversion and GVL yield after the fourth time. The XRD patterns of the fresh and the 4<sup>th</sup> reuse of the catalyst were shown in Fig. 4-5b. It indicated that the spent catalyst still had the same three phases including Cu metal, Ni metal, and NiO as it was reported earlier in Fig. 4-2b. The small decrease of the catalytic activity might be resulted from the fact that some metallic sites became agglomerated. The number of phases existed in the CuNiO catalyst before and after the reaction led to a further challenge to find out whether the catalytic performance of the mechanically mixed CuO and NiO would be similar or different from that of the CuNiO catalyst as well as its completely reduced form (alloy). The comparative results of the three scenarios were shown in Fig. 4-5c. The mechanically mixed CuO+NiO catalyst gave 17% of ML conversion with negligible GVL production and H<sub>2</sub> production. The improvement in terms of ML conversion compared with the inactive CuO and NiO suggested that the presence of both CuO and NiO in the same system promoted the catalytic activity. The similar XRD patterns of the catalyst before and after reaction without the presence of reduced species (Cu or Ni metal) indicated that the oxide phases in the mechanically mixed metal oxide catalyst might have some capability to accelerate ML conversion; however, metallic sites were required for producing GVL (Fig. 4-5d). On the other hand, a completely reduced CuNiO labelled as CuNi\_alloy showed only one single phase of CuNi alloy. Surprisingly, this alloy catalyst showed comparable ML conversion and

GVL yield to those of the pristine CuNiO catalyst. These results suggested that the ML could be converted either on mixed metal oxides or metal/alloy active sites, however, the high selectivity of GVL product preferred the suitable ratio of metal oxides/metallic active sites. In addition, in terms of H<sub>2</sub> production, the alloy catalyst was not comparable to the CuNiO catalyst suggesting that the 2-PrOH dehydrogenation preferably took place over the mixed metal oxide catalysts. As it was described above, CuNiO showed its impressive catalytic activity in all forms namely, pristine mixed metal oxides (CuNiO), partially reduced composite (Cu + Ni/NiO), and completely reduced solid solution (CuNi alloy). This is the important proof to confirm that CuNiO was a versatile catalyst for GVL production.

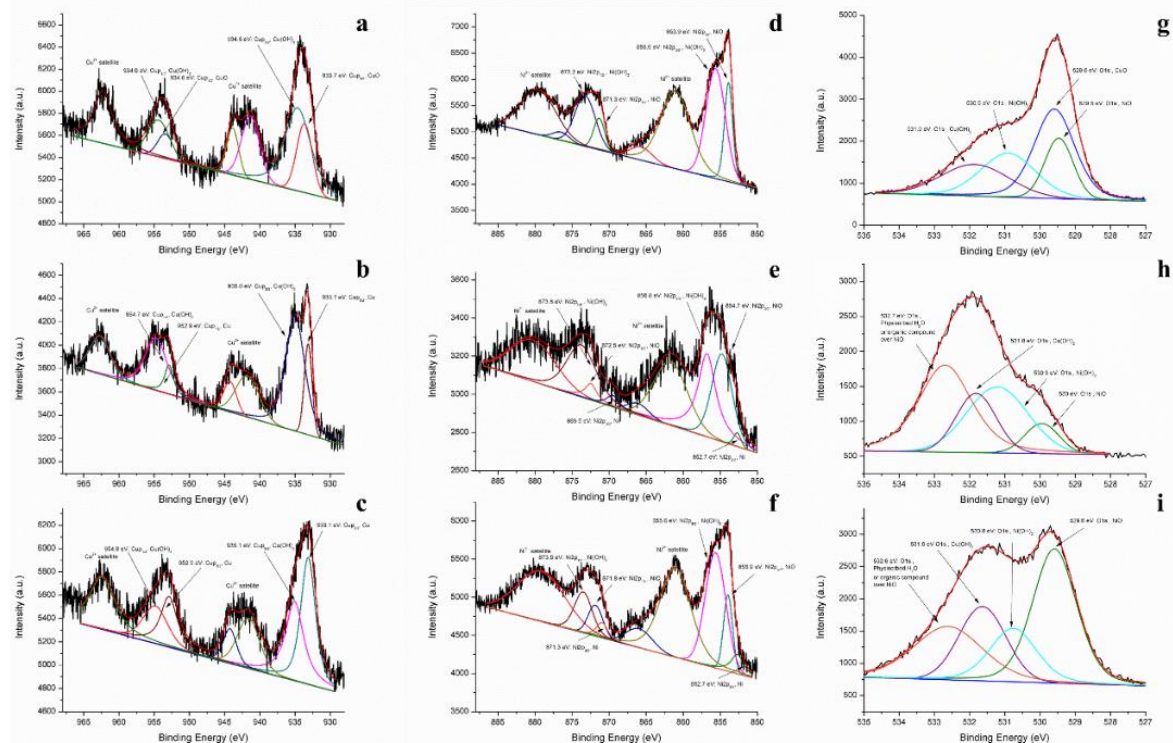
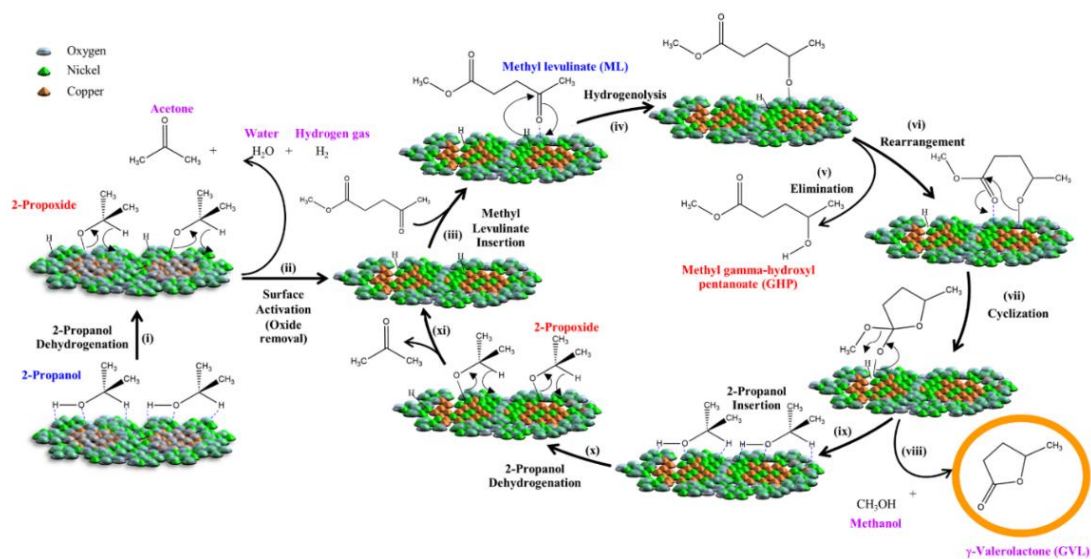


**Figure 4-6 XPS spectra of CuNiO (a, d, and g); spent CuNiO (b, e, and h); and CuNiO after 4<sup>th</sup> reuse (c, f, and i) in terms of Cu2p, Ni2p, and O1s, respectively**

To gain more understanding about good performance of the mixed metal oxide catalyst, the Cu/Ni molar ratio of 1.00 and 1.03 were observed in the pristine CuNiO and CuNi\_alloy catalysts by using XRF method, respectively (Table S4). Surface analysis results using XPS technique of the pristine CuNiO, spent CuNiO, and CuNiO after 4<sup>th</sup> reuse were compared in Fig. 6. According to the Cu2p spectra (Fig. 6a, b, c), the pristine CuNiO was originally composed of CuO and Cu(OH)<sub>2</sub>. After its first use, CuO was completely transformed to Cu metal, while the Cu(OH)<sub>2</sub> was still existed. The 4<sup>th</sup> reuse catalyst also showed these two species but with higher Cu metal/Cu(OH)<sub>2</sub> peak ratio. Ni2p spectra (Fig. 6d, e, f) also showed two species of NiO and Ni(OH)<sub>2</sub> in the pristine catalyst while the Ni metal was observed along with these two species both in the spent and 4<sup>th</sup> reuse catalysts. The O1s spectra (Fig. 6g, h, i) showed good agreement with the Cu2p and Ni2p results on their surface metal oxides and metal hydroxides formation. Additionally the high binding energy at around 532.6 – 532.7 eV in the spent catalyst and the 4<sup>th</sup> reuse samples indicated the physically adsorbed water and/or organic compounds (i.e. ML, GVL, 2-PrOH) over NiO species. This could be implied that the NiO was an important site for ML or 2-PrOH adsorption during the ML conversion to GVL. The XPS results revealed various types of surface species including Cu, Ni, CuO, NiO, Cu(OH)<sub>2</sub>, and Ni(OH)<sub>2</sub>. While the CuO was

found in the pristine catalyst but disappeared after its first use in the reaction. The role of CuO was consistent with the *in situ* XRD results stated above for facilitating NiO reduction at low temperature. The mutual presence of Cu, Ni, NiO, Cu(OH)<sub>2</sub>, and Ni(OH)<sub>2</sub> on the surface were responsible for high catalytic performance of CuNiO catalyst.



**Scheme 1 Proposed reaction mechanism**

Generally, catalytic transfer hydrogenation mechanism over heterogeneous catalysts can take place either through direct catalytic transfer (MPV) or metal hydride mechanism depending on catalyst active sites. If both Lewis acid and Brønsted basic sites are presented next to each other on the catalyst, the reaction would undergo via MPV mechanism. On the other hand, the reaction would proceed through the metal hydride mechanism if only a Lewis acid or the metal active site is presented. Therefore, in this work, it is worth proposing a reaction mechanism of ML to GVL conversion over the CuNiO catalyst to clarify its simultaneous reduction behavior and promising catalytic performance under 2-PrOH system (Scheme 1). Typically, two major steps including (1) alcohol dehydrogenation to activate surface of the catalyst and (2) hydrogenation of ML followed by simultaneous cyclization to produce GVL. In the first major step, 2-propanol was oxidized over a mixed metal oxide catalyst (containing both Lewis acid and Brønsted base sites) to form 2-propoxide on the catalyst surface (step i). This dehydrogenated intermediate generated hydrogen species and acetone via direct catalytic transfer or MPV mechanism (step ii). Then, the hydrogen species reduced metal oxides surface simultaneously to form metal active sites (Lewis acid) and this process generated water (Table S3) which could partially reoxidize the metals to metal hydroxides. After ML was inserted to the active metal sites (step iii) under adequate reaction pressure resulted from generated hydrogen gas and alcohol vapor at 200 °C, ML could then spontaneously react with adsorbed hydrogen species on the catalyst surface to form methyl gamma-hydroxypentanoate (GHP) adsorbed on the surface (step iv).<sup>29-31,34</sup> Some of this intermediate could be eliminated from the surface (step v) while the others underwent cyclization (step vii) leading to GVL production as well as methanol (MeOH) formation (step viii). The vacant active sites were then filled with 2-propanol (step ix) to generate active hydrogen species after 2-propanol dehydrogenation (step x) and acetone elimination (step xi). This led to an active site ready for the next cycle of GVL production.

Due to the fact that there were less number of Lewis acid (metal or alloy) than Brønsted base (species on the catalyst active sites at the beginning of the reaction, both alcohol dehydrogenation and GVL production preferably underwent through MPV mechanism. However, after the first cycle of reaction both MPV and metal hydride are crucial pathways for 2-PrOH dehydrogenation and ML hydrogenation.

#### 1.2.4.5 Conclusion

The catalytic transfer hydrogenation was successfully employed in both activation of copper mixed oxide catalysts and production of GVL consecutively. By using H<sub>2</sub>-TPR technique, alcohol-assisted reduction evaluation (ASR), *in-situ* XRD reduction, and XPS analysis, it was evident that the good synergistic behaviour between the secondary alcohols and the H<sub>2</sub> spillover effect in copper mixed oxide catalysts is the key for the superior catalytic performance. All catalysts showed potential performance for GVL production from ML in the 2-PrOH system at 200 °C within 3 h. The most efficient catalyst, CuNiO could be recycled up to four times with only slight decrease of GVL yield. The reaction mechanism in alcohol dehydrogenation and ML hydrogenation underwent through both MPV and metal hydride routes. The discovery in this work could pave the way for a new sustainable concept in catalysis over simultaneously activated mixed metal oxide catalysts.

### 3.3 Outputs

#### 3.3.1 Publication

- C. Rungnim, K. Faungnawakij, N. Sano, N. Kungwan, S. Namuangruk, Hydrogen Storage Performance of Platinum Supported Carbon Nanohorns: A DFT Study of Reaction Mechanisms, Thermodynamics, and Kinetics. *International Journal of Hydrogen Energy* **2018**, 43 (52), 23336–23345.
- W. Tanwongwan, A. Eiad-ua, W. Kraithong, N. Viriya-empikul, K. Suttisintong, A. Klamchuen, P. Kasamechonchung, P. Khemthong, K. Faungnawakij, S. Kuboon, "Simultaneous activation of copper mixed metal oxide catalysts in alcohols for gamma-valerolactone production from methyl levulinate", *Applied Catalysis A: General* **2019**, 579, 91-98
- C. Fang, S. Kuboon, P. Khemthong, T. Butburee, P. Chakthranont, V. Itthibenchapong, P. Kasamechonchung, T. Witoon, K. Faungnawakij, "Highly dispersed NiCu nanoparticles on SBA-15 for selective hydrogenation of methyl levulinate to gamma-valerolactone", *International Journal of Hydrogen Energy*, in press **2019**

#### 3.3.2 Conference and Forum

- Pongkarn Chakthranont, Doped-Carbon Nanohorns Catalysts for Efficient Electrosynthesis of H<sub>2</sub>O<sub>2</sub> from O<sub>2</sub> Reduction, 8<sup>th</sup> Asia Pacific Congress in Catalysis (APCAT8), 4-7 August 2019, Bangkok, Thailand
- Sanchai Kuboon, Simultaneous Activation of Copper Mixed Metal Oxide Catalysts in Alcohols for Gamma-Valerolactone Production from Methyl Levulinate, 8<sup>th</sup> Asia Pacific Congress in Catalysis (APCAT8), 4-7 August 2019, Bangkok, Thailand
- K. Faungnawakij, "Catalytic Production of Advanced Biofuels via Hydrotreatment Process: Bio-Jet, Green Diesel, and Fuel Additives" The International Conference on Advanced and Applied Petroleum,

Petrochemicals, and Polymers 2018 (ICAPPP 2018), Dec 18-20, 2018, Bangkok, Thailand (Invited Speaker)

- K. Faungnawakij, "Nanocatalysis for Biorefinery" The 23rd International Annual Symposium on Computational Science and Engineering (ANSCSE23), June 27-29, 2019, Chiang Mai University, Chiang Mai, Thailand (Invited Speaker)

- K. Faungnawakij, "Recent development of catalytic nanomaterials for biorefinery applications" The Second Materials Research Society of Thailand International Conference (2nd MRS Thailand International Conference), July 10-12, 2019, The Zign Hotel, Pattaya, Thailand (Keynote Speaker)

### **3.3.3 Book**

- S. Kuboon, W. Kraithong, J. Damaurai, K. Faungnawakij, "Ch.5 Hydro-Fractionation for Biomass Upgrading" in "Renewable Resources and Biorefineries" Editors Eduardo Jacob-Lopes, Leila Queiroz Zepka, IntechOpen **2018**, 101-114

### **3.3.4 Award**

### **3.3.5 Student exchange**

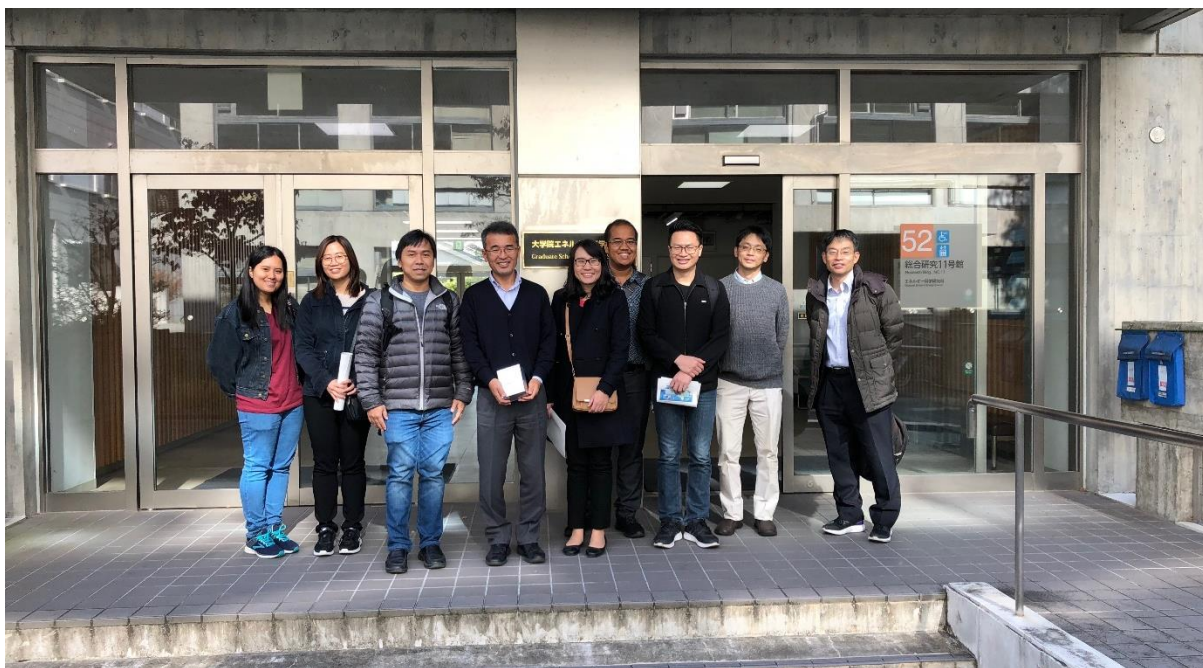
- One student exchange from Chulalongkorn University visited Kyoto Univ. for research exchange program under JASTIP, Oct 2017.

- Ms. Siripit Songtawee, Ph.D. candidate, Chulalongkorn University

- One research assistant from NANOTEC visited Kyoto Univ. for research exchange program under JASTIP, Nov 2017.

- Ms. Sutarat Thongratkaew, NANOTEC, NSTDA

- Two JASTIP seminars of the project were held in 2018 at NANOTEC (Sep, 26: Five Japanese members visited NANOTEC and Chulalongkorn Univ and at Kyoto univ (Nov, 18: 6 Thai members visited Kyoto Univ.).



(TOP) JASTIP seminar in Thailand 2018 and (Right) JASTIP seminar in Japan 2018